LEABHARLANN CHOLÁISTE NA TRÍONÓIDE, BAILE ÁTHA CLIATH | TRINITY COLLEGE LIBRARY DUBLIN
Ollscoil Átha Cliath | The University of Dublin

Terms and Conditions of Use of Digitised Theses from Trinity College Library Dublin

Copyright statement

All material supplied by Trinity College Library is protected by copyright (under the Copyright and Related Rights Act, 2000 as amended) and other relevant Intellectual Property Rights. By accessing and using a Digitised Thesis from Trinity College Library you acknowledge that all Intellectual Property Rights in any Works supplied are the sole and exclusive property of the copyright and/or other IPR holder. Specific copyright holders may not be explicitly identified. Use of materials from other sources within a thesis should not be construed as a claim over them.

A non-exclusive, non-transferable licence is hereby granted to those using or reproducing, in whole or in part, the material for valid purposes, providing the copyright owners are acknowledged using the normal conventions. Where specific permission to use material is required, this is identified and such permission must be sought from the copyright holder or agency cited.

Liability statement

By using a Digitised Thesis, I accept that Trinity College Dublin bears no legal responsibility for the accuracy, legality or comprehensiveness of materials contained within the thesis, and that Trinity College Dublin accepts no liability for indirect, consequential, or incidental, damages or losses arising from use of the thesis for whatever reason. Information located in a thesis may be subject to specific use constraints, details of which may not be explicitly described. It is the responsibility of potential and actual users to be aware of such constraints and to abide by them. By making use of material from a digitised thesis, you accept these copyright and disclaimer provisions. Where it is brought to the attention of Trinity College Library that there may be a breach of copyright or other restraint, it is the policy to withdraw or take down access to a thesis while the issue is being resolved.

Access Agreement

By using a Digitised Thesis from Trinity College Library you are bound by the following Terms & Conditions. Please read them carefully.

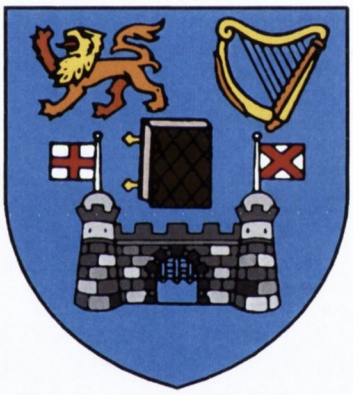
I have read and I understand the following statement: All material supplied via a Digitised Thesis from Trinity College Library is protected by copyright and other intellectual property rights, and duplication or sale of all or part of any of a thesis is not permitted, except that material may be duplicated by you for your research use or for educational purposes in electronic or print form providing the copyright owners are acknowledged using the normal conventions. You must obtain permission for any other use. Electronic or print copies may not be offered, whether for sale or otherwise to anyone. This copy has been supplied on the understanding that it is copyright material and that no quotation from the thesis may be published without proper acknowledgement.

A considered application of the Langreth-Lundqvist van der Waals density functional in the context of:

open shell molecules,

atom centered basis sets,

adsorption of graphene onto a Bi_2Se_3 slab.



Thomas Cathcart

School of Physics

Trinity College

University Dublin

A thesis submitted for the degree of

Doctor of Philosophy

March 2015

TRINITY COLLEGE
1 4 MAY 2015
LIBRARY DUBLIN

Thesis 10588

Declaration

I declare that this thesis has not been submitted as an exercise for a degree at this or any other university and it is entirely my own work.

I agree to deposit this thesis in the University's open access institutional repository or allow the library to do so on my behalf, subject to Irish Copyright Legislation and Trinity College Library conditions of use and acknowledgement.

Thomas Cathcart 

Acknowledgements

I would like to thank my friends for their years of support and teasing, without whom my life certainly wouldn't be as stimulating. It's reassuring to see that although we've grown older we haven't grown up. Thanks to my parents and family for their guidance and immeasurable support all my life. Thanks too for reading this work in spite of not understanding a word of it! Finally many thanks to Marta, you know how important you have been to me throughout this process and beyond - thank you.

"Serenity now" - Frank Costanza

Summary

The work in this thesis is aimed towards exploring the edge case application of the Langreth-Lundqvist vdW density functional (vdW-DF). The increasing popularity of the vdW-DF functional has resulted in its application across a wide variety of systems. Some of these systems are at the limit of the approximations made in the derivation of the functional, so called edge case systems. Although the vdW-DF functional may break down when applied to these edge case systems, through careful exploration of these systems we gain a greater understanding of not only the functional but also ways within which it can be improved.

We present our spin generalisation of the Langreth-Lundqvist vdW-DF density functional. Based on the adiabatic connection fluctuation dissipation theory it is an *ab initio* based method for the calculation of dispersion interactions in open shell systems. Our results for the $(N_2)_2$ and $(O_2)_2$ complexes as well as the phenalenyl dimer shows that our method provides more accurate binding energy results than the previously proposed spin-sum method [1, 2].

We examine how modifying the Siesta [3] atom centered basis set affects the accuracy of the vdW-DF binding energies. We benchmark several basis sets using the S22 molecular database and compare the error in these results to values seen in the literature. Comparisons are made with both converged plane wave DFT calculations as well as with other atom centered basis set codes. Additionally, through careful examination of the densities produced from these basis sets and comparison with plane

wave converged densities we explore the origins of the errors in the binding energies; accounting for what originates from insufficiently large basis sets and what is the result of basis set superposition errors. Finally we present general suggestions for the creation of atom centered basis sets suitable for the calculation of vdW-DF binding energies.

We compare the vdW-DF density based vdW functional against various other beyond pairwise approximation vdW methods. We find that the inclusion of many body interactions in the vdW+MB [4] gives results closest to those from diffusion Monte Carlo calculations for bilayer graphene. Calculations not including such effects fail to screen the non-local correlations and overbind with respect to the Monte Carlo results. This is also seen in our calculations for the adsorption of graphene atop a bismuth selenide slab, with beyond pairwise interactions acting to reduce the magnitude of the van der Waals binding. As these effects do not result in significant changes in the overlayer binding distances the resulting electronic bandstructures are qualitatively similar.

Contents

Summary i

1 Introduction 1

1.1 Historical background 1

1.2 The purpose of this work. 3

1.3 Outline of this thesis 3

2 Formal introduction to density functional theory 5

2.1 The many-body equation 5

2.2 Hartree-Fock and the variational principle 7

2.3 Thomas-Fermi density functional theory 9

2.4 The Hohenberg-Kohn theorems 10

2.5 Levy-Lieb constrained search and the total energy functional 12

2.6 The Kohn-Sham approximation 14

2.7 The exchange and correlation energy 16

3 van der Waals forces in density functional theory 19

3.1 Ground- Basic DFT 20

3.2 Level 1- Simple C_6 corrections 20

3.3 Level 2- Environmental C_6 coefficients 23

3.4 Level 3- Long range density functionals 25

3.5 Level 4- Beyond pairwise addition 28
3.6 Level 4- Many-body dispersion 28
3.7 Level 5- The exact XC functional 31

4 Generalisation of the vdW-DF to account for the interaction between spin polarised densities. 33

4.1 Introduction 33
4.2 Theory 35
4.2.1 Adiabatic connection fluctuation dissipation 35
4.3 Computational Methods 45
4.4 Results 49
4.4.1 $(N_2)_2$ 50
4.4.2 $(O_2)_2$ 53
4.4.3 Phenalenyl dimer 57
4.5 Conclusions 60

5 An examination of the accuracy of vdW-DF binding energies, as calculated within an atom centered basis set, over the S22 molecular database. 65

5.1 Introduction 65
5.1.1 Plane wave and atom centered basis sets. 66
5.1.2 Construction of the Siesta basis set. 69
5.2 Quantifying the accuracy of vdW interactions 71
5.3 Computational Methods 74
5.4 Results 75
5.4.1 Density based analysis of vdW-DF errors. 75
5.4.2 Analysis of vdW-DF S22 errors. 105

5.4.3 Comparison to literature results. 111

5.5 Conclusions 113

6 A comparison of the overlayer adsorption of graphene onto a Bi_2Se_3 slab using the vdW-DF and recent beyond pairwise approximation methods. 115

6.1 Introduction 115

6.2 Computational Methods 119

6.3 Results 121

6.3.1 Interlayer binding in bilayer graphene. 121

6.3.2 Relaxation of three quintuple layer Bi_2Se_3 slab. 126

6.3.3 Adsorption of a graphene overlayer atop an unrelaxed Bi_2Se_3 slab. 130

6.3.4 Adsorption of a graphene overlayer atop a relaxed Bi_2Se_3 slab. 134

6.3.5 Electronic bandstructure of Bi_2Se_3-graphene composite. 138

6.4 Conclusions 142

7 Final conclusions and future work. 145

7.1 Final conclusions and future work. 145

Appendix A Phenalenyl molecule optimised atomic coordinates 157

Appendix B Inverting the spin Dyson like screening equation 159

Appendix C Spin vdW kernel 163

Appendix D Evaluating the spin vdw kernel 165

Appendix E Our calculated S22 binding energies as well as the optimised Siesta basis sets and pseudopotentials used. 167

E.1 Our calculated S22 binding energies. 167

E.2 Optimised Siesta basis sets. 169

E.3 Siesta Pseudopotentials. 170

Appendix F Bi_2Se_3 $R\bar{3}m$ structure in a hexagonal lattice. 173

List of Figures

4.1 Convergence of inter-monomer binding energies 47

4.2 Dimer geometries 48

4.3 $(N_2)_2$ binding curves 52

4.4 $(O_2)_2$ binding curves 'H' geometry 55

4.5 $(O_2)_2$ binding curves 'X' geometry 56

4.6 Phenalenyl dimer binding energy curves 59

4.7 Energy difference in the non-local term between the spin-sum and spin vdW-DF interactions 63

4.8 Energy difference in the non-local term between the spin-sum and spin vdW-DF interactions for increasing interaction distances 64

5.1 Pictorial explanation of counterpoise correction. 78

5.2 Convergence of the binding energy with energy shift 79

5.3 Water dimer binding energy 85

5.4 Water dimer QE normalised density difference 86

5.5 Normalised density difference for the water dimer 87

5.6 Estimate of the BSSE for the water dimer 88

5.7 Formic acid dimer binding energy 91

5.8 Normalised density difference for the formic acid dimer 92

5.9 Estimate of the BSSE for the formic acid dimer 93

5.10 Methane dimer binding energy 96
5.11 Normalised density difference for the methane dimer 97
5.12 Estimate of the BSSE for the methane dimer 98
5.13 Benzene methane complex binding energy 101
5.14 Normalised density difference for the benzene methane complex . . . 102
5.15 Estimate of the BSSE for the benzene methane complex 103
5.16 S22 Binding energies 109
5.17 Differences between our calculated S22 binding energies and plane wave values 110

6.1 Bi_2Se_3-graphene structures 123
6.2 AA stacked bilayer binding curves 124
6.3 AB stacked bilayer binding curves 125
6.4 Bi_2Se_3 slab band structures 129
6.5 Binding energy curves for the unrelaxed Bi_2Se_3-graphene structure - top orientation 131
6.6 Binding energy curves for the unrelaxed Bi_2Se_3-graphene structure - hollow orientation 132
6.7 Binding energy curves for the relaxed Bi_2Se_3-graphene structure - top orientation 135
6.8 Binding energy curves for the relaxed Bi_2Se_3-graphene structure - hollow orientation 136
6.9 Bi_2Se_3-graphene band structures - top orientation 140
6.10 Bi_2Se_3-graphene band structures - hollow orientation 141

List of Tables

4.1 Results of $(N_2)_2$ binding curves 51

4.2 Results of $(O_2)_2$ binding curves 54

4.3 Results of phenalenyl dimer binding curves 58

5.1 Normalised density difference and associated binding energy error for the water dimer 82

5.2 Estimated and actual Siesta binding energy errors for the water dimer 83

5.3 Normalised density difference and associated binding energy error for the formic acid dimer 90

5.4 Estimated and actual Siesta binding energy errors for the formic acid dimer 90

5.5 Normalised density difference and associated binding energy error for the methane dimer 95

5.6 Estimated and actual Siesta binding energy errors for the methane dimer 95

5.7 Normalised density difference and associated binding energy error of the benzene methane complex 99

5.8 Estimated and actual Siesta binding energy errors for the benzene methane 100

5.9 Statistical errors of the S22 binding energies for various Siesta basis sets 108

5.10 Comparison of mean absolute errors in the S22 binding energies for our Siesta basis sets to literature results 111

6.1 AA stacked bilayer binding curve results 121

6.2 AB stacked bilayer binding curve results 122

6.3 Convergence of the overlayer binding energy with respect to the number of QLs in a Bi_2Se_3-graphene slab. 126

6.4 Inter-QL distances in a relaxed 3 QL slab 127

6.5 Bi_2Se_3 slab band gap at Γ point 128

6.6 Results of binding energy curves for the unrelaxed Bi_2Se_3-graphene structure - top orientation 133

6.7 Results of binding energy curves for the unrelaxed Bi_2Se_3-graphene structure - hollow orientation 133

6.8 Results of binding energy curves for the relaxed Bi_2Se_3-graphene structure - top orientation 137

6.9 Results of binding energy curves for the relaxed Bi_2Se_3-graphene structure - hollow orientation 137

6.10 Bi_2Se_3-graphene band gaps and Dirac gaps at Γ point - top orientation 139

6.11 Bi_2Se_3-graphene band gaps and Dirac gaps at Γ point - hollow orientation 139

E.1 Our calculated S22 binding energies 168

Chapter 1

Introduction

1.1 Historical background

In 1662 the Irish physicist Robert Boyle published his book detailing the first experiments with rarefied air. The law which is now his namesake relates the pressure to the inverse of the volume of an ideal gas. Such a gas is a theoretical abstraction in which its constituent particles neither interact with each other nor possess volume.

The combination of Boyle's law with Charles's law, relating temperature and volume, was introduced several times through out the mid-nineteenth century. This combination is referred to as the "ideal gas law", as it only holds true for gases that adhere closely to the unphysical ideal. This ideal considers molecules to be point-like particles, with no molecular volume. The only intermolecular interaction is as a result of elastic collisions between the particles. The equation of state for such a system follows

$$PV = NkT \tag{1.1.1}$$

where P is the pressure exerted by the gas with temperature T in a volume V, k is

Boltzmanns constant and N is the number of gas particles.

As part of his PhD thesis Johannes Diderik van der Waals introduced a corrected equation of state,

$$(P + a/V^2)(V - b) = NkT. \tag{1.1.2}$$

His two corrections account for the finite volume of the gas particles, b, and that such particles might interact, a/V^2. Allowing the gas particles to have finite volume means we cannot compress the gas infinitely. Allowing for an attractive inter particle force leads to a reduction in the total pressure the gas can exert. Although these might appear to be minor corrections, investigations into intermolecular forces consumed researchers for much of the twentieth century.

The term correcting the pressure due the intermolecular interaction is the truly extraordinary feature of van der Waals work. It was from this small correction that Johannes Diderik van der Waals introduced people to the notion of ubiquitous particle attraction. A universal atomic force acting between atoms and molecules of all types.

The work of Fritz London in the late 1930s captured the importance of van der Waals proposal. London suggested that quantum fluctuations were the cause behind the attraction of electrostatically neutral particles. Not only can this theory be applied to explain binding in rare gas dimers but such a force is universal, acting unimpeded between atoms of all types. These forces are referred to as dispersion forces as the London theory is similar to the quantum mechanical theory of light dispersion. Such forces are often included with those from other researchers investigating similar effects. Collectively they are referred to as van der Waals forces.

In 1998 Water Kohn was awarded* the Nobel Prize for his work in developing density functional theory. Perhaps the most popular and widely used electronic structure

*Along with John Pople for his work in developing ab initio quantum chemistry methods.

method in use today. It allows us to perform efficient calculations involving hundreds of electrons. In 2004 a group of researchers working with David Langreth proposed a novel new method to include these ubiquitous forces London described in density functional theory.

1.2 The purpose of this work.

The work in this thesis is aimed towards exploring the edge case application of the Langreth-Lundqvist vdW density functional. The increasing popularity of the vdW-DF functional has resulted in its application across a wide variety of systems. Some of these systems are at the limit of the approximations made in the derivation of the functional, so called edge case systems. Although the vdW-DF functional may break down when applied to these edge case systems, through careful exploration of these systems we gain a greater understanding of not only the functional but also ways within which it can be improved.

1.3 Outline of this thesis

In this thesis, we investigate the inclusion of van der Waals (vdW) forces in density functional theory (DFT). A detailed description chapter by chapter of the work presented is given below:

Chapter 2: In this chapter we introduce the framework of density functional theory. The aim of this chapter is to give the reader an understanding of the abilities as well as the limitations of the theory.

Chapter 3: In this chapter we discuss the Jacob's Ladder of vdW methods in DFT. We discuss the various levels of accuracy as well as their associated costs.

Chapter 4: In this chapter we discuss our work in generalising the vdW-DF

function to allow for the interaction of spin polarised densities. We achieve this by closely following and generalising the derivation of the vdW-DF functional. We show the performance of our functional on the open shell systems of the $(O_2)_2$ and the phenalenyl dimer as well as the closed shell $(N_2)_2$ complex. As a comparison we also calculate the binding of these systems using an alternative method based on applying the vdW-DF functional to the sum of the up and down spins instead of considering the interactions individually.

Chapter 5: In this chapter we discuss our work in investigating how the use of an atom centered basis set with the vdW-DF functional affects the accuracy of calculated binding energies. In detail we examine the differences in the binding energies and densities between calculations using an atom centered basis and a fully converged plane wave basis. We identify sources of error in the atom centered basis binding energy calculations and quantify their magnitudes for a selection of systems. We benchmark several basis sets using the S22 molecular database and compared the error in these results to values seen in the literature. From our findings we discuss strategies for the creation of accurate basis sets suitable for the calculation of vdW-DF binding energies.

Chapter 6: In this chapter we discuss our work in comparing the vdW-DF functional to several beyond pairwise approximation methods as applied to several 2D layered systems. We investigated the use of these methods on the bilayer graphene, the bismuth selenide (Bi_2Se_3) and the composite Bi_2Se_3-graphene systems. We present binding curves for the adsorption of the graphene onto a Bi_2Se_3 slab and the electronic bandstructures which result from relaxed geometries calculated using the differing vdW methods.

Chapter 7: In this chapter we summarise the main results of the thesis and discuss the opportunities for future work.

Chapter 2

Formal introduction to density functional theory

2.1 The many-body equation

The aim in the electronic structure problem is to obtain and understand the solutions of the Schödinger equation for interacting electrons,

$$\left(-\frac{1}{2}\sum_{i=1}^{N}\nabla_i^2 + \frac{1}{2}\sum_{\substack{i,j=1 \\ j\neq i}}^{N}\frac{1}{|\mathbf{r}_i-\mathbf{r}_j|} + \sum_{i=1}^{N} v_{ext}(\mathbf{r}_i) \right) \Psi(x_1\cdots x_N) = E\Psi(x_1\cdots x_N), \quad (2.1.1)$$

for different external potentials, $v_{ext}(\mathbf{r})$, where $x_i = \{\mathbf{r}_i, \sigma_i\}$ represents the set of both position and spin and N is the total number of electrons*. For compactness we also introduce the operator form of the equation,

$$(\hat{T} + \hat{V}_{ee} + \hat{V}_{ext})\Psi(x_1\cdots x_N) = E\Psi(x_1\cdots x_N), \quad (2.1.2)$$

*In this work we shall use Hartree atomic units

where

$$\hat{T} = -\frac{1}{2}\sum_{i=1}^{N}\nabla_i^2 \tag{2.1.3}$$

is the kinetic energy operator,

$$\hat{V}_{ee} = \frac{1}{2}\sum_{\substack{i,j=1 \\ j\neq i}}^{N}\frac{1}{|\mathbf{r}_i - \mathbf{r}_j|} \tag{2.1.4}$$

is the electron-electron interaction with $\mathbf{r}$ being the electronic coordinate, and

$$\hat{V}_{ext} = \sum_{i=1}^{N} v_{ext}(\mathbf{r}_i) \tag{2.1.5}$$

is the external potential. In most situations the external potential is simply the Coulombic sum of the atomic nuclei,

$$v_{ext}(\mathbf{r}) = \sum_{J}\frac{Z_J}{|\mathbf{r} - \mathbf{R}_J|}, \tag{2.1.6}$$

where $\mathbf{R}_J$ and Z_J are the locations and charges of the nuclei. The work in this thesis will be done under the Born-Oppenheimer approximation and as such the nuclear coordinates are fixed.

There are a number of constraints on the wave function, Ψ. It must integrate to N and it must obey Fermi statistics

$$\Psi(x_1 \cdots x_a \cdots x_b \cdots x_N) = -\Psi(x_1 \cdots x_b \cdots x_a \cdots x_N). \tag{2.1.7}$$

In principle, all of electronic physics within the fixed nucleus approximation can be described accurately from Equations (2.1.1),(2.1.6)(2.1.7). However unless the system we wish to examine has only a few of electrons, direct solution of these equations is

computationally intractable. For such systems we must introduce approximations to deal with the interaction of the electrons, this "many bodied" interaction. We shall now briefly review Hartree-Fock and Thomas-Fermi theories highlighting how approximations in these theories have laid the groundwork for density functional theory.

2.2 Hartree-Fock and the variational principle

The variational principle is an extremely useful tool upon which many calculations rely. It gives us a method to search for ground-state solutions by "guessing" with trial solutions [5, 6]. Only the exact ground-state wavefunction minimises the expectation value of the Hamiltonian, giving the ground-state energy:

$$E_{gs} = \min_{\Psi} \frac{\langle \Psi | \hat{H} | \Psi \rangle}{\langle \Psi | \Psi \rangle}. \tag{2.2.1}$$

If we expand our trial solution in the complete basis of exact solutions for a given Hamiltonian we get a normalised trial wavefunction of the form,

$$|\Psi_{trial}\rangle = \sum_i c_i |\psi_i\rangle, \tag{2.2.2}$$

with c_i being the expansion coefficients and ψ_i the exact solutions of the Hamiltonian. The energy expectation of such a trial is then,

$$E_{trial} = \langle \Psi_{trial} | \hat{H} | \Psi_{trial} \rangle = \sum_i |c_i|^2 E_i. \tag{2.2.3}$$

If the eigenvalues, E_i, are arranged in increasing order, such that $E_i > E_j$ given that state i lies above state j, then the ground state, and lowest energy, is given by E_0. The trial wavefunction corresponding to the exact ground-state must have $c_i = 0$ for all $i > 0$ and $|c_0|^2 = 1$.

Hartree-Fock relies on the minimisation procedure of equation (2.2.1) using the anti-symmetrised product of single particle wavefunctions from Slater determinants,

$$\Phi(x_1 \cdots x_N) = \frac{1}{\sqrt{N!}} \begin{vmatrix} \phi_1(x_1) & \cdots & \phi_N(x_1) \\ \vdots & & \vdots \\ \phi_1(x_N) & \cdots & \phi_N(x_N) \end{vmatrix} \tag{2.2.4}$$

where the ϕ's are single electron orbitals multipled by a spin function, $\phi_i(x_j) = \psi_j(\mathbf{r}_i)\chi_j(\sigma_i)$.

Other methods rely similarly on Slater determinants and the variational principle. One such method is configuration interaction, CI, which involves a minimisation over a sum of different N-particle Slater determinants. Again however, for more than a few electrons this method become computationally too expensive [7].

Two alternatives exist, to approximate the sum of Slater determinants, or treat the electron electron interaction as a perturbation.

1. Coupled Cluster (CC) methods do the former, and are approximations of configuration interaction [8, 9]. CCSD(T) is a CC calculation where Single and Double excitation determinants are considered self-consistently while Triple excitations are included perturbatively.

2. Møller-Plesset methods treat electron-electron interactions as a perturbation on top of the Hartree-Fock energy [10]. MP2 is a second order perturbation which is commonly used, MP4 is another method which is fourth order.

We will not be using such methods in this thesis, but some of them will be used as benchmarks for calculations. They give very accurate approximations to the exact solutions of the Schrödinger equation although at a high computation cost.

2.3 Thomas-Fermi density functional theory

Named after Llewellyn Thomas and Enrico Fermi this is the first and simplest density functional theory, DFT [11, 12]. It is a semi-classical theory introduced shortly after the introduction of the Schrödinger equation. Crucially, rather than working with the complex many electron wavefunction it uses the ground state particle density,

$$n(\mathbf{r}) = N \int d\sigma_1 d^4x_2 \cdots d^4x_N |\Psi(\mathbf{r}, \sigma_1, x_2, \cdots, x_N)|^2. \tag{2.3.1}$$

From the ground state density, experimental observables can be extracted through the use of functionals. The Thomas-Fermi energy functional extracts the total energy from the density,

$$E^{TF}[n] = T_{TF}[n] + \int d^3r v_{ext}(\mathbf{r}) + U_H[n] \tag{2.3.2}$$

with

$$T_{TF}[n] = \frac{3(3\pi)^{3/2}}{10} \int d^3r n^{5/3}(\mathbf{r}) \tag{2.3.3}$$

being the Thomas-Fermi approximation to the kinetic energy of a uniform non-interacting electron gas. The v_{ext} term is the previously mentioned external energy of equation (2.1.6). The final term is the Hartree energy,

$$U_H[n] = \frac{1}{2} \int d^3r d^3r' \frac{n(\mathbf{r})n(\mathbf{r}')}{|\mathbf{r} - \mathbf{r}'|}, \tag{2.3.4}$$

the classical electrostatic energy of the electrons.

The Thomas-Fermi theory fails to describe the exchange energy [13], and the error in kinetic energy is large [14]. Consequently bonding is not energetically favourable

in this approximation [15]. The Thomas-Fermi theory therefore is of limited practical use and serves as a historical footnote in the development of density functional theory.

2.4 The Hohenberg-Kohn theorems

The Hohenberg and Kohn theorems place the Thomas-Fermi idea of using the particle density as a fundamental variable on firmer theoretical ground. They establish a one-to-one correspondence between a given external potential and the ground state density [16].

Usually, to obtain solutions for the ground-state electronic structure we employ the following method. Start with an external potential and solve equation (2.1.1). From this we obtain the ground-state wavefunction from which we can extract experimental observables such as the ground-state electron density*, or more succinctly,

$$v_{ext} \rightarrow \Psi_0 \rightarrow n_0, \tag{2.4.1}$$

where Ψ_0 and n_0 are the ground state wavefunction and density respectively. As we previously mentioned, however, the many electron wavefunction is complex and difficult to solve. By proving the bijective mapping

$$v_{ext} \leftrightarrow n_0, \tag{2.4.2}$$

seen in the Hohenberg and Kohn theorems, we gain a significant advantage allowing us to bypass the wavefunction. The proof of such a mapping is a proof by contradiction using the same idea as the variational principle. Imagine we have two external potentials which both give the same ground-state density. We also choose these such

*The electron density can be experimentally inferred from x-ray diffraction patterns.

that they differ by more than a simple constant. For now we only consider systems with non-degenerate ground-states. The two potentials are denoted with different ground-state wavefunctions,

$$\begin{aligned} v_{ext,1} &\rightarrow |\Psi_1\rangle \\ v_{ext,2} &\rightarrow |\Psi_2\rangle. \end{aligned} \tag{2.4.3}$$

Using the variational principle we see that using the ground-state wavefunction from one potential as a trial wavefunction in the other potential we get the inequality,

$$\langle \Psi_2 | \hat{H}_1 | \Psi_2 \rangle > \langle \Psi_1 | \hat{H}_1 | \Psi_1 \rangle, \tag{2.4.4}$$

where $\hat{H}_i$ is the Hamiltonian, $\hat{T} + \hat{V}_{ee} + \hat{v}_{ext,i}$, constructed with the external potential $v_{ext,i}$. The first term in equation 2.4.4 can be rewritten as

$$\begin{aligned} \langle \Psi_2 | \hat{H}_1 | \Psi_2 \rangle &= \langle \Psi_2 | \hat{H}_2 | \Psi_2 \rangle + \langle \Psi_2 | \hat{H}_1 - \hat{H}_2 | \Psi_2 \rangle \\ &= E_2 + \int d^3r [v_{ext,1}(\mathbf{r}) - v_{ext,2}(\mathbf{r})] n_0(\mathbf{r}) \end{aligned} \tag{2.4.5}$$

where E_2 is the expectation energy of the Hamiltonian with the $v_{ext,2}$ potential. This gives an alternative representation of the inequality,

$$E_2 + \int d^3r [v_{ext,1}(\mathbf{r}) - v_{ext,2}(\mathbf{r})] n_0(\mathbf{r}) > E_1. \tag{2.4.6}$$

The reverse procedure can now be done giving,

$$E_1 + \int d^3r [v_{ext,2}(\mathbf{r}) - v_{ext,1}(\mathbf{r})] n_0(\mathbf{r}) > E_2. \tag{2.4.7}$$

Adding equations (2.4.6) and (2.4.7) gives the desired contradiction, $E_1 + E_2 >$

$E_1 + E_2$. This statement requires our original assumption, that our two potentials differ by more than a constant, to be wrong. Thus we have shown how, by contradiction, the density uniquely determines the external potential to within a constant.

2.5 Levy-Lieb constrained search and the total energy functional

We include this section for two reasons: firstly, to formally introduce the idea of functionals, as well as a method of obtaining the exact functional. This is the fundamental functional that will give the exact ground-state density. Secondly, the constrained search is, in the author's opinion, a clearer and theoretically sounder derivation than the original from Hohenberg and Kohn allowing for degenerate ground states.

In the mathematical sense a *functional* is a map from a vector space to its underlying scalar field. Put succinctly, a functional can be considered a *function of a function.* That is, it is a function which takes an entire function as its argument. A simple example is the definite integral,

$$I = \int_{x_1}^{x_2} f(x)dx. \tag{2.5.1}$$

We shall denote functionals in this work as functions with square brackets around their arguments,

$$f(x) \rightarrow \text{function}$$
$$f[x] \rightarrow \text{functional.}$$

The idea behind the Levy-Lieb constrained search is to perform a two step min-

imisation [17]. We rewrite the variational principle, equation (2.2.1), so it becomes,

$$E[n] = \min_{n}(F[n] + \int d^3r v_{ext}(\mathbf{r})n(\mathbf{r})) \tag{2.5.2}$$

with the minimisation running over a set of N-particle density-distributions, n. The functional $F[n]$ is the universal functional, it is independent of the external potential, and defined as,

$$F[n] = \min_{\Psi \to n} \langle \Psi | \hat{T} + \hat{V}_{ee} | \Psi \rangle \tag{2.5.3}$$

with the minimisation running over the set of many-body wavefunctions, Ψ which give the density n. Minimising equation (2.5.2) with the constraint that the density integrates to a fixed number of electrons,

$$\delta\{F[n] + \int d^3r n(\mathbf{r}) v_{ext}(\mathbf{r}) - \mu \left[\int d^3r n(\mathbf{r}) - N \right] \} = 0 \tag{2.5.4}$$

with μ being the Lagrange multiplier, gives the variational equation

$$v_{ext}(\mathbf{r}) = \mu - \frac{\delta F[n]}{\delta n(\mathbf{r})}. \tag{2.5.5}$$

The expression, $\frac{\delta F[n]}{\delta n(\mathbf{r})}$, is the functional derivative of the universal functional, $F[n]$, with respect to the density, $n(\mathbf{r})$. It is important to emphasise here that solving equation (2.5.2), with the constraint that the density integrates to a fixed number of electrons, is equivalent to solving the Schrödinger equation. This would be true if the exact universal functional, $F[n]$, was known making DFT an exact method to obtain the ground-state density. We shall talk about the approximations which are required to carry out calculations in practice and the implications in the following sections.

2.6 The Kohn-Sham approximation

The difficulty in using the Hohenberg and Kohn DFT is in evaluating the kinetic and interaction terms given that they are for a system of N interacting particles. In the Hartree-Fock method each particle is subject to the mean field created by all the other particles. It is through this field that the particles "interact". The Kohn-Sham (KS) method [18] can be viewed in a similar fashion, both being mean field theories. We replace the system of N interacting particles with an analogous system of non-interacting particles. This alternative system is constructed to give the same ground-state density as the fully interacting one. In doing so we can calculate the many body energy terms using non-interacting particles. We can improve on the Thomas-Fermi estimate of the kinetic energy, equation (2.3.3), by using

$$T_s[n] = \min_{\phi_s \to n} \langle \phi_s | \hat{T} | \phi_s \rangle \tag{2.6.1}$$

where ϕ_s is a Slater determinant of single-particle orbitals. The minimisation runs over all the determinants that give the density n. The result is the exact kinetic energy of a system of non-interacting electrons with a density n. Using this we can rewrite the total energy functional as

$$E[n] = T_s[n] + U_H[n] + E_{xc}[n] + \int d^3r v_{ext}(\mathbf{r}) n(\mathbf{r}) \tag{2.6.2}$$

with U_H being the Hartree energy and E_{xc} the exchange and correlation energy. This is also referred to as the "ignorance energy", it is the term that makes up the remainder of the universal functional

$$E_{xc}[n] = F[n] - (T_s[n] + U_H[n]). \tag{2.6.3}$$

Performing a constrained minimisation to obtain the Kohn-Sham potential, similar to equation (2.5.5), gives us

$$v_{KS}(\mathbf{r}) = \mu - \frac{\delta T_s[n]}{\delta n(\mathbf{r})}. \tag{2.6.4}$$

Solutions to this are the same as solving

$$(-\frac{1}{2}\nabla^2 + v_{KS}([n];\mathbf{r}))\phi_{i,\sigma}(\mathbf{r}) = \epsilon_{i,\sigma}\phi_{i,\sigma}(\mathbf{r}) \tag{2.6.5}$$

for the KS orbitals with,

$$v_{KS}(\mathbf{r}) = v_{ext}(\mathbf{r}) + \frac{\delta U_H[n]}{\delta n(\mathbf{r})} + \frac{\delta E_{xc}[n]}{\delta n(\mathbf{r})}. \tag{2.6.6}$$

This expression can be obtained by combining equations (2.5.5) (2.6.4) as they both are expressions for μ, the chemical potential. The term $\epsilon_{i,\sigma}$ is the eigenenergy corresponding to the $\phi_{i,\sigma}(\mathbf{r})$ KS eigenstate. The density is simply the sum of the occupied KS orbitals,

$$n(\mathbf{r}) = \sum_{\substack{i \\ occupied}} |\phi_i(\mathbf{r})|^2. \tag{2.6.7}$$

Solving equation (2.6.5), also known as the KS equations, must be done self-consistently. Starting with a guess for the density a KS potential is constructed. The resulting KS equation is solved giving the KS orbitals from which a new density is obtained. The process is repeated until the change in the input and output densities is less than a given tolerance.

In the KS approach the largest portion of the total energy, the kinetic part, is obtained exactly through the use of the non-interacting particle system. Only the E_{xc}

term must be approximated. This shall be one of the central themes of this thesis; how current approximations to this term fail to include van der Waals forces and how recently proposed methods correct for this.

2.7 The exchange and correlation energy

The exchange and correlation energy term, E_{xc}, is the crux of the Kohn-Sham method. It is the only term that must be approximated and the accuracy of the approximation can drastically change the results of calculations.

The exchange energy can we written as

$$E_x = -\frac{1}{2}\sum_{\sigma}\sum_{\substack{i,j \\ occupied}}\int d^3r \int d^3r' \frac{\phi^*_{i\sigma}(\mathbf{r})\phi^*_{j\sigma}(\mathbf{r}')\phi_{i\sigma}(\mathbf{r}')\phi_{j\sigma}(\mathbf{r})}{|\mathbf{r}-\mathbf{r}'|} \tag{2.7.1}$$

where the ϕ_i's are the KS orbitals.

Jacob's ladder of XC approximations

First introduced by John Perdew the Jacob's ladder is a parody of the biblical ladder to heaven. It makes an important point for DFT XC approximations however. To climb the ladder and reach more accurate approximations we must exert an ever increasing amount of computational effort.

- Local Density Approximation (LDA) [18, 19, 20, 21]

$$E_{xc}^{LDA}[n] = \int d^3r n(\mathbf{r})\epsilon_{xc}(n(\mathbf{r})) \tag{2.7.2}$$

The idea behind the Kohn-Sham approximation is that the Hartree energy captures most of the long range electron-electron interaction and the remainder can be approximated by a local term. From this understanding it is easy to see why

the local density approximation has been so successful despite their simplicity*. We shall see in the next section how such approximations ultimately miss out on the crucial long range interactions required for vdW. The LDA is correct, by construction, for the uniform electron gas. It is accurate for uniform density and slowly varying density systems, making it most useful in solid-state physics. The exchange and correlation energy per electron, $\epsilon_{xc}(\mathbf{r})$, is a combination of the exchange functional, which can be solved analytically for the homogeneous electron gas [23, 14, 24, 25], and a correlation functional parameterised from highly accurate Monte Carlo calculations of the homogeneous electron gas.

- Generalised Gradient Approximation (GGA) [26, 27, 28, 29]

$$E_{xc}^{GGA}[n] = \int d^3r n(\mathbf{r})\epsilon_{xc}(n(\mathbf{r}), \nabla n(\mathbf{r})) \tag{2.7.3}$$

Early gradient approximations were based about a naïve expansion about the LDA and suffered numerous problems. More considered expansions respecting important limits however lead to the generalised gradient expansion. GGA's improve upon the LDA results in particular for molecules and other quickly varying density environments such as surfaces and reduced dimensional systems.

- Meta Generalised Gradient Approximation (meta-GGA) [30]

$$E_{xc}^{meta-GGA}[n] = \int d^3r n(\mathbf{r})\epsilon_{xc}(n(\mathbf{r}), \nabla n(\mathbf{r}), \tau_s(\mathbf{r})) \tag{2.7.4}$$

This is an extension to the GGA which also includes a dependence on the non-

*The unexpected level of accuracy in LDA calculations is as a result of "error cancellation" [22].

interacting kinetic energy,

$$\tau_s(\mathbf{r}) = \frac{1}{2}\sum_i |\nabla\phi_i|^2. \tag{2.7.5}$$

- Orbital functions or Hyper-GGA's [31] Orbital functions like the Perdew-Zunger self interaction correction rely on the occupancy of the KS orbitals. So called hyper-GGA's include a fraction of the exact exchange.

- Unoccupied Orbitals. It is important to remember that DFT is a ground state theory. This is true even if we had the exact XC functional. In order to obtain accurate values for the unoccupied orbitals we need to use some beyond DFT method. This could be the random phase approximation (RPA)* or screened Greens function (GW) method [32]. Such methods will not be examined in this thesis but will be used as a reference in particular the RPA as it is know to give reasonable vdW energies for a range of geometries.

*See section 3.7

Chapter 3

van der Waals forces in density functional theory

In recent years there has been an increased interest in the development of vdW in DFT. This is due to the emergence of efficient and accurate vdW methods which can be utilised within a DFT framework. As our calculations move towards larger and more complex systems we face the increasing need to include such ubiquitous forces, acting between atoms of all types. In the following chapters we shall see how vdW plays an important role in a range of different systems. In this chapter we introduce the vdW techniques we shall rely on in the subsequent chapters.

DFT gives easy access to calculations of systems involving hundreds of atoms. As we move from the nano-scale to the mesoscopic, particularly in diffuse systems, vdW play an increasingly important role. This is clear even from the simplistic pairwise sum approximation of vdW for large bodies. The strength of the force grows like $\mathcal{O}(N^2)$ where N is the number of atoms in the system.

In their review [33] of vdW methods in DFT Klimes and Michaelides suggest a Jacob's ladder* type arrangement of the vdW methods. In this chapter we shall

*See section 2.7 for our discussion of the exchange and correlation Jacob's ladder.

expound and expand on this ladder focusing on the methods relevant to this thesis.

At each step on the ladder we consider the level of approximation each method uses to obtain the long range dispersion interaction. In doing this we can group together methods which exploit similar approximations.

3.1 Ground- Basic DFT

At the bottom of our ladder are the basic DFT methods. This includes the local (LDA) and semi-local (GGA) functionals as they *do not* describe long range electron-electron correlation. As a result they can never describe the long range asymptotics. They give incorrect binding curve shapes and vastly underestimate the binding energy of well separated molecules.

Some of these methods however are still used for weakly bonded systems. This is because some standard DFT functionals bind dispersion bound systems at short ranges. The best example of this is the LDA functional which has been used frequently for studies of graphite [34, 35] or noble gases on metals [36]. Accurate LDA results however are limited and inconsistent. Simply put, basic DFT methods do not describe the asymptotic form of the vdW interaction correctly.

3.2 Level 1- Simple C_6 corrections

At this step the aim is to correct basic DFTs failure to describe the vdW asymptote. To do this we add a corrective term to the DFT energy

$$E_{DFT+D} = E_{KS-DFT} + E_{disp} \tag{3.2.1}$$

where E_{disp} is the dispersion energy. For this work we shall use the $DFT + D$ method of Grimme *et al.* [37], that is $DFT + Dispersion$. Simply put, it is the pair wise summation approximation to dispersion forces. The dispersion energy is given by

$$E_{disp} = -s_6 \sum_{i}^{N} \sum_{\substack{j \\ j \neq i}}^{N} \frac{C_6^{ij}}{R_{ij}^6} f_{damp}(R_{ij}). \tag{3.2.2}$$

R_{ij} is simply the interatomic distance between the atoms. This is an *empirical* or at best "semi-empirical" method due to the large amount of fitting parameters used. The parameters, as seen in equation (3.2.2), are

1. C_6^{ij}

   This is perhaps the kernel of the DFT+D method, alongside the use of the damping function. Rather than calculate the C_6 values at run time, the coefficients are pre-calculated and stored. Crucially here though the C_6^{ij} value between two different atoms, i and j, depends on the polarisabillity of both atoms, as can be seen with the Casimir-Polder equation [38]

   $$C_6^{ij} = \frac{3}{\pi} \int_0^{\infty} du \alpha_i(iu) \alpha_j(iu) \tag{3.2.3}$$

   Rather than store the C_6 values for every atom combination in the periodic table (almost 7 thousand values) instead the value of every element with itself is stored, C_6^{ii}. A simple average is then used to get the correct inter atomic coefficient,

   $$C_6^{ij} = 2 \frac{C_6^{ii} C_6^{jj}}{C_6^{ii} + C_6^{jj}}. \tag{3.2.4}$$

   There are of course issues with how the individual C_6 coefficients are calculated, what hybridization state the atoms are in and whether the resulting C_6 value

is transferable to the required system. Grimme places the error in the binding energy due to such mismatched coefficients on the order of 10-20%. [39]

2. R_0

   This is the vdW radii, an imaginary hard sphere surrounding the atom to model its finite size. This is similar to the molecular volume in the vdW equation of state, (1.1.2). These are entirely theoretical constructs however with no general method to extract such parameters from experiment, particularly for the disperse systems of interest here. These values are usually derived choosing an electron density contour from restricted open shell Hartree Fock calculations [37]. Again the issue of transferability also arises with these parameters.

3. $f_{damp}(R_{ij})$

   This is perhaps the most empirical part of the method. Although the exchange and correlation functional is typically local or semi-local, they still capture some of the vdW dispersion energy, particularly in the short range. In order to avoid double-counting this contribution and also to avoid the singularity at $R_{ij} = 0$, a cut off function is introduced to restrict the dispersion contribution to long range separations. In essence this is an artificial restriction to ensure that the dispersion energy we add is an *intermolecular* interaction and not an *intramolecular* interaction. It is defined as

$$f_{damp}(R_{ij}) = \frac{1}{1 + e^{-\kappa(R_{ij}/R_0 - 1)}} \tag{3.2.5}$$

   with R_0 being the sum of the atomic vdW radii and κ is a factor chosen to make sure the function decays at small R_{ij} fast enough so the interaction is *inter*-atomic. κ is fixed at 23 and does not change for differing systems.

4. s_6

This is the final piece of parametrisation in this method. It is a scale factor which varies for different exchange and correlation functionals. Values for this are obtained by fitting binding energies and intermolecular distance for a test set of complexes to experimental or reliable theoretical values.

Aside from the issues with the large amount of fitting parameters involved in this method it suffers, expectedly, everywhere the pairwise summation approximation fails. Despite these problems the relative simplicity of this method has been a significant factor in its success. Reasonable atomic geometries, bond lengths and binding energies are obtained for a range of systems [40, 41, 42, 43].

The biggest issue with methods at this level of approximation is the use of same C_6 coefficients in every environment.

3.3 Level 2- Environmental C_6 coefficients

At this step the idea is to use or incorporate an environmental dependence into the C_6 values. We still use the dispersion expressions from Step 1, equations (3.2.1) and (3.2.2) in combination with some reference data. Here we shall discuss the approach of Tkatchenko and Scheffler (TS-vdW) [44] although there are other similar methods also on this level such as the $DFT - D3$ method of Grimme [45].

The TS-vdW method starts with the Casimir-Polder expression [38] for the exact C_6 value,

$$C_6^{AB} = \frac{3}{\pi} \int_0^\infty du \alpha_A(iu) \alpha_B(iu) \tag{3.3.1}$$

with $\alpha_A(iu)$ being the frequency dependent polarisability of fragment A. Dropping all

but the first term in the Padé series for $\alpha_A(iu)$ gives

$$\alpha_A^1(\omega) = \frac{\alpha_A^0}{1 + (\frac{\omega}{\eta_A})^2}, \tag{3.3.2}$$

where α_A^0 is the static polarisability of A and η_A an effective frequency. Substituting $\alpha_A^1(\omega)$ for $\alpha_A(iu)$ in equation (3.3.1) gives the London formula,

$$C_6^{AB} = \frac{3}{2}\left[\frac{\eta_A \eta_B}{\eta_A + \eta_B}\right]\alpha_A^0 \alpha_B^0. \tag{3.3.3}$$

In the homo-nuclear case, with A = B as in H_2 O_2 etc., we get

$$\eta_A = \frac{4}{3}\frac{C_6^{AA}}{(\alpha_A^0)^2}. \tag{3.3.4}$$

We can then combine equations (3.3.3) and (3.3.4) to obtain an expression which only depends on homo-nuclear parameters*,

$$C_6^{AB} = \frac{2C_6^{AA}C_6^{BB}}{\frac{\alpha_B^0}{\alpha_A^0}C_6^{AA} + \frac{\alpha_A^0}{\alpha_B^0}C_6^{BB}}. \tag{3.3.5}$$

To allow for environmental effects we define an effective C_6 coefficient to be used for atoms inside molecules or solids. Noting the direct relationship between polarisability and volume† we can construct a relationship between the free atom polarisabilities and effective polarisabilities inside molecules and solids,

$$\frac{\kappa_A^{eff}}{\kappa_A^{free}}\frac{\alpha_A^{eff}}{\alpha_A^{free}} = \frac{V_A^{eff}}{V_A^{free}} \tag{3.3.6}$$

*obtained from the reference data of Chu and Dalgarno [46]

†This can be easily observed by examining the SI units of polarisability. The SI units are $[Coulombs][meters^2][Volts^{-1}]$. When this is multiplied by $\frac{1}{4\pi\epsilon_0}$, where ϵ_0 is the vacuum permittivity, we get the desired units of cubic meters.

where κ_A^i is the proportionality constant between the volume and polarisability for the free-atom and atom in situ environments. The volumes V_A^i are calculated using the Hirshfeld partitioning of the DFT density. Then using equations (3.3.3) and (3.3.4) we get the effective C_6 coefficient,

$$C_6^{AA,eff} = \frac{\eta_A^{eff}}{\eta_A^{free}} \left(\frac{\kappa_A^{free}}{\kappa_A^{eff}} \right)^2 \left(\frac{V_A^{eff}}{V_A^{free}}^2 \right) C_6^{AA,free}. \tag{3.3.7}$$

Tkatchenko and Scheffler make the assumption here that

$$\frac{\eta_A^{eff}}{\eta_A^{free}} \left(\frac{\kappa_A^{free}}{\kappa_A^{eff}} \right)^2 \simeq 1, \tag{3.3.8}$$

meaning that the effective C_6 parameters are simply the free atom values scaled by the relative change in the partitioned density volume. Similarly the reference values of R_0^{free}, the free atom vdW radii, are scaled to give effective environmental dependent values.

C_6 coefficients calculated with this method were compared to a database of 1225 parameters ranging across atoms, organic and inorganic molecules [44] resulting in a mean absolute relative error of 5.5%. It is not clear yet how transferable such a scheme is however and whether such a simple scaling of the C_6 values with volume will also give accurate results for more difficult systems, such as those involving different oxidation states.

3.4 Level 3- Long range density functionals

The methods in the previous steps required predetermined reference parameters to calculate the dispersion energy, either the C_6 coefficients or the atomic polarisabilities. Methods on this step do not rely on external input parameters to calculate

the dispersion interaction, only the electron density. Such methods are referred to as "non-local" in the literature as they add long range correlations to local or semi-local correlation functionals.

The non-local correlation energy E_c^{nl} is calculated from

$$E_c^{nl} = \int\int dr_1 dr_2 n(\mathbf{r}_1)\phi(\mathbf{r}_1, \mathbf{r}_2)n(\mathbf{r}_2) \tag{3.4.1}$$

which is a double integral with $n(\mathbf{r})$ being the electron density and $\phi(\mathbf{r}_1, \mathbf{r}_2)$ some kernel function. The form of this equation however is not unfamiliar, if the kernel function were the simple Coulomb interaction, $\phi(\mathbf{r}_1, \mathbf{r}_2) = |\mathbf{r}_1 - \mathbf{r}_2|^{-1}$, the expression would the Hartree energy*. To obtain the dispersion energy, the required expression must be more complicated becoming $\mathcal{O}(|\mathbf{r}_1 - \mathbf{r}_2|^{-6})$ asymptotically. It is important to note that because of the form of the kernel this method follows the pairwise summation approximation, ignoring points between $\mathbf{r}_1$ and $\mathbf{r}_2$.

Various forms for E_c^{nl} were suggested throughout the 1990s, subject to the harsh restriction of non-overlapping fragments [47]. This restriction was removed by Langreth *et al.* in the early 2000s [48, 49] who proposed a functional form which could be evaluated for overlapping fragments with arbitrary geometries. The key to evaluating the exchange and correlation energy in this scheme is to divide the correlation into two regimes under which two different approximations can be made. The expression for this is

$$E_{xc} = E_x + E_c^{local} + E_c^{nl}, \tag{3.4.2}$$

where the exchange energy, E_x, is evaluated using a GGA functional and the correlation energy, E_c is split into local, E_c^{local}, and non-local, E_c^{nl} or nl, terms. This method

*such an expression however fails to take account for double counting

is referred to as the van der Waals density functional (vdW-DF).

Such methods will receive much of our attention in this work. We generalise the vdW-DF to open shell systems in chapter 4, evaluate the performance of the functional with atom centered basis sets in chapter 5 and apply the functional in comparison to beyond pairwise methods for the adsorption of graphene onto Bi_2Se_3 slabs in chapter 6. For now though we wish to highlight some of the well documented results from the literature.

The most discussed results are comparisons of the binding energies and bond lengths with respect to experiment or higher accuracy wavefunction methods. It has been generally accepted that the vdW-DF method increases dispersion bond lengths [48, 49, 50, 51]. While the initial method was implemented in a post-processing fashion Thonhauser *et al.* introduced the vdW-DF exchange and correlation potential [52], allowing for self-consistent calculations. Although they show that calculating vdW complexes self consistently does not alter the interaction energies near equilibrium binding distances, it does allow for the calculation of Hellmann-Feymann forces. This results in more efficient geometry relaxations.

In the long range limit the vdW density functional tends to overestimate the dispersion interaction. Vydrov and van Voorhis showed how a significantly simplified, analytical form, of the kernel could reduce the MAPE* errors in the calculated C_6 coefficients from 23% with the vdW-DF, to less than 13% [53, 54, 55]. To correct for these large errors the authors of the vdW functional [49] introduced an alternative method [56] which swapped the revPBE [28] exchange for the pw86 [29] exchange part. The idea behind this was to reduce the spurious overbinding originating from the exchange interaction. Such modifications to the exchange term have been widely examined [57, 58, 59] with optB88 and optPBE exchange functionals showing good

*Mean Absolute Percentage Error

performance across a wide range of systems [59, 60, 61].

The vdW-DF bulk moduli results appear to follow those of other functionals, where an increase in the bond length corresponds to a decrease in the bulk moduli. Klimeš *et al.* tested the vdW-DF functional across a wide range of systems including metals, ionic, and covalent materials. They found that both variants of the functional *underestimated* the bulk moduli by up to 45% [61], largest for the alkali metals, with similar results found by others [62, 63, 64].

This density functional method has become an important milestone for vdW methods in DFT. It gives an accurate description of the dispersion within the framework of a DFT functional and combines the correlations of all ranges in a single formula.

3.5 Level 4- Beyond pairwise addition

All the methods up to this step considered the dispersion interaction to be pairwise additive. That is, the interaction of two segments is independent of the inter-segment environment. The consequence of this assumption is that the interaction of two atoms or molecules is independent of the material that separates them and no consideration is made for collective excitations. Although such considerations are not important for gas phase, or small molecules interactions, they become increasingly important for systems where the bare intermolecular interaction is screened by the presence of the other constituents.

3.6 Level 4- Many-body dispersion

The recent paper of Tkatchenko *et al.* [4] added two important features to their earlier work [44]. They added an electrostatic screening correction to the dipole-dipole interaction and non-additive many bodied effects.

Methods discussed on lower steps do not include long-range screening beyond those included in the atomic densities. The two bodied vdW interaction results from the interaction of fluctuating dipoles. When the atoms are embedded in a system, solid or large molecule, they will experience dipole fluctuations which differ from those of the free atoms. Beyond simple local environmental effects there is also the long range electrostatic screening by distant dipoles. It is this dynamic electric field created by surrounding atoms, leading to polarisation and depolarisation effects, which is the major contributor to the anisotropy in molecular polarisability.

By modelling the environment as a dipole field we can construct a classical electrodynamics equation, which we solve self-consistently, for the self-consistent screening (SCS),

$$\alpha^{SCS}(\mathbf{r}; iu) = \alpha^{TS}(\mathbf{r}; iu) + \alpha^{TS}(\mathbf{r}; iu) \int dr' \mathcal{T}(\mathbf{r} - \mathbf{r}') \alpha^{SCS}(\mathbf{r}; iu). \tag{3.6.1}$$

Where we represent the Tkatchenko and Scheffler approximate frequency dependent polarisability, equation (3.3.2), by $\alpha^{TS}(\mathbf{r}; iu)$ and $\mathcal{T}(\mathbf{r} - \mathbf{r}')$ is the dipole-dipole interaction tensor. The SCS equation, equation (3.6.1), however requires $\alpha^{TS}(\mathbf{r}; iu)$ to be a continuous function over space while equation (3.3.2) gives only point polarisabilities.

To extend the previous scheme we note that equation (3.3.2) is the frequency-dependent dipole polarisability of the spherical quantum harmonic oscillator (QHO) with Gaussian density. By modelling the N atoms in our system as a collection of QHOs an integration over $\mathbf{r}$ space gives a discretised version of the SCS equation,

$$\alpha_p^{SCS}(iu) = \alpha_p^{TS}(iu) + \alpha^{TS}(iu) \sum_{q \neq p}^{N} \mathcal{T}_{pq}(\mathbf{r} - \mathbf{r}') \alpha_q^{SCS}(iu). \tag{3.6.2}$$

where $\mathcal{T}_{pq} = \nabla_{\mathbf{r}_p} \otimes \nabla_{\mathbf{r}_q} W(r_{pq})$ is the dipole-dipole interaction tensor, $\mathbf{r}_p$ is the position of the QHO centered on atom p and $W(r_{pq})$ is the Coulomb interaction for two

spherical Gaussian distributions with $r_{pq} = |\mathbf{r}_p - \mathbf{r}_q|$.

Perhaps more interestingly Tkatchenko *et al.* also described a method to approximate the many bodied interaction of dipoles in an non additive fashion. To calculate the many bodied vdW energy they use the coupled fluctuating dipole model (CFDM) applied to a collection of coupled isotropic three dimensional QHOs representing the atoms of the system. The CFDM Hamiltonian is written as,

$$\hat{H} = -\frac{1}{2}\sum_{p=1}^{N} \nabla^2_{\boldsymbol{\chi}_p} + \frac{1}{2}\sum_{p=1}^{N} \omega_p^2 \boldsymbol{\chi}_p^2 + \sum_{p>q}^{N} \omega_p \omega_q \sqrt{\alpha_p \alpha_q}\, \boldsymbol{\chi}_p \mathcal{T}'_{pq} \boldsymbol{\chi}_q \tag{3.6.3}$$

where $\boldsymbol{\chi}_p = \sqrt{m_p}\boldsymbol{\mu}_p$, with $\boldsymbol{\mu}_p$ being the displacement of oscillator p from equilibrium, $m_p = (\alpha_p \omega_p^2)^{-1}$ and α_p and ω_p are the static polarisability and characteristic frequency of oscillator p, the two input values of equation (3.3.2). In equation (3.6.3) the first and second terms are the kinetic and potential terms of an isolated QHO. The final term is the many bodied dipole-dipole interaction term between QHOs with

$$\mathcal{T}'_{pq} = \nabla_{\mathbf{r}_p} \otimes \nabla_{\mathbf{r}_q} W(r_{pq})', \tag{3.6.4}$$

with $W(r_{pq})'$ being a specific form of the Coulomb potential that we will describe below. The vdW energies for our system are given by the difference between the zero point energy of the coupled and uncoupled QHOs,

$$E_{vdW} = \frac{1}{2}\sum_{p=1}^{3N} \sqrt{\lambda_p} - \frac{3}{2}\sum_{p=1}^{N} \omega_p \tag{3.6.5}$$

where λ_ps are the eigenvalues of the CFDM Hamiltonian $\hat{H}$.

In order to combine this attractive vdW energy with the other correlation contributions found in DFT XC approximations, some form of coupling must be made. The empirical coupling of Grimme, equation (3.2.5), and the intrinsic cutoff of the

non-local energy in the Dion scheme, equation (3.4.2), are two coupling suggestions we have discussed so far. In the vdW+MBD method, rather than applying an explicit empirically controlled coupling or intrinsic coupling placing strident requirements on the choice of DFT kernels with which it can be combined, we adjust the form of the Coulomb potential in dipole-dipole interaction term of the CFDM Hamiltonian. The form of the Coulomb potential is

$$W'(r_{pq}) = \frac{1 - \exp(1 - (r_{pq}/R_{pq}^{vdW})^{\beta})}{r_{pq}} \tag{3.6.6}$$

with R_{pq}^{vdW} being the vdW radius and β is the coupling parameter to determine how quickly we reach the asymptotic form, $1/r_{pq}$. β is fitted to a database of molecules to obtain XC dependent values. Choosing values of $\beta \geq 2$ means that $W'(r_{pq}) \to 0$ as $r_{pq} \to 0$, if this is fitted correctly it should provide a good coupling to the choosen XC DFT functional.

3.7 Level 5- The exact XC functional

Clearly we do not have access to the exact XC DFT functional, yet. However recently it has become standard to accept the random phase approximation [65] (RPA) as being an accurate representation of the vdW energy [66, 67, 68, 69]. The RPA exchange and correlation energy is given by the expression,

$$E_{xc}^{RPA} = -\frac{\hbar}{2\pi}\int_0^{\infty} du Tr[V \sum \chi(r, r'; iu)] + E_{self}, \tag{3.7.1}$$

where $\chi(r, r'; iu)$ is the Kohn-Sham density-density response function, V is the Coulomb interaction and E_{self} is the "self-correlation" energy of a particle with itself.

The method provides a very accurate approximation to the exact correlation en-

ergy, giving HOMO-LUMO* gaps close to those of GW [32] and accurate asymptotes across a range of different vdW geometries [70]. Though extremely accurate, evaluation of the RPA energy is expensive. Typically non-converged calculations are extrapolated to extract the correct converged energy [69]. Recently a number of suggestions have been put forward to allow for RPA calculations at a reduced computational cost. Methods such as range separation techniques [66] to response functions [71] and recasting the RPA in terms of the KS-orbitals [72] all provide opportunities to access this method at a reduced computational cost. Such methods allow us to bring this accurate calculation method to systems previously out of reach.

Although we shall not be directly using the RPA method, the vdW-DF functional is based on the adiabatic connection fluctuation dissipation [73] used to derive the RPA. We will expound on this point later as we derive the vdW-DF for a system with spin. Furthermore the RPA will be referred to as a metric measuring the accuracy of our calculations.

*This is the energy difference between the Highest Occupied Molecular Orbital and the Lowest Unoccupied Molecular Orbital.

Chapter 4

Generalisation of the vdW-DF to account for the interaction between spin polarised densities.

4.1 Introduction

The notion of a spin dependent vdW functional is perhaps unusual. It is very much the meeting point between two seemingly disparate regimes of electron-electron interactions, that of unpaired electron spins leading to localised magnetic moments and the weak electron-electron correlations leading to the vdW interaction [23]. However the weak interaction of open-shell systems lies directly at this intersection. This includes the dimerisation of molecular oxygen [74] and the interaction of phenalenyl radicals [1]. These interactions are also found in many important biological molecules, such as the interaction of oxygen with the heme molecular unit [75].

To accurately capture these interactions we have generalised the vdW density functional of Dion *et al.* [49] to spin polarised systems. In parallel to our work, two

other groups have independently tested an approximate spin generalisation of the vdW-DF [1, 2]. The approximation is based upon the simple transformation of the two spin polarised densities to a single spin-less density via

$$\rho = \rho_\uparrow + \rho_\downarrow, \tag{4.1.1}$$

where ρ is the spin-less density and $\rho_\uparrow$ and $\rho_\downarrow$ are the spin polarised up and down densities. This spin-less density construct is then inserted into the standard Langreth-Lundqvist vdW functional [49, 56]. The total non-local Kohn-Sham potential is then estimated with

$$\nu_\uparrow^{nl} = \nu_\downarrow^{nl} = \nu^{nl} \tag{4.1.2}$$

with $\nu_\uparrow^{nl}$ and $\nu_\downarrow^{nl}$ being the up and down non-local potentials respectively. Here we will refer to this approximation as the spin-sum, while we will refer to our spin generalisation of the vdW-DF as the spin vdW-DF.

In this work we derive and verify that our spin vdW-DF density functional is superior to the naïve spin-sum approximation already set forward [1, 2]. Our approximation is derived from first principles using the adiabatic connection formula in Section 4.2. In Section 4.4.1 we apply our method to the closed shell system of $(N_2)_2$. In Sections 4.4.2 and 4.4.3 we apply our version as well as the spin-sum approximation to the open shell systems of $(O_2)_2$ and the phenalenyl dimer. The results of these sections confirm that our spin vdW-DF returns more accurate results than the spin-sum approximation for real open shell systems.

4.2 Theory

Fundamentally our spin generalisation follows the derivation of Langreth-Lundqvist [47, 48, 76, 49, 52, 77] with small corrections to ensure the expressions remain valid for spin polarised densities. To begin with the derivation follows the adiabatic connection fluctuation dissipation theory, relating the exact exchange and correlation energy to the spin-density spin-density response function. This ensures that correlated charge fluctuations in the spin-densities are included in the functional, as required for dispersion interactions.

4.2.1 Adiabatic connection fluctuation dissipation

The aim of the adiabatic connection is to link the fully interacting and the non interacting Hamiltonians and subsequently obtain an expression for the exact exchange and correlation energy. We include a derivation of this, which follows Harris [73], as it introduces our notation system.

Our Hamiltonian is a system of electrons interacting via the Coulomb interaction and moving in an external spin dependent potential. If we define

$$\hat{v} = \sum_{\alpha\beta} \int w_{\alpha\beta}(\mathbf{r}) \psi^{\dagger}_{\alpha}(\mathbf{r}) \psi_{\beta}(\mathbf{r}) \tag{4.2.1}$$

where $w_{\alpha\beta}$ is the external potential, $\psi^{\dagger}$ and ψ are the electron creation and annihilation operators, respectively, and the indices α and β denote a Pauli 2×2-matrix notation [21, 78] the Hamiltonian reads,

$$\hat{H} = \hat{T} + \hat{v} + \hat{U} \tag{4.2.2}$$

where $\hat{T}$ and $\hat{U}$ are the kinetic energy and the electron-electron interaction operators. If we define the (2×2) spin density matrix as

$$n_{\alpha\beta}(\mathbf{r}) = \langle \psi^{\dagger}_{\beta}(\mathbf{r}) \psi_{\alpha}(\mathbf{r}) \rangle, \tag{4.2.3}$$

we can then write the *scalar total density* as

$$n(\mathbf{r}) = \sum_{\alpha\beta} n_{\alpha\beta}(\mathbf{r}). \tag{4.2.4}$$

Let us introduce a fictitious system with the same number of electrons but in which the Coulomb interactions are scaled by a factor $0 \leq \lambda \leq 1$. To ensure our auxiliary system gives the same ground state density, the external potential must also depend on this coupling constant. By ensuring that the *total* density, $n(\mathbf{r})$, remains the same for all values of λ we are operating under the *spin restricted KS-DFT formulation* [79]. The coupling constant dependent external potential is denoted V^{λ} and the Hamiltonian becomes

$$\hat{H}_{\lambda} = \hat{T} + V^{\lambda} + \lambda \hat{U}. \tag{4.2.5}$$

With $\lambda = 0$ our system is reduced to the non-interacting Kohn-Sham system with $V^{\lambda=0} = v + v_H + v_{xc}$, where v_H and v_{xc} are the Hartree and exchange and correlation potentials. In the fully interacting limit we get $V^{\lambda=1} = v$. If we denote Ψ^{λ} as the ground state N-particle many-body wave-function of $\hat{H}_{\lambda}$, then via the Hellmann-Feynmann theorem we get the dependence of the energy on the coupling constant

$$\frac{dE(\lambda)}{d\lambda} = \frac{d}{d\lambda} \langle \Psi^{\lambda} | \hat{H}_{\lambda} | \Psi^{\lambda} \rangle = \langle \Psi^{\lambda} | \hat{U} | \Psi^{\lambda} \rangle + \langle \Psi^{\lambda} | \frac{\partial V^{\lambda}}{\partial \lambda} | \Psi^{\lambda} \rangle. \tag{4.2.6}$$

Integrating this over λ gives

$$E_{\lambda=1} = E_{\lambda=0} + \int_0^1 d\lambda \langle \Psi^\lambda | \hat{U} | \Psi^\lambda \rangle - \int d\mathbf{r} n(\mathbf{r})[v_H + v_{xc}]. \tag{4.2.7}$$

Evaluating equation (4.2.5) for the non-interacting case, $\lambda = 0$, and interacting cases give the energy expressions,

$$\begin{aligned} E_{\lambda=0} &= T_0 + \int d\mathbf{r} n(\mathbf{r}) V^{\lambda=0}(\mathbf{r}) \\ E_{\lambda=1} &= T_0 + E_H + E_{xc} + \int d\mathbf{r} n(\mathbf{r}) V^{\lambda=1}(\mathbf{r}) \end{aligned} \tag{4.2.8}$$

with T_0 being the non-interacting kinetic energy. Applying these two expressions to equation (4.2.7) yields

$$E_H + E_{xc} = \int_0^1 d\lambda \langle \Psi^\lambda | \hat{U} | \Psi^\lambda \rangle. \tag{4.2.9}$$

Importantly this is independent of the external potential depending only on our treatment of the internal interaction, U.

Here we make two assumptions vital to our generalisation of the vdW-DF functional. Firstly we ignore spin-spin interactions. This means our electron-electron interaction operator, U, becomes the non-local Coulomb operator. Secondly we restrict our attention to that of spin-polarised systems with two spin orientations, σ and σ'. This reduces our spin density matrix to diagonal terms only, we denote these two spin densities as n_σ and $n_{\sigma'}$. We now expand the interaction energy in terms of a spin polarised number density operator, $\hat{n}(\mathbf{r}\sigma) = \sum_i \delta(\mathbf{r} - \mathbf{r}_i)\delta_{\sigma\sigma_i}$,

$$\langle \Psi^\lambda | \hat{U} | \Psi^\lambda \rangle = \frac{1}{2} \int d\mathbf{r} d\mathbf{r}' \frac{1}{|\mathbf{r} - \mathbf{r}'|} \sum_{\sigma\sigma'} [\langle \hat{n}(\mathbf{r}\sigma)\hat{n}(\mathbf{r}'\sigma') \rangle_\lambda - \delta(\mathbf{r} - \mathbf{r}')\delta_{\sigma\sigma'} \langle \hat{n}(\mathbf{r}\sigma) \rangle_\lambda] \tag{4.2.10}$$

where $\langle \cdots \rangle_\lambda$ is the expected value for the system in the ground state, Ψ^λ, with coupling

constant λ. This can be succinctly expressed as

$$\langle \Psi^{\lambda} | \hat{U} | \Psi^{\lambda} \rangle = \frac{1}{2} \int d\mathbf{r} d\mathbf{r}' \frac{1}{|\mathbf{r} - \mathbf{r}'|} \sum_{\sigma\sigma'} n_2^{\lambda}(\mathbf{r}\sigma, \mathbf{r}'\sigma') \tag{4.2.11}$$

where we have defined $n_2^{\lambda}(\mathbf{r}\sigma, \mathbf{r}'\sigma') = \langle \hat{n}(\mathbf{r}\sigma)\hat{n}(\mathbf{r}'\sigma') \rangle_{\lambda} - \delta(\mathbf{r} - \mathbf{r}')\delta_{\sigma\sigma'}\langle \hat{n}(\mathbf{r}\sigma) \rangle_{\lambda}$ as the pair probability density. Using the definition of the density fluctuation operator, $\delta\hat{n}(\mathbf{r}\sigma) = \hat{n}(\mathbf{r}\sigma) - n(\mathbf{r}\sigma)$, the pair density becomes

$$n_2^{\lambda}(\mathbf{r}\sigma, \mathbf{r}'\sigma') = \langle \delta\hat{n}(\mathbf{r}\sigma)\delta\hat{n}(\mathbf{r}'\sigma') \rangle_{\lambda} + \delta(\mathbf{r} - \mathbf{r}')\delta_{\sigma\sigma'}n(\mathbf{r}\sigma) + n(\mathbf{r}\sigma)n(\mathbf{r}'\sigma'). \tag{4.2.12}$$

By applying the fluctuation-dissipation theorem [80] to the expectation term we can express the pair density in terms of the density-density response function,

$$\langle \delta\hat{n}(\mathbf{r}\sigma)\delta\hat{n}(\mathbf{r}'\sigma') \rangle_{\lambda} = -\frac{1}{\pi} \int_0^{\infty} du\, \chi_{\sigma\sigma'}^{\lambda}(r, r'; iu) \tag{4.2.13}$$

with the response function*, $\chi_{\sigma\sigma'}^{\lambda}$, expressed in terms of the imaginary frequency, iu. Subtracting off the Hartree term from equation (4.2.9) and applying equations (4.2.11),(4.2.12),(4.2.13) gives the exact exchange and correlation energy

$$E_{xc} = -\frac{1}{2\pi} \int_0^1 d\lambda \int_0^{\infty} du Tr[V \sum_{\sigma\sigma'} \chi_{\sigma\sigma'}^{\lambda}(r, r'; iu)] + E_{self} \tag{4.2.14}$$

where V is the Coulomb potential $\frac{1}{|\mathbf{r}-\mathbf{r}'|}$. E_{self} is the energy from the term $\delta(\mathbf{r} - \mathbf{r}')\delta_{\sigma\sigma'}n(\mathbf{r}\sigma)$, the "self-interaction" energy of a particle with itself through the Coulomb interaction [81].

From the application of linear response theory to time dependent density func-

*while this should be referred to as the spin-density spin-density response function, as it relates the charge fluctuations of the spin-densities, the term density density response or density response function will be mainly used in this work. These terms help reinforce our starting assumption to neglect spin-spin interactions as well spin charge interactions, the later being omitted due to the zero external magnetic field.

tional theory (TDDFT) [82] it is possible to obtain expressions relating the interacting and non-interacting response functions [83].

Petersilka *et al.* [83] link the noninteracting response, χ^0, to the response at an arbitrary coupling constant, χ^λ, with a Dyson-type equation. Following the approach of Dion [84] we write Petersilkas expression in the form of two identities,

$$\begin{aligned} \chi^\lambda &= \tilde{\chi}^\lambda + \tilde{\chi}^\lambda * (\lambda V) * \chi^\lambda \\ \tilde{\chi}^\lambda &= \chi^0 + \chi^0 * (f_{xc}^\lambda) * \tilde{\chi}^\lambda \end{aligned} \tag{4.2.15}$$

where $A * B$ denotes the convolution operation and f_{xc}^λ denotes the kernel $f_{xc}^\lambda = \frac{\delta v_{xc}^\lambda(r,t)}{\delta n(r',t')}$. $\tilde{\chi}^\lambda$ is the response to the screened potential. However the screened response function requires knowledge of the kernel f_{xc}^λ whose exact form is unknown.

Under the random phase approximation (RPA) [85]* the screened response is approximated with the non interacting response, $\tilde{\chi}^\lambda \simeq \chi^0$. Here we follow the approach of Dion *el al.* [49] and apply the full potential approximation (FPA†) [84], which uses the fully interacting response $\tilde{\chi}^\lambda \simeq \chi^{\lambda=1}$. Inserting this into equation (4.2.15) and generalising to include spin gives,

$$\chi_{\sigma\sigma'}^\lambda = \chi_{\sigma\sigma'}^{\lambda=1} + \sum_{\nu\nu'} \chi_{\sigma\nu}^{\lambda=1} * \lambda V * \chi_{\nu'\sigma'}^\lambda \tag{4.2.16}$$

This can be rearranged to give‡,

$$\sum_{\sigma\sigma'} \chi_{\sigma\sigma'}^\lambda = \sum_{\sigma\sigma'} \chi_{\sigma\sigma'}^{\lambda=1} \left(1 - \sum_{\nu\nu'} \chi_{\nu\nu'}^{\lambda=1} * [\lambda V]\right)^{-1} \tag{4.2.17}$$

*See Section 3.7

†See Appendix B

‡see Appendix B for a more thorough explanation of this rearrangement

Applying this to equation (4.2.14) gives,

$$E_{xc} = -\frac{1}{2\pi}\int_0^1 d\lambda \int_0^\infty du\, Tr[(1 - \sum_{\nu\nu'} \lambda V \chi^{\lambda=1}_{\nu\nu'})^{-1} \sum_{\sigma\sigma'} V\chi^{\lambda=1}_{\sigma\sigma'}] + E_{self} \tag{4.2.18}$$

or more succinctly as *

$$E_{xc} = \int_0^\infty \frac{du}{2\pi}\, Tr[Ln(1 - \sum_{\sigma\sigma'} V\chi^{\lambda=1}_{\sigma\sigma'})] + E_{self}, \tag{4.2.19}$$

where Tr denotes the trace operator and Ln the natural log. Here we have also changed the ν and ν' indices to σ and σ'. For clarity we shall discard the $\lambda = 1$ superscript and accept that all subsequent response functions are to be calculated using the full Coulomb interaction.

Similarly to Dion *et al.* we want to split the correlation into local and non-local parts. Where the local coorelation part can reasonably be captured by local density functionals and the non-local part catches everything else. In doing this we can treat both parts to differing levels of approximation.

$$E_{xc}[n] = E^0_{xc}[n] + E^{nl}_c[n] \tag{4.2.20}$$

Firstly we define the external potential as

$$\phi^{ext}_\sigma(\mathbf{q},\omega) = V(\mathbf{q}) n^{ext}_\sigma(\mathbf{q},\omega), \tag{4.2.21}$$

where $V(\mathbf{q}) \equiv 4\pi e^2/q^2$. The density fluctuations resulting from such a field can

*Here we have used the identity

$$\frac{dLn(1+a\lambda)}{d\lambda} = \frac{a}{1+a\lambda}$$

be written in two equivalent forms*

$$\delta n_\sigma = \sum_{\sigma'} \chi_{\sigma\sigma'} \phi^{ext}_{\sigma'} \tag{4.2.22a}$$

$$\delta n_\sigma = -\boldsymbol{\nabla}.\mathbf{P}_\sigma, \tag{4.2.22b}$$

with $\mathbf{P}_\sigma$ being the polarisation density. We can relate the polarisation density to the external electric field, $\mathbf{E}^{ext}$. This field is from the sum of the external potentials, that is,

$$\mathbf{E}^{ext} = -\boldsymbol{\nabla}\left(\sum_\sigma \phi^{ext}_\sigma\right) \tag{4.2.23}$$

The relationship between the external field and the polarisation is through the dielectric constant, ϵ_σ. We generalise this to an anisotropic material, and so the dielectric constant becomes a rank-2 tensor, $\boldsymbol{\epsilon}_\sigma$, with elements $\epsilon^{\alpha\beta}$ where $\alpha, \beta \in \{x, y, z\}$. A linear approximation for the polarisation density gives,

$$\mathbf{P}_\sigma = \epsilon_0(\boldsymbol{\epsilon}_\sigma - \mathbf{1}).\mathbf{E}^{ext}, \tag{4.2.24}$$

where ϵ_0 is the electric permittivity of free space and $\mathbf{1}$ is the 3×3 identity matrix. Applying this to equation (4.2.22b) and equating to (4.2.22a) gives,

$$\boldsymbol{\nabla}.\epsilon_0(\mathbf{1} - \boldsymbol{\epsilon}_\sigma).\boldsymbol{\nabla}\phi^{ext} = \sum_{\sigma'} \chi_{\sigma\sigma'} \phi^{ext}_{\sigma'}. \tag{4.2.25}$$

*A similar spin dependent density-density response function is used by Kanjouri *et al.* [86]. The important point here is that while our notation indicates a spin dependent external potential this is a *Coulomb* field resulting from the density fragment n_σ.

As $\phi = \sum_{\sigma'} \phi_{\sigma'}$ this reduces to,

$$\boldsymbol{\nabla}.\epsilon_0(\mathbf{1} - \boldsymbol{\epsilon}_\sigma).\boldsymbol{\nabla} = \sum_{\sigma'} \chi_{\sigma\sigma'}. \tag{4.2.26}$$

Inserting this into equation (4.2.19) gives,

$$E_{xc} = \int_0^\infty \frac{du}{2\pi} Tr[Ln(1 - \boldsymbol{\nabla}.\epsilon_0(\mathbf{1} - \sum_\sigma \boldsymbol{\epsilon}_\sigma).\boldsymbol{\nabla}V)] + E_{self}, \tag{4.2.27}$$

In the uniform density limit $\boldsymbol{\epsilon}_\sigma$ becomes constant and isotropic, such that $\epsilon_\sigma^{xx} = \epsilon_\sigma^{yy} = \epsilon_\sigma^{zz} \equiv \epsilon_\sigma$ are the only non-zero tensor elements. Applying this to equation (4.2.19) and using the identity (4.2.26) gives the local exchange and correlation density,

$$E_{xc}^0 = -\int_0^\infty \frac{du}{2\pi} \int_0^1 \frac{d\lambda}{\lambda} Tr[1 - (\sum_\sigma \epsilon_\sigma)^{-1}] - E_{self} \tag{4.2.28}$$

Subtracting E_{xc}^0 from equation (4.2.19) and again applying equation (4.2.26) gives the non-local correlation energy.

$$E_c^{nl} = \int_0^\infty \frac{du}{2\pi} Tr[Ln(\sum_\sigma \boldsymbol{\nabla}.\epsilon_0\boldsymbol{\epsilon}_\sigma.\boldsymbol{\nabla}G) - Ln(\sum_{\sigma'} \epsilon_{\sigma'})] \tag{4.2.29}$$

where G is the Coulomb Green's function.

In his thesis, Rydberg expresses equation (4.2.29) in terms of a series using a polarisation operator [76]. As before we follow this machinery generalising the method to include spin polarised densities. Firstly we write equation (4.2.29) as

$$E_c^{nl} = \int_0^\infty \frac{du}{2\pi} Tr[Ln(1+\Delta)] \tag{4.2.30}$$

where we have defined*

$$\Delta = (\sum_{\sigma'} \boldsymbol{\epsilon}_{\sigma'})^{-1}[\boldsymbol{\nabla}, \epsilon_0 \sum_{\sigma} \boldsymbol{\epsilon}_{\sigma}].\boldsymbol{\nabla} G. \tag{4.2.31}$$

By taking advantage of the definition of a Green's function, $\nabla^2 G = 1$. The idea behind Rydbergs method is to express Δ in terms of a generalised spin density polarisation operator, S_σ. This operator can then be approximated with a model based on the local density [84, 76]. A simple definition of S_σ,

$$\sum_{\sigma} S_\sigma[n] = Ln(\sum_{\sigma} \boldsymbol{\epsilon}_\sigma[n]) \tag{4.2.32}$$

would make E_{xc}^0, equation (4.2.28) integrated over λ, linear in S_σ. Equation (4.2.29) can also be expressed in terms of S_σ by the series,

$$\Delta = \sum_{n=1}^{\infty} \frac{1}{n!} \mathbf{d}_n.\mathbf{d}_0 G \tag{4.2.33}$$

where

$$\mathbf{d}_{n+1} = [\sum_{\sigma} S_\sigma, \mathbf{d}_n] \tag{4.2.34}$$

with the starting condition $\mathbf{d}_0 = \boldsymbol{\nabla}$. Where we take the series expression from Rydberg *et al.* [76] replacing their polarisation operator with a spin density polarisation operater which we have yet to define. From here we follow the work of Rydberg *et al.*

*With $[\hat{A}, \hat{B}]$ being the commutator between the two operators $\hat{A}$ and $\hat{B}$.

[76]. We expand the logarithm to second order,

$$Tr[Ln(1+\Delta)] \approx Tr[\Delta] - \frac{1}{2}Tr[\Delta^2] + \mathcal{O}(\delta^3) \tag{4.2.35}$$

Evaluating the expressions gives

$$Tr[Ln(1+\Delta)] \approx Tr[\frac{1}{2}\sum_{\sigma\sigma'}[S_\sigma S^*_{\sigma'} - S_\sigma T S^*_{\sigma'} T]] \tag{4.2.36}$$

Inserting equation (4.2.36) into equation (4.2.30) and expanding in plane waves gives

$$E_c^{nl} = \frac{\hbar}{4\pi}\sum_{\sigma\sigma'\mathbf{q}_1\mathbf{q}_2}\int_0^\infty du(1-(\hat{\mathbf{q}}_1.\hat{\mathbf{q}}_2)^2)S_\sigma^{\mathbf{q}_1,\mathbf{q}_2}S_{\sigma'}^{\mathbf{q}_2,\mathbf{q}_1} \tag{4.2.37}$$

taking the plasmon-pole model for S_σ from Dion *et al* [49] with

$$S_\sigma^{\mathbf{q}_1,\mathbf{q}_2} = \frac{1}{2}[\tilde{S}_\sigma^{\mathbf{q}_1,\mathbf{q}_2} + \tilde{S}_\sigma^{-\mathbf{q}_1,-\mathbf{q}_2}] \tag{4.2.38}$$

where S_σ is in plane wave format and

$$\tilde{S}_\sigma^{\mathbf{q}_1,\mathbf{q}_2} = \int d^3r e^{-i(\mathbf{q}_1-\mathbf{q}_2).\mathbf{r}}\frac{\omega_{p\sigma}}{[\omega+\omega_\sigma^{q_1}(\mathbf{r})][-\omega+\omega_\sigma^{q_2}(\mathbf{r})]} \tag{4.2.39}$$

Alternatively expressing this in terms of the kernel function.

$$E_c^{nl} = \frac{1}{2}\sum_{\sigma\sigma'}\int\int d^3r d^3r' n_\sigma(\mathbf{r})\phi_{\sigma\sigma'}(\mathbf{r},\mathbf{r}')n_{\sigma'}(\mathbf{r}') \tag{4.2.40}$$

We expand on this rearrangement in the Appendix C. It is important to note here that this is the same kernel function of Dion *et al.* [49]. As the kernel, $\phi_{\sigma\sigma'}(\mathbf{r},\mathbf{r}')$, not only depends on the separation between the density fragments but also their density

gradients and magnitudes, our kernel depends on the spin-densities. In Appendix D, we show how the Soler method [77] for efficiently solving the functional also removes the spin-density dependence. The result of this is a spin polarised version of the vdW-DF which can still utilise the same pre-computed kernel values as Soler.

4.3 Computational Methods

We have implemented our spin polarised generalisation of the Langreth-Lundqvist vdW density functional [49], equation (4.2.40), in the Quantum Espresso electronic structure code [87]. Our code is fully self consistent and uses the efficient Soler algorithm [77] to calculate the vdW energy.

We evaluate our kernel using a mesh of 20 points for each spin direction. The mesh is comprised of pre-computed values of the function $q_\sigma^0(n_\sigma(\mathbf{r}), |\boldsymbol{\nabla} n_\sigma(\mathbf{r})|)$, equation (C.1.4). Soler pre-calculates and tabulates the kernel function at each of these points. At run time interpolating functions are built allowing the evaluation of the kernel at any q value [77]. By constructing spin dependent interpolating functions, see Appendix D, we can make use of the same precomputed table of kernel values as Soler.

For all the calculations in this chapter we used the rigid rotator model [88, 89]. In this method the intra-molecular geometries are fixed and the inter-molecular distances and relative rotation angles are varied. We fixed the intra-molecular distances for the $(N_2)_2$ and $(O_2)_2$ dimers at the experimental gas phase distances, 1.098 Å for the N_2 dimer and 1.208 Å for the O_2 [90]. The phenalenyl molecular geometries were fixed at their optimised positions. These positions were calculated with our spin vdW-DF functional, see Appendix A for these coordinates.

All calculations were carried out in cubic simulation cells of length 25 Bohr. We used a single k point at the Γ point ($k = 0$) as these systems are not periodically

extended. A kinetic energy cutoff of 200 Rydberg was used for the $(N_2)_2$ and $(O_2)_2$ complexes while a 90 Rydberg cutoff was used for the phenalenyl dimers. Troullier-Martins norm conserving pseudopotentials [91] with revPBE [28] exchange and correlation were used. Methfessel-Paxton occupation smearing [10] was used with a broadening of 0.01 Rydberg.

These parameters correspond to errors of less than 1 meV in the inter-monomer interaction energy. This is confirmed with the convergence curves for the inter-monomer binding energy, Figure 4.1.

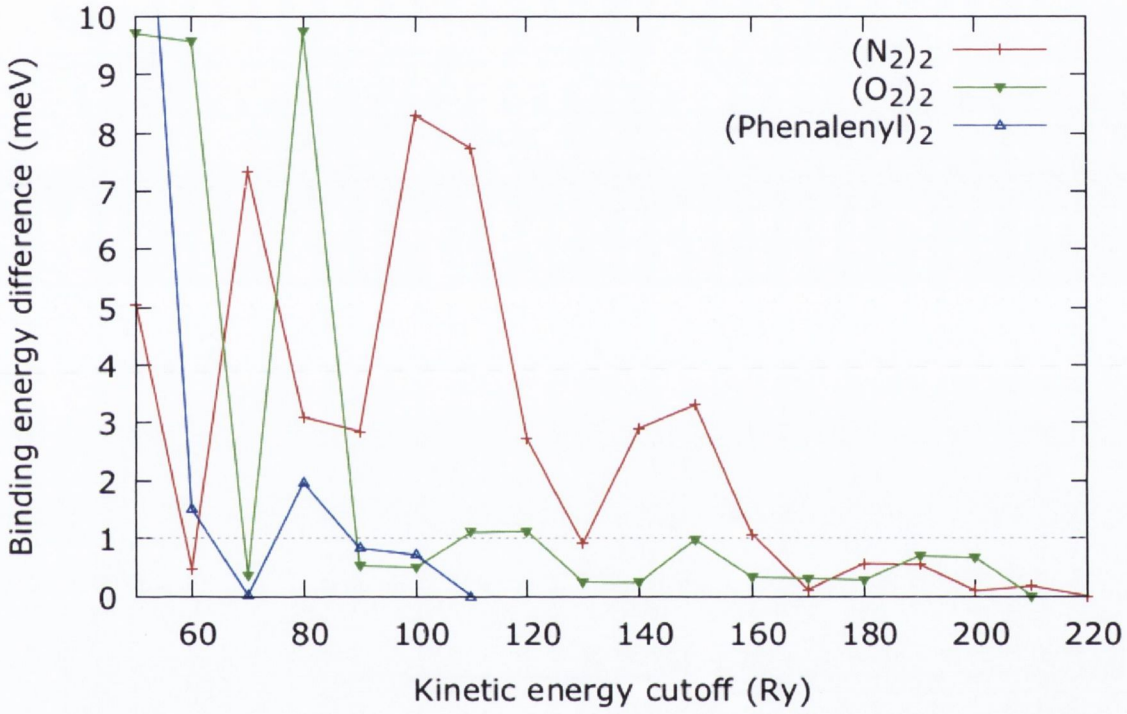


Figure 4.1: Convergence of inter-monomer binding energies - Difference in the inter-monomer binding energies, at various kinetic energy cutoffs, from the binding energy calculated with the max cutoff. A maximum plane wave cutoff of 210 Ry and 220 Ry was used for the $(O_2)_2$ and $(N_2)_2$ complexes respectively. The phenalenyl dimer was calculated with a maximum cut off of 110 Ry. Both the $(O_2)_2$ and $(N_2)_2$ complexes were calculated in the planar 'H' geometry with inter-monomer separations of 4 Å. The phenalenyl dimer was calculated in the fully eclipsed orientation with an inter-monomer separation of 3.3 Å. See Figure 4.2 for a description of the geometries. The binding energies for all the systems were calculated with our spin vdW-DF.

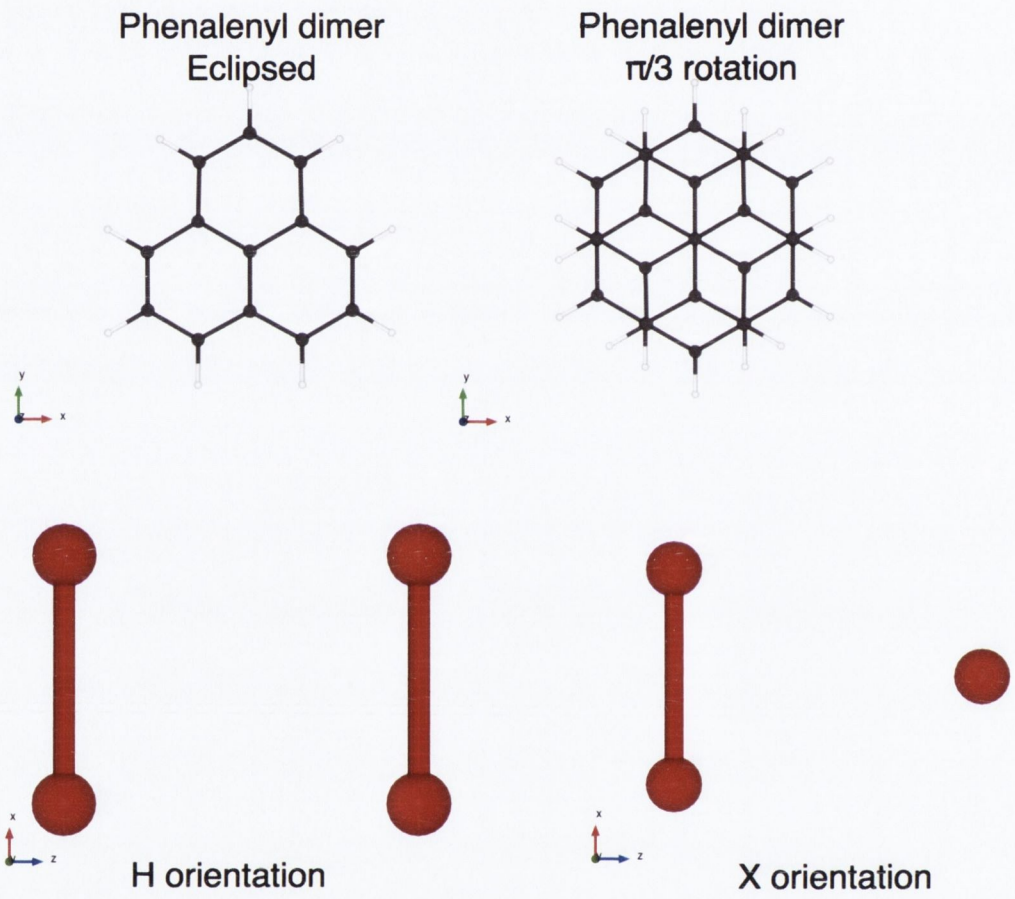


Figure 4.2: Dimer geometries - Shown are the various geometry configurations for the complexes used in this chapter. On the top line are the fully eclipsed and $\pi/3$ rotated configurations of the phenalenyl dimers. The rotation of one molecule by $\pi/3$ relative to the other gives this rotated configuration. The bottom line shows the planar 'H' geometry and the orthogonal 'X' geometry. The 'X' geometry arises from a $\pi/2$ relative rotation of the monomers. We calculate the $(O_2)_2$ complex in both the 'H' and 'X' geometries and the $(N_2)_2$ in just the 'H'.

4.4 Results

To test the validity of our spin vdW-DF functional we require test systems with a rather specific set of attributes. An ideal test system is comprised of isolated neutral sub-fragments with unpaired electrons. By having isolated neutral sub-fragments we ensure the interaction is dispersive in nature. Unpaired electrons give rise to paramagnetic properties in the sub-fragments. With no external magnetic field the magnetic dipoles of the sub-fragments are not expected to interact at long range. This is because thermal agitation acts to keep the magnetic dipoles randomly oriented, reducing their interaction significantly [24]. The lack of external magnetic fields and long range spin interaction define the limits of our theory, as it is around these assumptions that the functional is constructed.

Molecular oxygen has two spin states. Its ground triplet state, S=1, and its excited singlet state, S=0. Two oxygen molecules can, and do, combine to form the vdW complex $(O_2)_2$. The most significant states of the complex are the singlet, S=0, and the quartet, S=0, states corresponding to two ground state molecules forming with spins aligned or anti-aligned. Such interactions are expected to take place high in the atmosphere but have also been replicated and studied in the lab. Interestingly the geometry of the complex depends upon its spin state. In the singlet state the molecules form the planar 'H' shape while in the quartet state the molecules align so their molecular axes are perpendicular forming the 'X' shape. These geometries are shown in Figure 4.2

The complex $(N_2)_2$ is similar to that of the oxygen system except it has no unpaired electrons and its ground state is the singlet, S=0. The complex also forms in the planar 'H' geometry.

The phenalenyl dimer complex provides a second system to test our spin vdW-DF against. The phenalenyl are neutral radicals with unpaired electrons. In the resulting

dimer the molecules create an anti-symmetric state, S=0.

These systems provide excellent test cases for our functional. The $(N_2)_2$ complex provides the means to test that our functional reduces to the standard vdW-DF functional for systems with no spin polarisation. The $(O_2)_2$ and phenalenyl dimer complex meanwhile, test the validity of our no long range spin interactions assumption and allow us to compare the performance of our spin vdW-DF and the spin-sum approximation.

4.4.1 $(N_2)_2$

Figure 4.3 shows the binding energy curves for the $(N_2)_2$ complex. We calculated curves using the standard, non-spin polarised, version of the vdW-DF along with our spin vdW-DF and the spin-sum functionals. Experimental results, Exp., are taken from Aquilanti *et al.* [89]. All these calculations were performed without spin polarisation. The identically overlapping binding curves illustrate that our implementation of both spin vdW approximations correctly reduce to that of the non-spin vdW-DF for non-spin polarised calculations. Table 4.1 summarises the binding energies and inter-molecular distances from the binding curves of Figure 4.3. The table shows the need for calculations with dispersion corrections.

method	bond length (Å)	bond energy (meV)
revPBE	unbound	n/a
spin revPBE	unbound	n/a
vdW-DF	3.91	-9.14
spin-sum	3.90	-7.58
spin vdW-DF	3.88	-7.09
Exp.	3.77	-11.43
CCSD	3.57	-8.92

Table 4.1: Results of $(N_2)_2$ binding curves - Binding energies and distances of the $(N_2)_2$ complex in 'H' geometry. Experimental results, Exp., and coupled cluster results, CCSD, are taken from Aquilanti *et al.* [89]. See figures 4.2 and 4.3 for a description of the geometries and the binding curves. The values were extracted from quadratic functions which had been fitted about the curve minima.

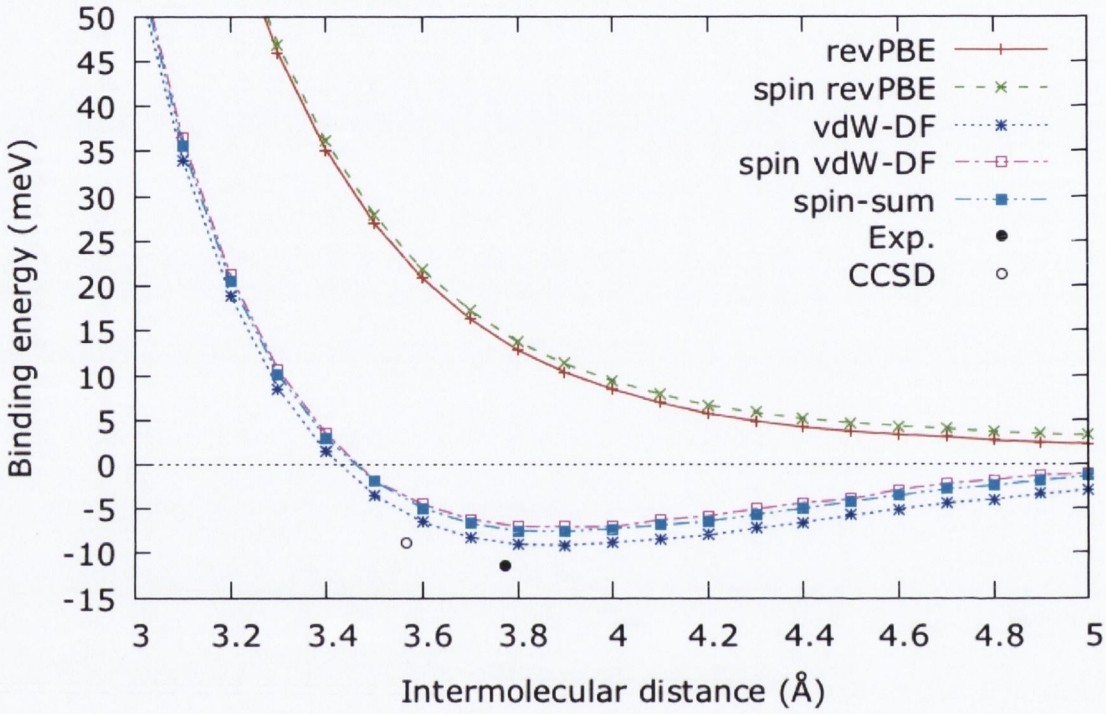


Figure 4.3: $(N_2)_2$ binding curves - Binding energy curves for the $(N_2)_2$ geometry in the planar 'H' geometry. Experimental results, Exp., and coupled cluster results, CCSD, are taken from Aquilanti *et al.* [89]. See Figure 4.2 for a description of the geometry. Binding curves are shown for the revPBE with and without spin (revPBE and spin revPBE respectively), our spin polarised version of the vdW-DF functional (spin vdW-DF), our implementation of the approximate spin vdW-DF (spin-sum) [1, 2] and the non-spin-polarised functional of Dion *et al.* (vdW-DF) [49]. Our spin vdW-DF and the spin-sum methods are in close agreement with each other and bind slightly less than the nonspin, vdW-DF, curve. This is similar to revPBE results which show the binding curve calculated with spin lies higher in energy than the non-spin case. Binding curves calculated using the spin-sum and spin vdW-DF methods without spin are identical to the results of the non-spin vdW-DF and are not shown here. These results are summarised in Table 4.1.

4.4.2 $(O_2)_2$

Figures 4.4 and 4.5 show the binding energy curves for the $(O_2)_2$ complex in both the planar 'H' and orthogonal 'X' geometries. Illustrations for these two geometries are shown in Figure 4.2. The curves are calculated using revPBE, our spin vdW-DF and the spin-sum approximation for both possible spin states of the complex. Experimental results are taken from Bussery *et al.* [88].

Values of the bond length and binding energy are extracted from the binding energy curves by fitting quadratic functions to curves about the minima. The resulting values from this fitting are shown in Table 4.2.

Our results highlight the need for dispersion interactions in calculations of the $(O_2)_2$ complex. The revPBE results show no binding for the 'H' geometry and very small binding for the 'X' geometry.

Our method predicts the same ground state total spin value as found in scattering experiments for both the 'H' and 'X' geometries [88], a zero spin ground state for the 'H' geometry and a quintet, S=2, for the 'X' geometry. Our method also predicts an energy splitting between the spin states similar to those of experiment. Our method returns a splitting of 2.08 meV and 0.13 meV between the two energy levels for the 'H' and 'X' orientations respectively. The experiments of Bussery *et al.* [88] found splittings of 2.84 meV and 0.44 meV, for the 'H' and 'X' geometries.

The spin-sum approximation incorrectly predicts the zero spin state to the ground state of both orientations. It estimates the energy difference between the spin states as 29.6 meV and 15.76 meV for the 'H' and 'X' geometries.

orientation	spin	method	bond length (Å)	bond energy (meV)
H	0	revPBE	unbound	n/a
H	0	spin vdW-DF	3.18	-25.42
H	0	spin-sum	3.18	-58.41
H	0	Exp.	3.53	-17.01
H	2	revPBE	unbound	n/a
H	2	spin vdW-DF	3.51	-23.34
H	2	spin-sum	3.53	-28.81
H	2	Exp.	3.70	-14.17
X	0	revPBE	3.97	-1.70
X	0	spin vdW-DF	3.43	-32.20
X	0	spin-sum	3.41	-48.48
X	0	Exp.	3.61	-15.35
X	2	revPBE	3.97	-1.68
X	2	spin vdW-DF	3.43	-32.07
X	2	spin-sum	3.42	-32.72
X	2	Exp.	3.61	-15.79

Table 4.2: Results of $(O_2)_2$ binding curves - Binding energies and distances of the $(O_2)_2$ complex in 'H' and 'X' geometries for the singlet, S=0, and quintet, S=2, states. Experimental results, Exp., are taken from Bussery *et al.* [88]. See figures 4.2, 4.4 and 4.5 for a description of the geometries and the binding energy curves. The values were extracted from quadratic functions which had been fitted about the curve minima. The curves were calculated using revPBE, our spin vdW-DF and the spin-sum approximation [1, 2]. Both the spin vdW-DF methods qualitatively predicts the correct spin state for the 'H' geometry. While both methods over-estimate the binding energy of both the spin states, our method is significantly more accurate with an error of 8.41 meV compared to an error of 41.4 meV from the spin-sum method for the binding energy of the ground state. This difference in accuracy is reduced for the binding energies of the quintet state in both geometries. For the 'X' geometry the spin-sum method incorrectly predicts the singlet state to be the lower of the two states by 15.76 meV. Our method correctly predicts that the singlet and quintet state lie within 1 meV of each other.

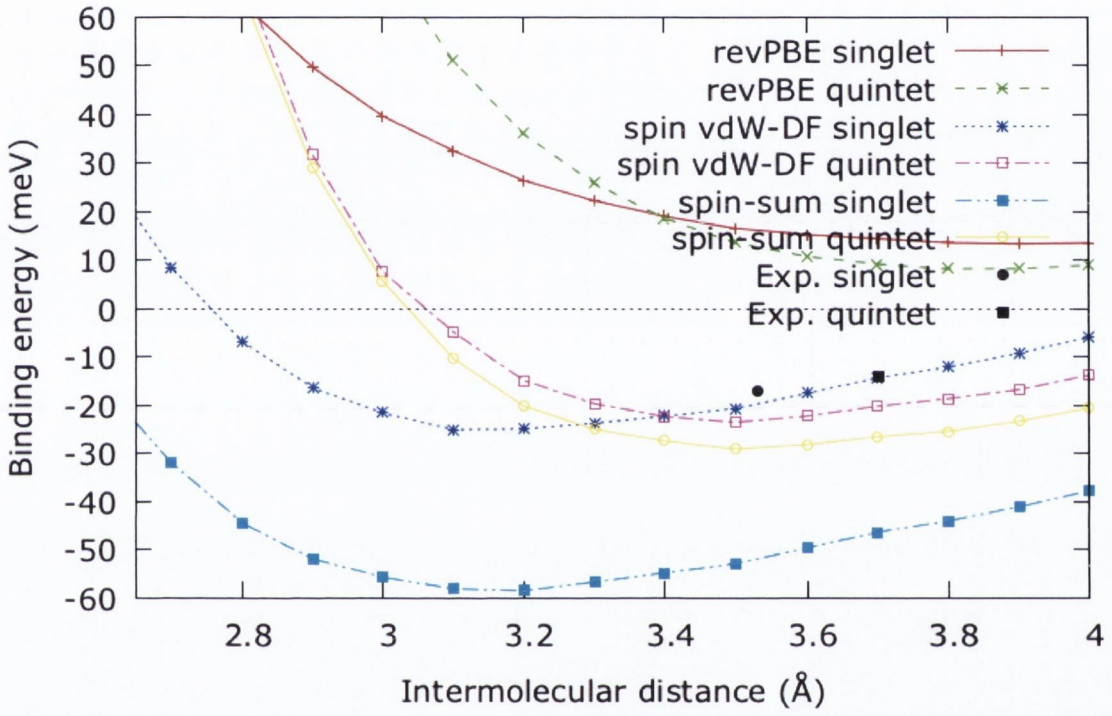


Figure 4.4: $(O_2)_2$ binding curves 'H' geometry - Binding energy curves for the $(O_2)_2$ geometry in the planar 'H' geometry. Binding curves are shown for the singlet, S=0, and quintet, S=2, states. Experimental results, Exp., are taken from Bussery *et al.* [88] and show results for the singlet, a solid black circle, and quintet, solid square, states. See Figure 4.2 for a description of the geometry. The results from the revPBE, our spin vdW-DF functional and our implementation of the spin-sum approximation [1, 2] functionals are shown. The revPBE results show no binding at any distance. While both the spin vdW-DF functionals correctly predict the singlet state as the lower energy state the spin-sum method over-binds, overestimating the binding of the singlet state and consequently the singlet quintet splitting. These results are summarised in Table 4.2.

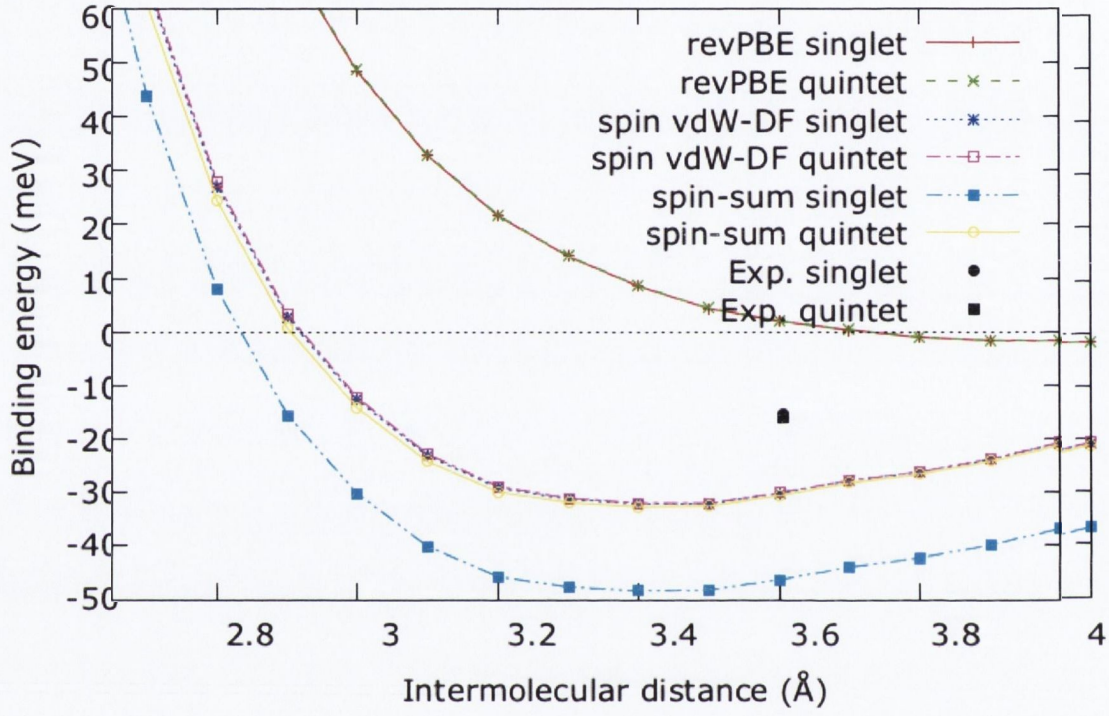


Figure 4.5: $(O_2)_2$ binding curves 'X' geometry - Binding energy curves for the $(O_2)_2$ geometry in the 'X' geometry. Binding curves are shown for the singlet, S=0, and quintet, S=2, states. Experimental results, Exp., are taken from Bussery *et al.* [88] and show results for the singlet, a solid black circle, and quintet, solid square, states. In the figure these points overlap with the energy splitting between the states less than 1 meV. The spin vdW-DF curves for the S=0 and S=2 overlap with the spin-sum curve for the S=2 state on this graph. See Figure 4.2 for a description of the geometry. The results from the revPBE, our spin polarised version of the vdW-DF and our implementation of the spin-sum approximation [1, 2] functionals are shown. Both the revPBE and our spin vdW-DF functionals correctly predict a small energy splitting between the states. The revPBE results show a binding energy of 2 meV at 4 Å. The spin-sum method over estimates the binding energy of the singlet state, incorrectly predicting it as the lowest energy state. These results are summarised in Table 4.2.

4.4.3 Phenalenyl dimer

Figure 4.6 shows the binding energy curves for the phenalenyl dimer as calculated with revPBE, our spin vdW-DF and spin-sum functionals. The orientation of the two dimers in the complex is show in Figure 4.2. Although experimental binding energies and bond lengths for phenalenyl dimer are sensitive to substituent atoms as well as the solvent in which they interact, we include two experimental results here for comparison. The results are for tert-butyl substituted phenalenyl dimers in hexane and dichloromethane and are taken from Kolb *et al.* [1].

Values of the bond length and binding energy are extracted from the binding energy curves by fitting quadratic functions to curves about the minima. The resulting values from this fitting are shown in Table 4.3.

Similar to results of the $(O_2)_2$ complex, both spin versions of the vdW-DF functional overbind with respect to experimental results. The spin-sum approximation overbinds with respect to our spin vdW-DF by 20 meV. Our binding energy for the spin-sum approximation, of 640 meV, is in excellent agreement with the 633 meV value found by Kolb [1]; our calculated binding distance matches with theirs.

method	bond length (Å)	bond energy (eV)
revPBE	3.59	-0.11
spin vdW-DF	3.32	-0.62
spin-sum	3.31	-0.64
Exp. 1	3.23	-0.32
Exp. 2	3.24	-0.41

Table 4.3: Results of phenalenyl dimer binding curves - Binding energies and distances of the phenalenyl dimer in the anti-symmetric, S=0, spin configuration. The values were extracted from quadratic functions which had been fitted about the curve minima. Experimental results, Exp., are taken from Kolb *et al.* [1]. The experimental results, Exp.1 and Exp.2, are dependent on both the solvent and phenalenyl substituents used. Values shown here are for tert-butyl substituted phenalenyl dimers in hexane, Exp.1, and dichloromethane, Exp.2. The dimers were orientated in their 'eclipsed' position. See Figure 4.2 for a description of the geometry. The results shown are for our spin vdW-DF, the spin-sum and revPBE functionals. These show the importance of vdW corrections for the dimer as the revPBE results under-bind, with respect to the experimental values. Similarly to the O_2 dimer results, Figures 4.4, 4.5 and Table 4.2, the spin-sum method binds more strongly than that of our spin vdW-DF method.

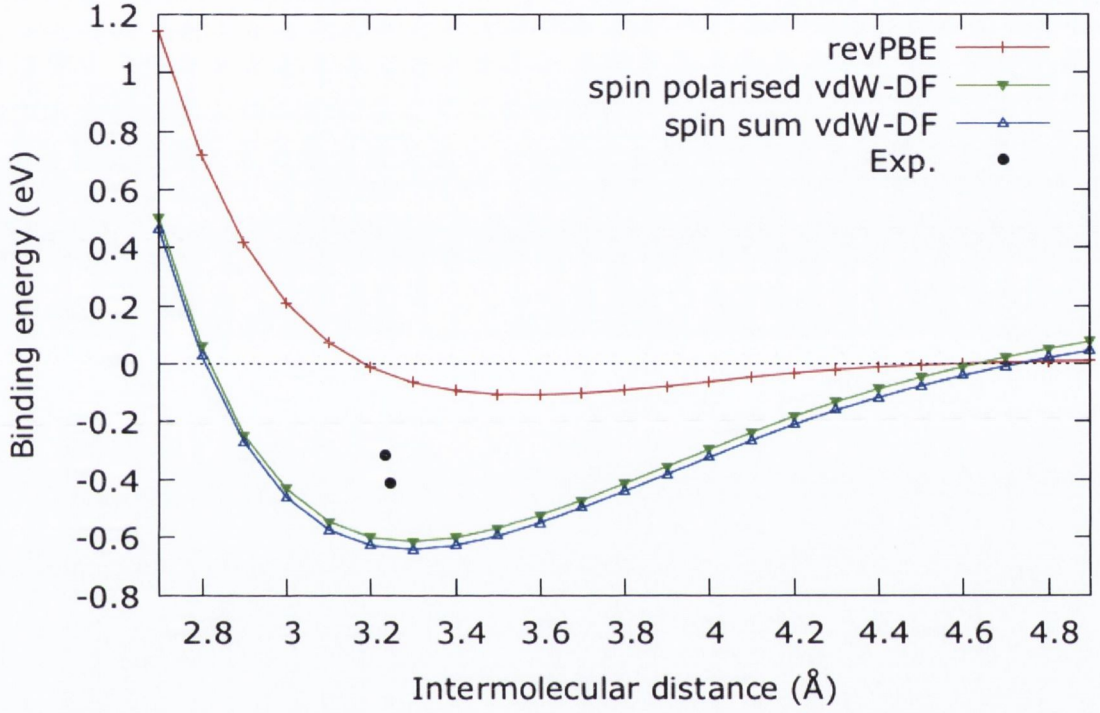


Figure 4.6: Phenalenyl dimer binding energy curves - Binding energy curves of the Phenalenyl dimer in the anti-symmetric, S=0, spin configuration. Experimental results, Exp., are taken from Kolb *et al.* [1]. The experimental results are dependent on both the solvent and phenalenyl substituents used. Values shown here are for tert-butyl substituted phenalenyl dimers in hexane, upper value, and dichloromethane, lower value. The dimers were orientated in their 'eclipsed' position. See Figure 4.2 for a description of the geometry. The binding curves shown are for our spin vdW-DF, the spin-sum and revPBE functionals. The revPBE results under-bind, with respect to the experimental values, while the vdW-DF based functionals give binding energies and distances closer to experiment. Similarly to the O_2 dimer results, Figures 4.4, 4.5 and Table 4.2, the spin-sum method binds more strongly than that of our spin vdW-DF method. These results are summarised in Table 4.3.

4.5 Conclusions

We have presented our spin generalisation of the Langreth-Lundqvist vdW-DF density functional. Based on the adiabatic connection fluctuation dissipation theory it is an *ab initio* based method for the calculation of dispersion interactions in open shell systems. Our results presented here for the $(N_2)_2$ and $(O_2)_2$ complexes as well as the phenalenyl dimer shows that our method provides more accurate binding energy results than the previously proposed spin-sum method [1, 2].

The reason for this continued overbinding by the spin-sum method is due to how it calculates the dispersion interaction. The ab initio derivation of our spin vdW-DF function shows that the interaction of spin densities should be accomplished by summing up the interactions between each pair of spin densities. The results in this chapter support this concept by showing the spin-sum functional overbinding compared to our spin vdW-DF. To confirm this is true for all spin polarised dispersion interactions we define the energy difference between the two methods as,

$$\Delta E = E_{spin-sum} - E_{spinvdW-DF} \tag{4.5.1}$$

where $E_{spin-sum}$ is the spin-sum interaction energy and E_{vdW-DF} is the energy from our spin vdW-DF. By fixing both the total energies of the two interacting spin densities as well as their separation we can calculate the difference in the interaction energies between the two methods. In Figure 4.7 we plot the energy difference between two densities, fixed at a distance of 4 Å and each with total densities of 6 electrons per unit volume*.

Figure 4.7 shows that for all values of the spin polarisation the spin-sum interaction energy will always be greater than our spin vdW-DF. The difference is at a minimum

*We consider the points as having infinitesimal volume.

when both densities are spin un-polarised, $P = 0$ or purely polarised, $P = 1$, systems. At $P = 0$ there are equal number of up and down spins, as would be found in a closed shell system. The difference is greatest for spin polarised densities just off from $P = 0$, such densities are found in open shell systems. Our results for the $(N_2)_2$, $(O_2)_2$ and phenalenyl dimer systems are in line with these results. We found significant differences between the spin-sum and our spin vdW-DF methods for the open shell systems but not for the closed shell $(N_2)_2$.

This can be seen in the binding energy curves of the phenalenyl dimer, Figure 4.6, as well as the singlet energy curves for the $(O_2)_2$ complex, Figures 4.4 and 4.5. The energy difference is smallest as the spin polarisation approaches 1. This can be seen in the energy curves for the $(O_2)_2$ quintet state.

Figure 4.8 shows how the energy difference, ΔE, between the spin vdW-DF and spin-sum methods depends upon the separation of the interacting fragments. At larger fragment separations, the difference between the dispersion energies calculated with the two methods is reduced. The rate of this reduction is independent of the spin polarisation of the fragments.

This dependence can been seen in the $(O_2)_2$ complex by comparing the energy difference between the two methods for the S=0 and S=2 states in both the 'H' and 'X' geometry configurations. The inter-molecular separation between the atoms increases as we move from the 'H' to the 'X' configurations, as such we expect the dispersion energies as calculated with the spin vdW-DF and spin-sum methods to lie closer for the 'X' geometry configuration than for the 'H'. Table 4.2 shows that the energy difference of spin vdW-DF and spin-sum methods for the S=0 state is 32.99 meV and 16.28 meV for the 'H' and 'X' configurations respectively. In the S=2 state the energy difference is 5.47 meV and 0.75 meV for the 'H' and 'X' configurations respectively.

In summary, our spin vdW-DF is a desirable alternative to the approximate spin-sum method. We have presented a rigorous derivation based on a generalisation of the Langreth-Lundqvist vdW-DF functional. We have shown that for closed shell systems, such as the $(N_2)_2$ complex, our spin vdW-DF and the spin-sum methods are similar. Both methods are in close agreement to the non-spin vdW-DF for spin polarised calculations and congruent with the non-spin vdW-DF for calculations without spin. For the $(O_2)_2$ system we have shown that our spin vdW-DF predicts the correct ground state spin for both geometries considered. Our method also predicts the energy separation between the spin states in close agreement with experimental results. The spin-sum method fails in both of these points, incorrectly predicting a much more strongly bound singlet state for both geometries and consequently predicting a spin state energy splitting much larger than experiment. Our results of the phenalenyl dimer shows that both spin vdW methods give results in reasonable agreement to experimental values.

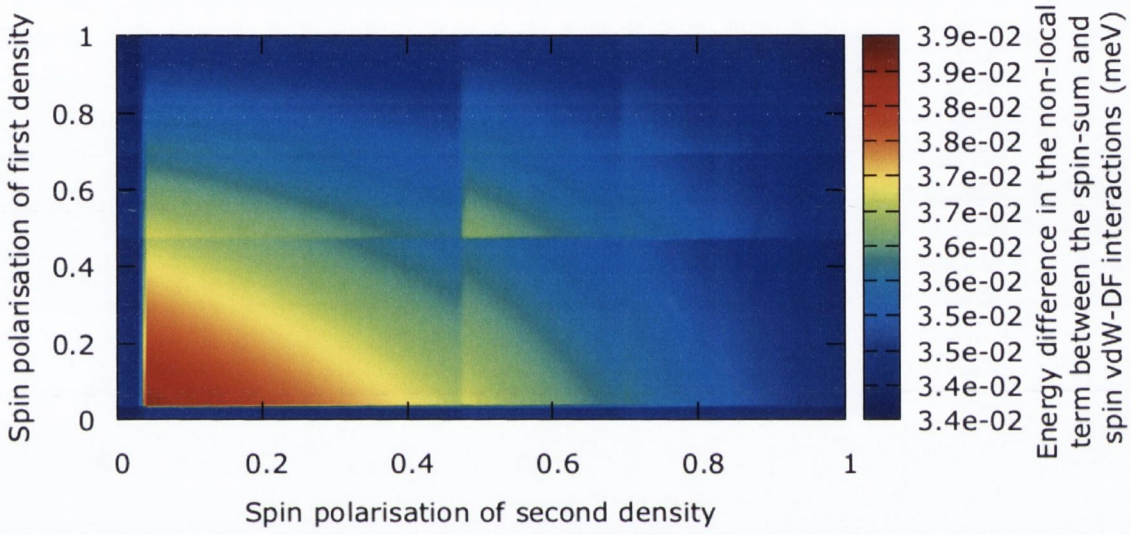


Figure 4.7: Energy difference in the non-local term between the spin-sum and spin vdW-DF interactions - This shows the energy difference in the non-local dispersion interaction between two spin densities, as calculated with the spin-sum and spin vdW-DF functionals. We define the spin polarisation as $P = (n_\uparrow - n_\downarrow)/(n_\uparrow + n_\downarrow)$. We fix the distance between the two densities at 4 Å and the total number of electrons, of both up and down spin, at each point to be 6. We have ignored density gradient corrections. The energy difference is defined as the difference between the spin-sum and the spin vdW-DF methods. The figure shows that the spin-sum interaction energy will always be greater than our spin vdW-DF. The difference is at a minimum when both densities are spin un-polarised, $P = 0$ or purely polarised, $P = 1$, systems. At $P = 0$ there are equal number of up and down spins, as would be found in a closed shell system. The difference is greatest for spin polarised densities slightly greater than $P = 0$, such densities are found in open shell systems. Our results for the $(N_2)_2$, $(O_2)_2$ and phenalenyl dimer systems are in line with these results. We found significant differences between the spin-sum and our spin vdW-DF methods for the open shell systems but not for the closed shell $(N_2)_2$.

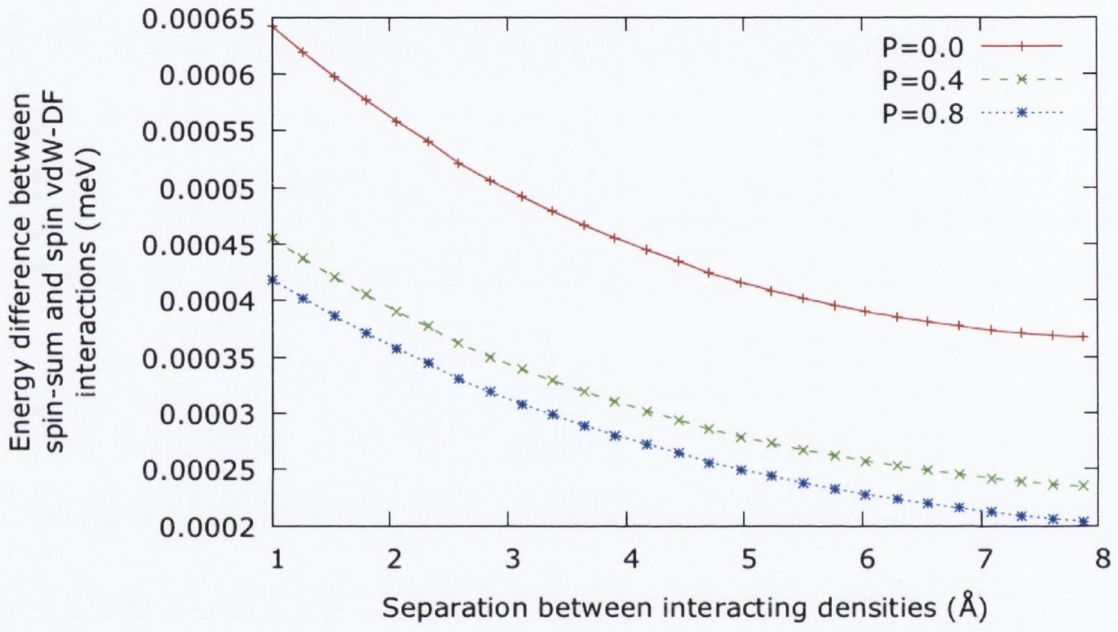


Figure 4.8: Energy difference in the non-local term between the spin-sum and spin vdW-DF interactions for increasing interaction distances - This shows the energy difference in the non-local dispersion interaction between two spin densities, as calculated with the spin-sum and spin vdW-DF functionals. We define the spin polarisation as $P = (n_\uparrow - n_\downarrow)/(n_\uparrow + n_\downarrow)$. The distance between the two densities varies from 1 to 8 Å and the total number of electrons, of both up and down spin, at each point to be 6. We have ignored density gradient corrections. The energy difference is defined as the difference between the spin-sum and the spin vdW-DF methods. The figure shows that the energy difference between the two methods decreases with increasing density separations. It shows that this decrease is independent of spin polarisation, with the three curves decreasing at similar rates.

Chapter 5

An examination of the accuracy of vdW-DF binding energies, as calculated within an atom centered basis set, over the S22 molecular database.

5.1 Introduction

Can the binding energy be used as a measure of the quality of a calculation? There are a number of factors which go into correctly, or accurately, calculating the binding energy. These factors range from using the correct geometries, to the accuracy at which our computational methods work at and also include the accuracy obtainable within a given theory. While the error in the final result is a single value each of these factors interact in a dynamic non-trivial fashion to give this. Determining how these

factors affect the overall accuracy is important, giving us a deeper understanding of these methods as well as how they can be combined.

In this chapter we shall explore how using an atom centered basis set with the vdW-DF functional [49] affects the accuracy of calculated binding energies. While there has been a lot of attention paid to the accuracy of both the original vdW-DF functional as well as the improved versions [57, 58, 56, 59], this has been primarily focused on how changes to composition of the exchange and correction functional affect the accuracy of this method. Additionally many of these analyses have been restricted to plane wave basis sets. The disadvantage of such methods is that such calculations scale cubicly with the size of the system [92, 14]. Atom centered basis sets can be constructed such that the computational cost scales linearly with the system size [93, 94, 23]. This is a distinct advantage for vdW systems which are often large in size and contain a significant amount of vacuum. What we shall explore here is how the atom centred basis set and changes to such sets affect the accuracy of the vdW-DF binding energies. To begin we shall briefly compare these two different systems for basis sets in the following section.

5.1.1 Plane wave and atom centered basis sets.

Plane wave basis set

As we have already discussed, the KS DFT method maps the many-bodied Schrödinger equation for N interacting particles onto N one-body equations describing a system of non-interacting particles. The non-interacting particles are under the influence of an effective potential V_{eff} such that the resulting ground state density is identical to

that of the interacting system. This system of equations can be defined as:

$$\hat{h}^{KS}\psi_i(\mathbf{r}) = \left[-\frac{1}{2}\nabla^2 + V_{eff}[n](\mathbf{r})\right]\psi_i(\mathbf{r}) = \varepsilon_i\psi_i(\mathbf{r}), \tag{5.1.1}$$

$$n(\mathbf{r}) = 2\sum_i f_i|\psi_i(\mathbf{r})|^2, \tag{5.1.2}$$

where $\hat{h}^{KS}$ is the Kohn-Sham effective Hamiltonian and i is the band index of the Block eigenstate ψ_i, with eigenvalue ε_i and occupancy f_i.* These two equations are coupled through the density dependence of the effective potential, meaning they must be solved self-consistently.

To do this we expand the eigenstates, ψ_i, in a series of basis functions,

$$\psi_i(\mathbf{r}) = \sum_\alpha c_{i\alpha}\chi_\alpha(\mathbf{r}), \tag{5.1.3}$$

where $\chi_\alpha(\mathbf{r})$ are the basis functions and $c_{i\alpha}$ are the expansion coefficients. Here we expand the basis functions, $\chi_\alpha(\mathbf{r})$, for a single Γ-point calculation using plane-waves, $e^{i\mathbf{G}\cdot\mathbf{r}}$,

$$\chi_\alpha(\mathbf{r}) = \frac{1}{\sqrt{\Omega}}\sum_{\mathbf{G}}^{\mathbf{G}_{max}} c_i(\mathbf{G})e^{i\mathbf{G}\cdot\mathbf{r}}. \tag{5.1.4}$$

Where Ω is the volume of the unit cell and $\mathbf{G}$ is a reciprocal space lattice vector. The accuracy of this expansion is determined by the number of plane waves used and to each plane wave there is an associated kinetic energy. By defining a maximum kinetic energy, such that $E_{cutoff} = \frac{1}{2}G_{max}^2$, the maximum number of plane waves used in the expansion can be fixed.

One of the disadvantages of using a plane wave basis is that a large number of

*The factor of 2 in the density accounts for the spin degeneracy as here we are assuming a spin-unpolarised system. Additionally we also consider Γ-point sampling.

basis functions are required to obtain accurate results. As the eigenstates are both delocalised and mutually orthogonal, such that $\langle\psi_i|\psi_j\rangle = \delta_{ij}$, solving the system of equations proceeds like $\mathcal{O}(N^3)$ [18, 14, 92], where N is the number of plane waves. Because of this the calculations can be very computationally expensive for large numbers of plane waves.

Atom centered basis set

In order to achieve a linear-scaling method it is necessary to exploit the "nearsightedness" of quantum many-particle systems [95, 92]. This is the concept that the density is relatively insensitive to distant changes in the external potential [96]. We can take advantage of this by restricting particles to only local interactions. In doing so we reduce the computational cost of the calculation but also reduce its accuracy [97, 94]. Consequently this approximation must be controlled carefully to ensure an acceptable error.

In practice this feature is exploited by re-writing the KS system of equations as a matrix equation. This is then solved using efficient linear algebra algorithms which rely on the sparsity of the matrices. This sparsity of the matrices is a direct result of the expanding the KS orbitals in a set of strictly localised non-orthogonal basis functions, $\phi_\alpha(\mathbf{r})$.

$$\psi_i(\mathbf{r}) = \sum_\alpha c_{i\alpha}\phi_\alpha(\mathbf{r}). \tag{5.1.5}$$

Again here $c_{i\alpha}$ are the expansion coefficients. The resulting matrix equation is:

$$\hat{H}^{KS}\hat{C} = \hat{S}\hat{C}\hat{\varepsilon} \tag{5.1.6}$$

where $\hat{H}^{KS}$ and $\hat{S}$ are the KS and overlap matrices. These are defined as integrals

over the entire space,

$$H^{KS}_{\alpha\beta} = \int \phi_\alpha(\mathbf{r})\hat{h}^{KS}\phi_\beta(\mathbf{r})d\mathbf{r} \tag{5.1.7}$$

$$S_{\alpha\beta} = \int \phi_\alpha(\mathbf{r})\phi_\beta(\mathbf{r})d\mathbf{r}. \tag{5.1.8}$$

Here we use the vector expression of the expansion coefficients, $\hat{C}$. Again the effective potential, contained withing the KS matrix, depends on the density. Here the density is defined as:

$$\rho(\mathbf{r}) = \sum_{i\alpha\beta} c_{i\alpha}c_{i\beta}\phi_\alpha(\mathbf{r})\phi_\beta(\mathbf{r}). \tag{5.1.9}$$

5.1.2 Construction of the Siesta basis set.

In this work we will be using the Siesta [3] DFT code as an example of an atom centered basis set. The Siesta basis set has two significant features,

1. User controlled localisation,

2. User controlled size.

These features mean it is possible to have some control over both the accuracy and the cost of calculations. To do this Siesta utilises numerical atomic orbitals, NAOs. The NAO for atom I, located at $\mathbf{R}_I$ with quantum numbers nlm is given by:

$$\phi_{Ilmn}(\mathbf{r}) = R_{Iln}(r_I)Y_{lm}\left(\frac{\mathbf{r}_I}{|\mathbf{r}_I|}\right), \tag{5.1.10}$$

with $\mathbf{r}_I = \mathbf{r} - \mathbf{R}_I$ and Y_{lm} being the spherical harmonics. The radial part of the orbital centered on atom I, with quantum numbers n and l is given by the function $R_{Iln}(r)$. This definition allows for multiple orbitals with the same angular dependence

but with differing radial dependences, what is conventionally known as a 'multiple-ζ' basis. Increasing the number of ζs our NAO increases the radial flexability of basis, allowing it to better represent the molecular orbitals across a range of chemical environments. For the minimal basis, or single-ζ basis, the radial functions are obtained from the eigenfunctions of the isolated atom contained within a spherical box. These are solutions to the differential equation:

$$\left(-\frac{1}{2r}\frac{d^2}{dr^2}r + \frac{l(l+1)}{2r^2} + V_l(r)\right)\phi_l(r) = (\varepsilon_l + \delta\varepsilon_l)\phi_l(r). \tag{5.1.11}$$

The shift in the energy, $\delta\varepsilon_l$, is the result of forcing the confinement so the first node of the solution occurs at r_c. The length of the basis function is determined by the cutoff length, r_c, after which we force the function to zero. In practice the user selects the energy shift and Siesta applies this to all atomic species resulting in a range of r_cs. Tuning this variable modifies the degree of localisation in the calculation, and hence the computational cost.

To generate the additional radial functions for the multiple-ζ basis, Siesta adopts a modified scheme from the quantum chemistry community, the 'split-valence' method [94]. This works by defining the second-ζ, $\phi_l^{2\zeta}$, as the first-ζ, $\phi_l^{1\zeta}$, with some of its longer range terms removed. To realise this the long range part of the first-ζ is described using the expression,

$$\xi_l(r) = \begin{cases} r^l(a_l - b_l r^2) & \text{if } r < r_l^s \\ \phi_l^{1\zeta}(r) & \text{if } r \geq r_l^s \end{cases} \tag{5.1.12}$$

where a_l and b_l are constants to ensure continuity of value and slope at r_l^s. The 'split-radius' r_l^s is chosen so that a fraction* of the first-*zeta* norm occurs within $r > r_l^s$.

*Typically this value is ~ 0.15.

The second-ζ is then defined as:

$$\phi_l^{2\zeta}(r) = \phi_l^{1\zeta}(r) - \xi_l(r). \tag{5.1.13}$$

Iterative applications of this method allows for the generation of an increasing number of orbitals for the basis.

Combining this method with the generation of orbitals with higher angular momenta, also know as polarised orbitals, results in a basis set with both radial and angular flexibility. Increasing both the radial and angular flexibility of a basis increases the transferability of the basis across a wide range of chemical environments.

In this work we shall examine how changes to the atom centered basis can affect the accuracy of binding energy results when using the vdW-DF density functional. This is not a trivial or insignificant problem. As we have highlighted van der Waals forces are the result of long range correlations. The issue is whether the steps taken in the Siesta code to achieve linear scaling adversely affect the accuracy of the dispersion interactions. In the next section we shall discuss how we shall quantify and measure how changes in the basis set affect vdW interactions.

5.2 Quantifying the accuracy of vdW interactions

In order to determine how changes to the Siesta basis set affect the accuracy of vdW interactions, we have selected two system attributes which we calculate in both Siesta [3] and Quantum Espresso (QE) [87], a plane wave code. It is straight forward to obtain a converged plane wave basis as there is only a single parameter to vary, the kinetic energy cutoff for the plane waves, and they do not suffer from issues regarding localisation, as Siesta does. This means we can easily compare the results from our Siesta calculations to QE and isolate the effects of modifying the basis set.

5. AN EXAMINATION OF THE ACCURACY OF VDW-DF BINDING ENERGIES, AS CALCULATED WITHIN AN ATOM CENTERED BASIS SET, OVER THE S22 MOLECULAR DATABASE.

Firstly we calculate the binding energy of compounds from the S22 molecular database [98]. This is a set of 22 complexes which can be divided into three categories: those which are bound by hydrogen bonds, those bound by dispersion bonds and those in which covalent and dispersion bonds are of equal importance, otherwise known as the mixed category. The database contains the binding energies and optimised structures for the complexes, obtained from highly accurate Moller-Plesset [10] and coupled cluster calculations [99]. Using the optimised structures we shall compare calculations of binding energies, done in Siesta, with those done in the plane wave code, Quantum Espresso. We define the binding energy of a complex comprising of two monomers as:

$$E_{\text{bind}} = E_{\text{complex}} - E_{\text{monomer1}} - E_{\text{monomer2}}, \tag{5.2.1}$$

where E_{bind} is the binding energy, E_{complex} is the total energy of the complex and E_{monomeri} is the total energy of the i^{th} monomer in the complex.

Secondly we shall compare the densities obtained from both Siesta and QE calculations, for the same selection of compounds as the binding energy. There are two important reasons for this:

1. As stated in our definition of DFT, the ground state electronic density contains all the information for the ground state of the system. Consequently if the two densities, from the QE and Siesta calculations, are identical we know that both codes will return the same results. A similar argument can be made regarding the vdw-DF and dispersion forces: if our two densities match then the dispersion interactions will also be identical regardless of any "nearsightedness" in the Siesta basis set.

2. Atom centered basis sets have a significant problem calculating binding ener-

gies. This is known as the basis set superposition error, BSSE [100]. Every basis set has an associated error, this error is the difference between the chosen basis and the infinite basis set. In practice careful selection of sufficiently large sets results in acceptably small errors. However this issue manifests itself in the calculation of intermolecular binding energies using atom centered basis sets. The issue is that the complex and the monomers will be calculated in basis sets of significantly differing sizes. If the number of atoms in the two monomers are N_a and N_b, the complex basis set will be $\mathcal{O}(N_a + N_b)$ while those of the monomers would be $\mathcal{O}(N_a)$ and $\mathcal{O}(N_b)$. This is an important issue for vdW complexes as their binding energies tend to be $\mathcal{O}(100)meV$, with typical BSSE values being a significant appreciable magnitude in comparison with this. While there are methods to correct for this [101], they are typically restricted to static calculations meaning we cannot calculate the BSSE corrected binding energy including the internal relaxation of the atomic positions for the monomers. Figure 5.1 shows the conventional counterpoise correction method to correct for the BSSE. In this method "ghost atoms", that is the basis functions associated with a particular atom but without any electrons or nuclei, are added to the monomer calculations to ensure a consistent basis set size across all the calculations.

To compare the densities we define the normalised density difference*:

$$dd(\rho_{Siesta}(\mathbf{r}), \rho_{QE}(\mathbf{r})) = 1 - \frac{\int |\rho_{Siesta}(\mathbf{r}) - \rho_{QE}(\mathbf{r})| d\mathbf{r}}{\int \rho_{QE}(\mathbf{r}) d\mathbf{r}}, \tag{5.2.2}$$

where $\rho_{QE}(\mathbf{r})$ and $\rho_{Siesta}(\mathbf{r})$ are the densities resulting from the QE and Siesta calculations. The normalised density difference is a number lying between 0 and 1, the closer it is towards 1 the more similar the two densities are.

*We will also refer to this as the density difference

5.3 Computational Methods

We performed DFT calculations using both QE [87] and Siesta [3] using Troullier-Martins norm conserving pseudopotentials [91]. The pseudopotentials were generated in our cross code pseudopotential generator, a modified version of the ld1.x pseudopotential generator* capable of outputting the same potential in both Siesta and QE formats. In doing this we remove any ambiguity that differing pseudopotentials might produce differing electronic densities. Any remaining differences between the densities should be the result of differing basis sets. †

The QE calculations were performed in a 60 Bohr cubic cell with a 60 Rydberg plane wave cutoff. The Siesta calculations were also performed in a 60 Bohr cubic cell, with a mesh cut-off of 500 Rydbergs and an energy shift of $1meV$. Figure 5.2 shows that for our isolated complexes, energy shifts of $1meV$ or less lead to convergence errors of less than $1meV$ in the binding energy. All our calculations are done with a single k point at the Γ point ($k = 0$).

The generated pseudopotentials were tested in QE, using the details below, by calculating the binding energy of the water and formic acid dimers with the PBE [27] XC functional. The binding energy of the water dimer was found to be 218meV, this compares well with the all electron calculation of 219meV of Lee et al [56]. The formic acid dimer binding energy was calculated to be 797meV compared to the all electron value of 790meV, also from Lee et al [56].

In addition to using Siesta to generate NAOs for our basis sets using our fixed energy-shift of 1meV, we also created basis sets with each cutoff individually optimised. More information about this as well as our optimised basis sets are given in the appendix.

*This code is part of the Quantum Espresso package [87]

†This assumes that the total energy functionals as implemented in both codes can correctly evaluate the total energy without introducing an additional errors.

5.4 Results

This section is split into two parts. Firstly we will examine the binding energy of a small section of complexes as well as discuss and quantify the origin of errors in our atom centered basis calculations. From this we will identify basis set qualities which minimise binding energy errors. In the second part we will compare these qualities across the entire S22 database to extract clear ideas about how the vdW-DF, as calculated within an atom centered basis, performs.

5.4.1 Density based analysis of vdW-DF errors.

The four systems we shall examine in detail are the water, formic acid, and methane dimers as well as the benzene methane complex. They form an interesting mix of hydrogen bonded and dispersion bound complexes. For each complex we calculate the binding energy, as calculated with Siesta, for a range of basis sets both with and without counterpoise corrections. Additionally for each calculation we extracted the charge density of the monomers as well as the complexes. These binding energies and densities are then compared to our QE results to identify and quantify the following errors in the binding energy.

1. **Actual error**: We define this as the difference in the binding energies between our atom centered basis calculations and plane wave basis calculations. This is the total error resulting from the use of an atom centered basis instead of a converged set of plane waves as the other parameters are identical between the two calculations. This error is the result of an aggregate of the other errors.

$$\mathrm{AE}(\text{test basis}) = |E_{\mathrm{bind}}(\text{test basis}) - E_{\mathrm{bind}}(\text{converged plane wave})| \quad (5.4.1)$$

Where AE is the actual error, E_{bind}(test basis) is the binding energy calculated

using the basis under investigation and E_{bind}(converged plane wave) the binding energy calculated in a converged plane wave basis.

2. **Insufficient basis error**: This is the error arising from using a basis that is less than that of the converged basis. For a plane wave basis this is equivalent to the actual error. For non-plane wave basis sets we construct an analogous plane wave basis whose density difference to the converged plane wave basis is identical to that of the basis in question, the test basis. We define η(test basis) as a function which returns the analogous plane wave basis with the same density difference as the test basis. The insufficient basis error is then defined as,

$$\text{IBE(test basis)} = |E_{\text{bind}}(\eta(\text{test basis})) - E_{\text{bind}}(\text{converged plane wave basis})| \tag{5.4.2}$$

Where IBE is the insufficient basis error, E_{bind}(test basis) is the binding energy calculated using the basis under investigation and E_{bind}(converged plane wave) the binding energy calculated in a converged plane wave basis. In this work we approximate the action of η by pre-calculating the density difference at several different plane wave basis sizes and then selecting the basis whose density difference is closest to that of the test basis. The binding energy is then calculated using the analogous plane wave basis.

3. **Basis set superposition error**: This is the error from mismatched monomer and complex basis sets. Here we *estimate* the BSSE through the difference between the counterpoise corrected and uncorrected binding energies. It is important to note that the addition of ghost atoms to the monomer basis does not give an equivalent basis to that of the complex. Ghost atoms are empty orbitals and as such the monomer electrons will fill them easier than real atomic

orbitals.

$$\text{BSSE(test basis)} = |E_{\text{bind}}(\text{test basis}) - E_{\text{bind}}(\text{test basis + ghost atoms})| \tag{5.4.3}$$

Where BSSE is the basis set superposition error, E_{bind}(test basis) is the binding energy calculated using the basis under investigation and E_{bind}(test basis + ghost atoms) the binding energy calculated using the test basis supplemented with ghost atoms for counterpoise correction.

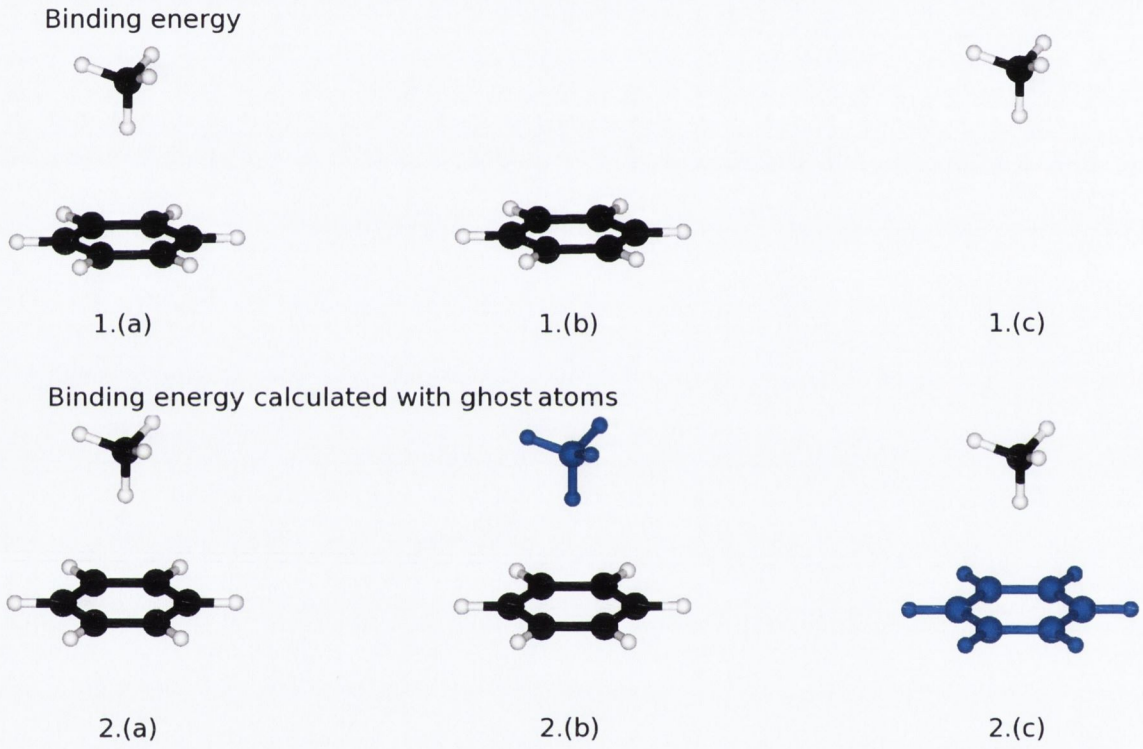


Figure 5.1: Pictorial explanation of counterpoise correction. - Figures 1.(a-c) show the calculations required for a standard binding energy calculation of the benzene methane complex. The binding energy, as defined by equation (5.2.1), is the total energy of complex $1.(a) - 1.(b) - 1.(c)$. Figures 2.(a-c) show the positions of the ghost atoms in blue. A binding energy calculation with counter poise corrections can be achieved with $2.(a) - 2.(b) - 2.(c)$

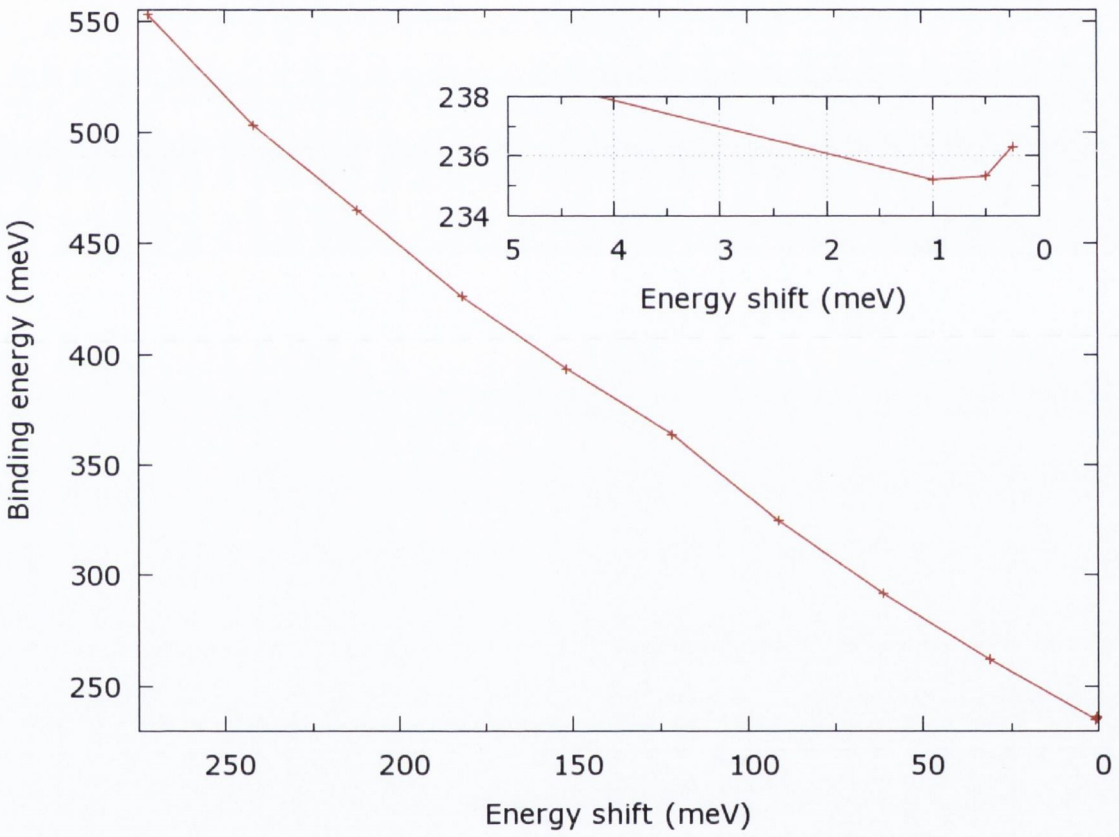


Figure 5.2: Convergence of the binding energy with energy shift - Convergence of the water dimer binding energy with increasing values of the basis energy shift, from equation 5.1.11. The insert shows the values less then 5 meV. Note that the binding energies corresponding to the 1 meV, 0.5 meV and 0.25 meV energy shifts all lie within 1 meV of each other. Calculations were done in the Siesta [3] DFT code using the vdW-DF [49] XC.

Water dimer

The binding energy of the water dimer, as calculated in both Siesta and QE, is shown in Figure 5.3. The figure shows the binding energy for the five Siesta basis sets constructed both with and without ghost atoms. The QE binding energy is superimposed on top of the plot. There are several points of interested in this plot:

1. The Siesta results can be bracketed into two groups, within which the binding energies vary non-monotonically; those with and without ghost atoms in the monomer basis set.

2. The binding energies from the ghost atom group fluctuate about the QE binding energy result, while the non ghost atom group fluctuates about some larger binding energy value. This is an expected result however and is a consequence of the previously mentioned basis set superposition error. To reiterate, we see an increase in the binding energy due to the disparity in the basis sets of the monomer and dimer calculations. The increased basis set of the dimer significantly lowers the total energy; it is this lowering which we then see as an increase in the binding energy beyond that of the counterpoise corrected results.

In order to estimate the error in the binding energy due to the insufficient basis error we must first quantify how similar our Siesta densities are to those of the converged QE calculations. To do this we calculate the normalised density difference, equation (5.2.2). Figure 5.5 shows the results of plotting this for the water molecule and water dimer. The plot compares the densities obtained from using various Siesta basis sets with the density obtained from a fully converged QE calculation. If two densities are identical the normalised density difference will be 1, the closer two densities are to 1 the more similar they are. It can be seen in the figure that the double zeta + polarised, triple zeta + polarised and optimised basis basis sets are closest to

1 while the double zeta and triple zeta basis sets are furthest. In comparing this plot to that of Figure 5.3 we can also see that the basis sets with density differences closest to 1 also returned binding energies closest to that of the QE value.

The spread of values between the monomer, complex and monomer with ghost atoms for a particular basis set indicates the degree of BSSE included for that particular basis set. For example, in the triple zeta basis results we see a large separation between the complex and monomer values with a smaller separation between the complex and monomer including the ghost atoms. This relationship is repeated in Figure 5.3, again for the triple zeta results we see a large over binding and a reduction in this as we include ghost atoms in the basis.

To link our normalised density difference values to estimates of the insufficient basis error we first need to calculate how the changes in the density results in errors in the binding energy. We do this in Figure 5.4. Here we compare the normalised density difference for densities calculated in QE using different plane wave cutoff values to the density from the converged QE calculation*. Additionally we have plotted the binding energy as calculated at each of the cutoff values. From this plot we construct the reference, Table 5.1 for this system. This reference table allows us to correlate density differences from the converged QE density to binding energy errors. As these are the errors in plane wave calculations there is no BSSE and the error comes from insufficient basis size.

In order to calculate the insufficient basis error for our Siesta calculations we apply the results of Table 5.1 to the normalised density differences of our Siesta results, Figure 5.5. First however we must decide which densities we are comparing. Unlike in the QE calculations where both the monomer and complex are calculated using the same sized basis set, and hence have identical density differences, the Siesta

*In Figure 5.4 we use the density generated at the 65 Ry kinetic energy cutoff as the reference density, against which we compare the other densities.

$E_{cut}(Ry)$	normalised density difference	Binding energy error (meV)
20.000000	0.846082938092	152.591
25.000000	0.886367033405	67.518
30.000000	0.91605042074	53.893
35.000000	0.938444988106	37.875
40.000000	0.955062478072	9.065
45.000000	0.968015474536	9.165
50.000000	0.978537333832	5.146
55.000000	0.987248096636	0.211
60.000000	0.994429601729	0.232

Table 5.1: Normalised density difference and associated binding energy error for the water dimer - A reference table of the normalised density differences for the water dimer along with the plane wave kinetic energy cutoff used to generate each density and the resulting error in the binding energy. The values for this table are plotted in Figure 5.4. Note for this system, values of 40 Ry or larger are necessary to give errors of less than 10 meV in the binding energy. Equivalently normalised density differences of 0.955 or greater are necessary to ensure errors of no more than 10 meV in the binding energy.

complex and monomer basis differ. If there was no difference between the basis sets there would be no BSSE in the binding energy and the only difference in the binding energy from the QE result would be due to inadequate basis set size. If we adopt this idea and using Table 5.1 with the normalised density difference from the smallest basis set, that of the uncorrected monomer, we obtain estimates for the errors in the Siesta basis sets due to the size of the basis set *alone*. That is errors untainted by the BSSE.

In table 5.2 we estimate the Siesta insufficient basis error using the normalised density differences from Figure 5.5 and reference table 5.1. The monomer density differences are matched to the nearest values in the reference table. Additionally we also include the actual errors and an estimate of the BSSE from Figure 5.6.

Table 5.2 summaries the results for the water dimer. We draw three important results from this:

Siesta basis	density difference	insufficient basis (meV)	BSSE (meV)	actual uncorrected (meV)	actual corrected (meV)
double zeta	0.933	37.88	55.01	108.89	53.88
double zeta + polarised	0.972	9.16	103.40	51.33	-52.06
triple zeta	0.938	37.88	121.06	168.05	46.99
triple zeta + polarised	0.974	5.15	68.91	43.60	-25.31
optimised	0.968	9.16	13.18	46.38	33.20

Table 5.2: Estimated and actual Siesta binding energy errors for the water dimer - The errors for the water dimer are given in meV in the different columns. The density difference is the normalised density difference between the non counterpoise corrected monomer and the converged plane wave density. This is used to estimate the insufficient basis error, error in the binding energy due to the basis set not being the converged basis. We use the uncorrected monomer as this will give the largest estimate for this error. The BSSE values are taken from Figure 5.6. The actual errors are the differences between the Siesta calculated binding energies and the converged plane wave result. Here we give errors from both the non counterpoised corrected and corrected basis set calculations.

1. The error from not using the converged basis set, the basis set insufficiency error, is small for all our calculations. It is always far less than both the actual errors as well as the BSSE.

2. Our estimated BSSE values can be both larger than as well as smaller than the actual error. When the BSSE is larger than the actual error the addition of ghost atoms to the basis causes the complex to switch from over binding to under binding. This result is in line with other works which showed that the addition of ghost atoms to a basis does not systematically lead to improved binding energy accuracies [102].

3. While the BSSE for the optimised basis is the lowest, both the corrected and uncorrected values of the triple zeta + polarised binding energies are less than those of the optimised.

For the remaining compounds we shall show the binding energy plot, normalised density difference for the Siesta densities plot, the estimate of the BSSE plot, our reference table of the QE density difference and corresponding binding energy error, and our results table showing our estimates for the BSSE, the insufficient basis error as well as both the corrected and uncorrected binding energy errors. These results are enough to draw conclusions about the performance of the different basis sets. Our focus is on the accuracy of the actual errors as well the magnitudes of the BSSE and insufficient basis error.

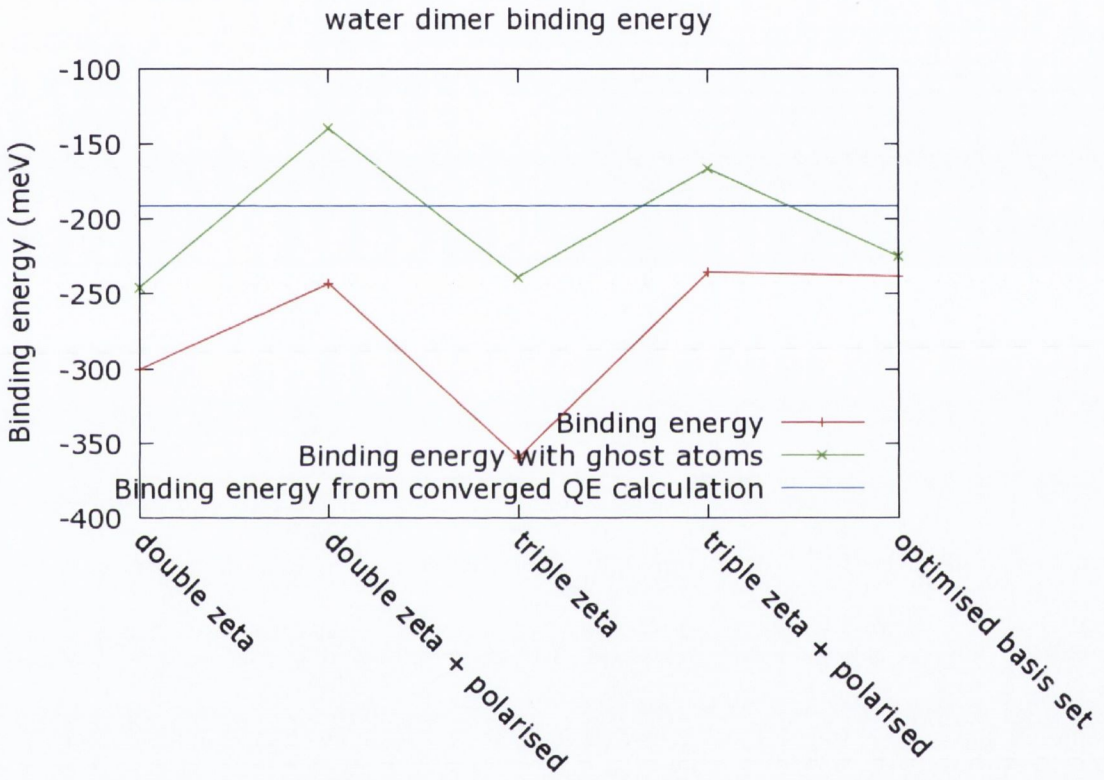


Figure 5.3: Water dimer binding energy - Binding energy calculated for a selection of Siesta basis sets with and without the addition of ghost atoms to the monomer basis calculation. Note how the values from the basis sets including ghost atoms fluctuate about the QE binding energy result while the values from sets without the ghost atoms fluctuate about a much higher value. This is due to the BSSE, the smaller basis set of the monomer restricts the electrons causing an increase in monomer total energy. The result of this is an increase in the binding energy.

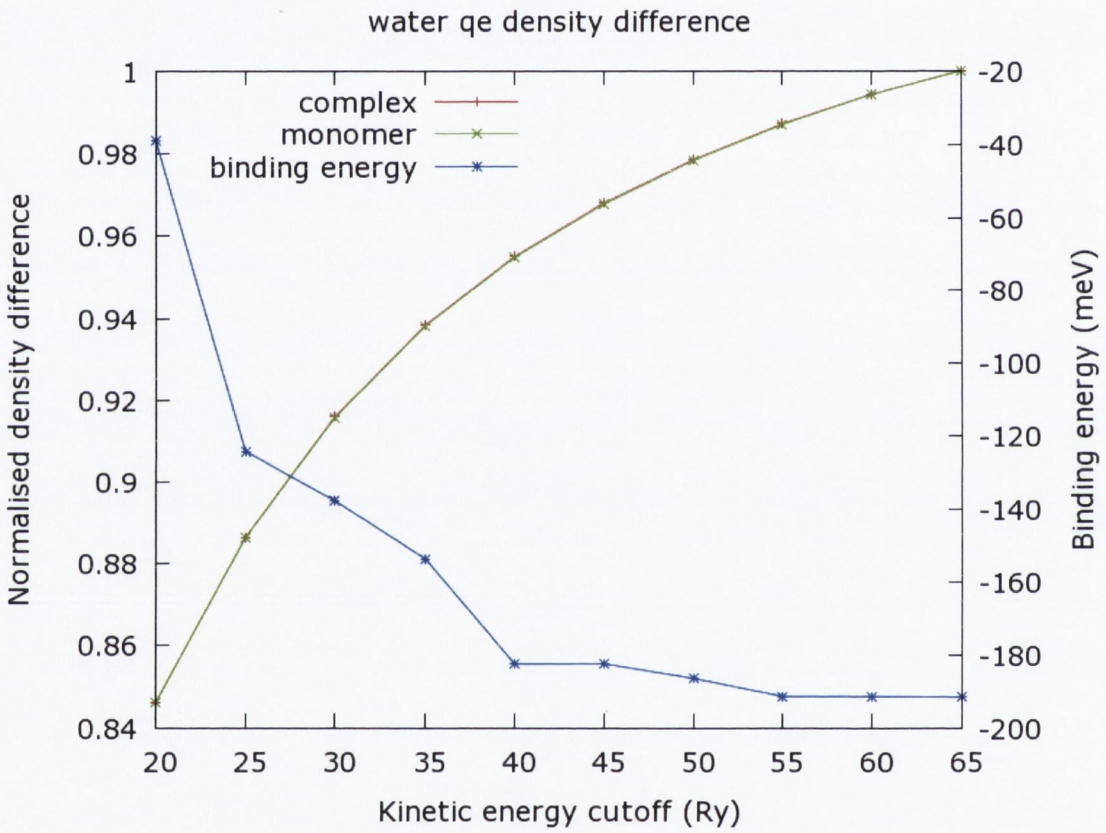


Figure 5.4: Water dimer QE normalised density difference - Normalised density difference plot for QE densities comparing the density at differing plane wave cutoff values to the converged QE density. The normalised density difference is plotted on the left axis while the binding energy is plotted on the right axis. Note how the normalised density difference values for the monomer and complex are equivalent, this is expected as the basis set is identical for the two calculations. The error in the water dimer binding energy equated to the normalised density difference can be seen in Table 5.1.

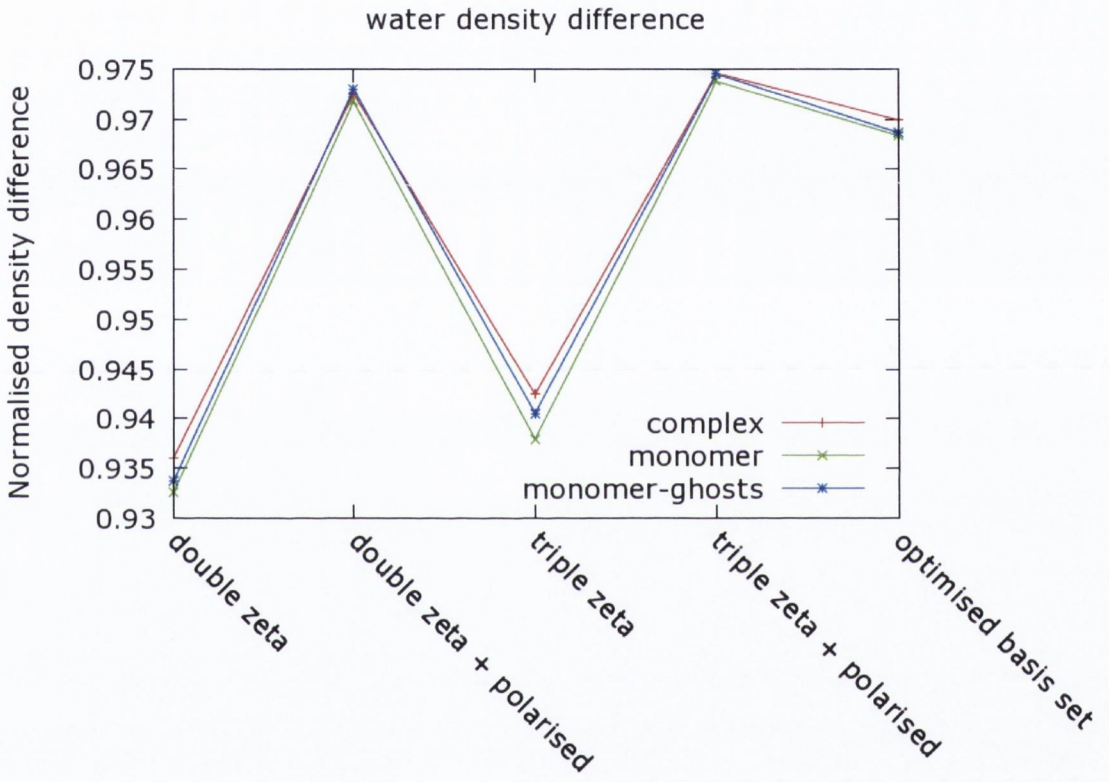


Figure 5.5: Normalised density difference for the water dimer - Plot of the normalised density difference, equation (5.2.2), for the single water molecule, with and without ghost atoms, and the water dimer. The densities from the Siesta basis sets for each molecule is compared to the corresponding density from a converged QE calculation. Note how the double zeta + polarised, triple zeta + polarised and optimised basis results are closest to 1. This indicates that these basis sets result in densities closest to those from the converged QE calculations, as well as binding energies closest to that of QE result.

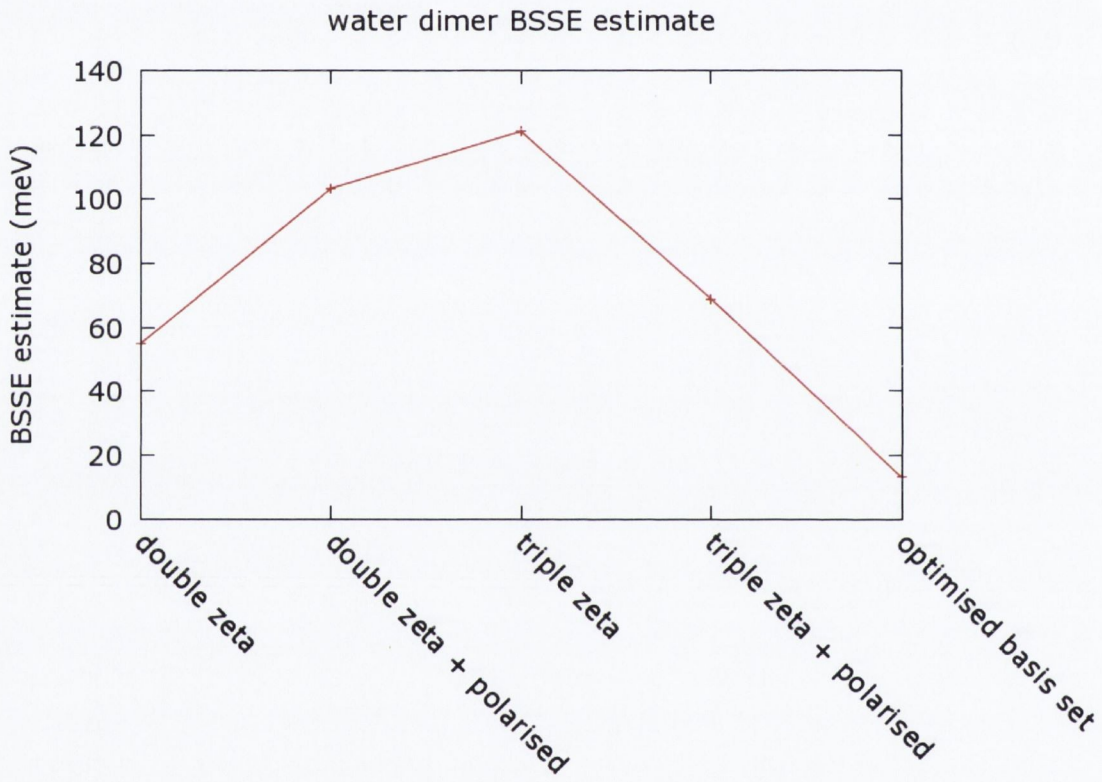


Figure 5.6: Estimate of the BSSE for the water dimer - Using ghost atoms as a counterpoise correction an estimate of the BSSE can be obtained from the difference between the Siesta binding energies calculated with and without correction. Identically in the dimer complex case, this is the difference between the energies of the monomer and the monomer with counterpoise correction. Note here that the energy difference is smallest for the optimised basis set.

Formic Acid dimer

The results of the formic acid dimer are very similar to that of the water dimer although they do confirm and reinforce our previous results, here we shall mention our results succinctly. Figure 5.7 shows the binding energy of the dimer calculated with and without counterpoise corrections. Again the binding energies from the corrected basis sets fluctuate about the QE binding result while the uncorrected results fluctuate about a much higher limit. Again the result from the uncorrected optimised basis set lies quite close to that of the converged QE calculation. As normalised density difference plotted in Figure 5.8 is very similar to that of the water complex, see Figure 5.5, we shall forgo the detailed analysis of the results except to note that it is the same basis sets producing the highest density differences. Additionally we note that the optimised basis set has the highest normalised density difference and the lowest spread in differences,this is confirmed in the plots of the estimated BSSE seen in Figure 5.9.

Table 5.4 shows the actual errors in the dimer binding energies as well as our estimates for the insufficient basis error, using values from table 5.3, as well as the BSSE, from Figure 5.9. From the table we can draw the following results:

1. The insufficient basis error is particularly large for basis sets which do not include polarised orbitals in the basis.

2. The BSSE is fairly consistent, and large, across all the basis sets.

3. For all but the optimised basis, applying the counterpoise correction dramatically decreases the error between the Siesta and QE binding values. In the optimised case the correction acts in the wrong direction causing the complex to become even more under bound.

$E_{cut}(Ry)$	normalised density difference	Binding energy error (meV)
20	0.853	530.14
25	0.894	518.77
30	0.922	227.16
35	0.942	143.51
40	0.957	109.15
45	0.969	34.93
50	0.979	16.30
55	0.988	14.32
60	0.995	5.88

Table 5.3: Normalised density difference and associated binding energy error for the formic acid dimer -A reference table of the normalised density differences for the formic acid dimer along with the plane wave kinetic energy cutoff used to generate each density and the resulting error in the binding energy.

Siesta basis	density difference	insufficient basis (meV)	BSSE (meV)	actual uncorrected (meV)	actual corrected (meV)
double zeta	0.949	143.51	259.37	264.54	5.16
double zeta + polarised	0.974	16.30	225.27	207.74	-17.53
triple zeta	0.953	109.15	253.56	263.39	9.83
triple zeta + polarised	0.976	16.30	121.99	113.53	-8.46
optimised	0.969	34.93	66.29	-34.62	-100.90

Table 5.4: Estimated and actual Siesta binding energy errors for the formic acid dimer - The errors for the formic acid dimer are given in meV in the different columns. The density difference is the normalised density difference between the non counterpoise corrected monomer and the converged plane wave density. This is used to estimate the insufficient basis error, error in the binding energy due to the basis set not being the converged basis. We use the uncorrected monomer as this will give the largest estimate for this error. The BSSE values are taken from Figure 5.9. The actual errors are the differences between the Siesta calculated binding energies and the converged plane wave result. Here we give errors from both the non counterpoised corrected and corrected basis set calculations.

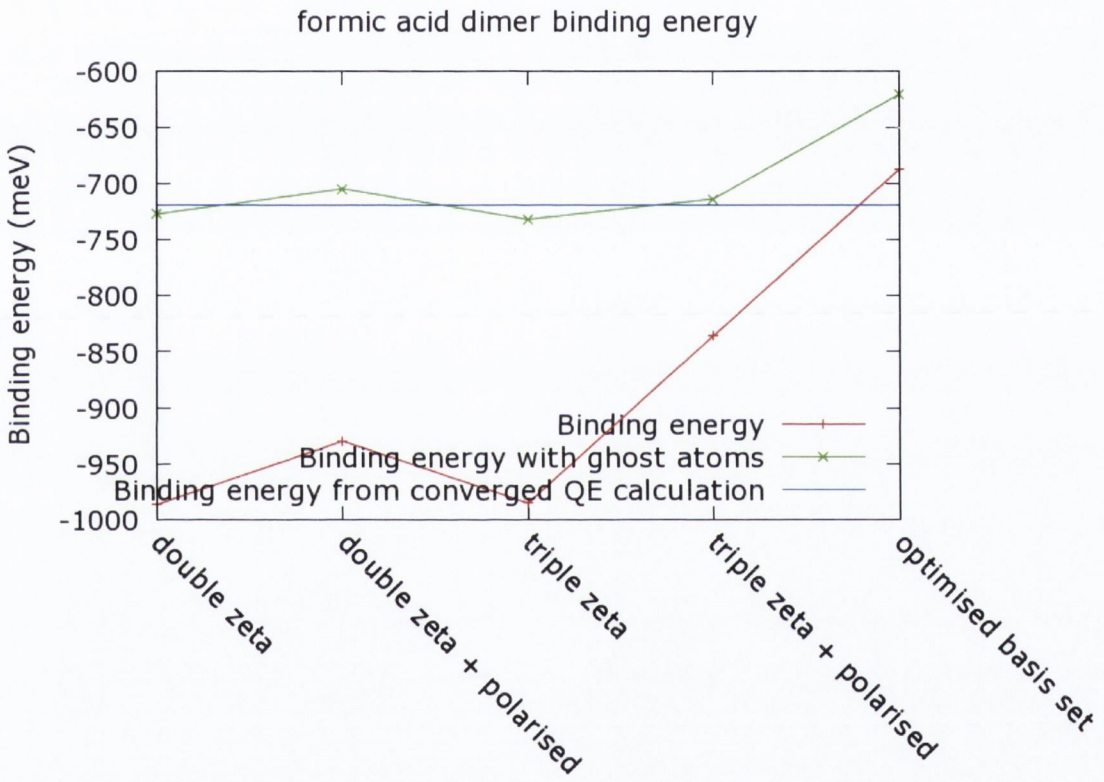


Figure 5.7: Formic acid dimer binding energy - Binding energy calculated for a selection of Siesta basis sets with and without the addition of ghost atoms to the monomer basis calculation. Note how the values from the basis sets including ghost atoms fluctuate about the QE binding energy result while the values from sets without the ghost atoms fluctuate about a much higher value; a result of the BSSE.

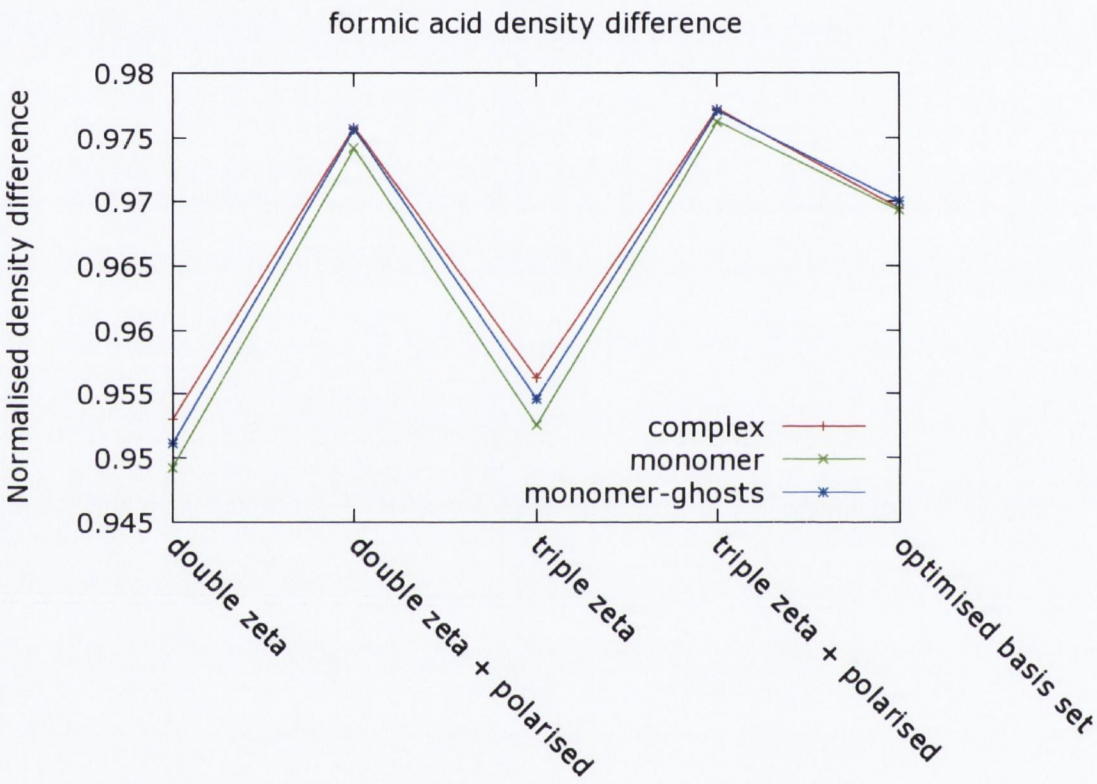


Figure 5.8: Normalised density difference for the formic acid dimer - Plot of the normalised density difference, equation (5.2.2), for the single formic acid molecule, with and without ghost atoms, as well as the dimer. The densities from the Siesta basis sets for each molecule is compared to the corresponding density from a converged QE calculation. Note how the double zeta + polarised, triple zeta + polarised and optimised basis results are closest to 1. This indicates that these basis sets result in densities closest to those from the converged QE calculations.

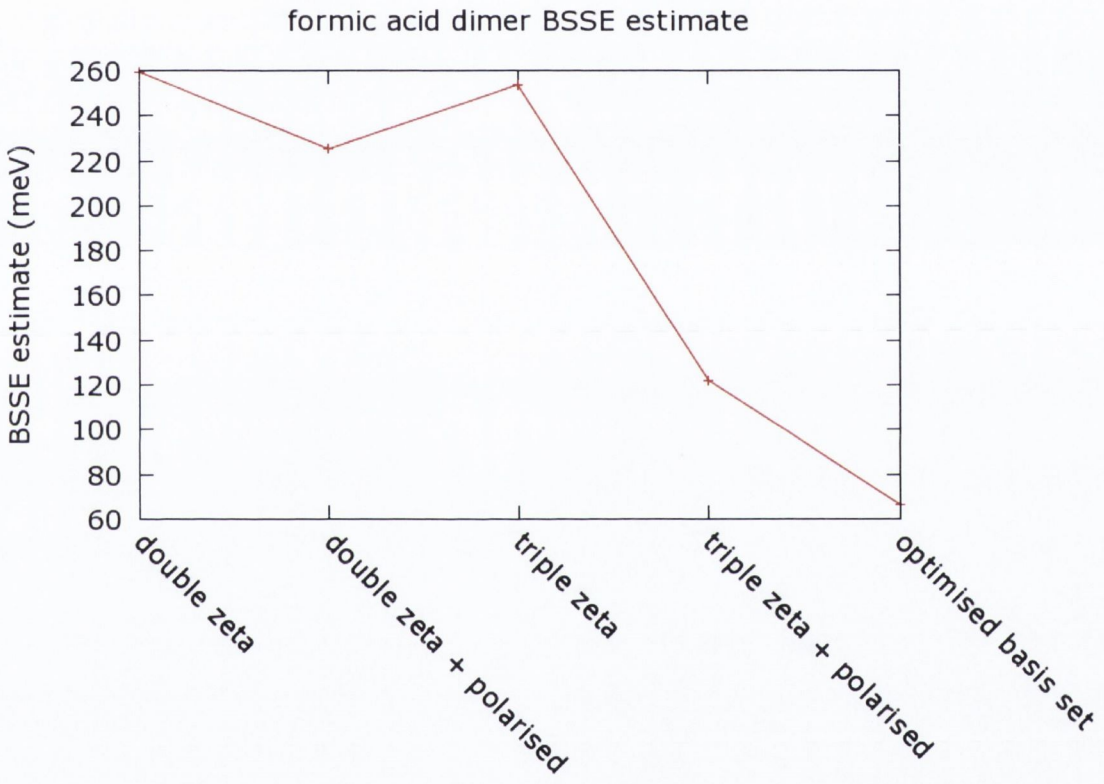


Figure 5.9: Estimate of the BSSE for the formic acid dimer - Using ghost atoms as a counterpoise correction an estimate of the BSSE can be obtained from the difference between the Siesta binding energies calculated with and without correction. Identically in the dimer complex case, this is the difference between the energies of the monomer and the monomer with counterpoise correction. Note here that the energy difference is smallest for the optimised basis set.

Methane dimer

The methane dimer is an interesting and difficult test case. It is purely dispersion bound, unlike the water and formic acid dimers which are hydrogen bound, and its binding energy is very small due to the reduced size of the monomers. It is the reduced size of the monomers which causes atom centered basis sets problems, a particularly small basis set. This is evident in the binding energy results seen in Figure 5.10. A plot of the normalised density difference, Figure 5.11 goes some way to explaining these poor results. The plot shows a large separation between the monomer and complex density differences as well as a similarly large gap between the counterpoise corrected monomer and the complex. This is expected however with such a small basis set, both the monomer and complex are not large enough to describe the system with sufficient accuracy.

Table 5.6 shows the actual errors in the dimer binding energies as well as our estimates for the insufficient basis error, using values from table 5.5, as well as the BSSE, from Figure 5.12. From the table we can draw the following results:

1. The insufficient basis error is surprisingly small and consistent across all the basis sets.

2. Increasing the size of the basis, by increasing the number of zetas and including polarised orbitals, the counterpoise corrected binding energy decreases to a minimum for the triple zeta + polarised basis. The optimised basis can be compared to the double zeta + polarised basis where it seems to increase the uncorrected binding error but decrease the magnitude of the corrected value. Again however the triple zeta + polarised basis gives a lower error than the optimised basis.

$E_{cut}(Ry)$	normalised density difference	Binding energy error (meV)
20	0.942	-1.05
25	0.963	-1.89
30	0.974	-1.88
35	0.981	-1.62
40	0.985	-0.11
45	0.989	-0.35
50	0.992	-0.58
55	0.995	-0.47
60	0.998	-0.18

Table 5.5: Normalised density difference and associated binding energy error for the methane dimer - A reference table of the normalised density differences for the methane dimer along with the plane wave kinetic energy cutoff used to generate each density and the resulting error in the binding energy.

Siesta basis	density difference	insufficient basis (meV)	BSSE (meV)	actual uncorrected (meV)	actual corrected (meV)
double zeta	0.943	-1.05	4.62	16.37	11.75
double zeta + polarised	0.957	-1.89	2.96	13.25	10.29
triple zeta	0.944	-1.05	19.43	24.53	5.10
triple zeta + polarised	0.958	-1.89	12.06	14.70	2.64
optimised	0.964	-1.89	23.13	16.74	-6.39

Table 5.6: Estimated and actual Siesta binding energy errors for the methane dimer - The errors for the methane dimer are given in meV in the different columns. The density difference is the normalised density difference between the non counterpoise corrected monomer and the converged plane wave density. This is used to estimate the insufficient basis error, error in the binding energy due to the basis set not being the converged basis. We use the uncorrected monomer as this will give the largest estimate for this error. The BSSE values are taken from Figure 5.12. The actual errors are the differences between the Siesta calculated binding energies and the converged plane wave result. Here we give errors from both the non counterpoised corrected and corrected basis set calculations.

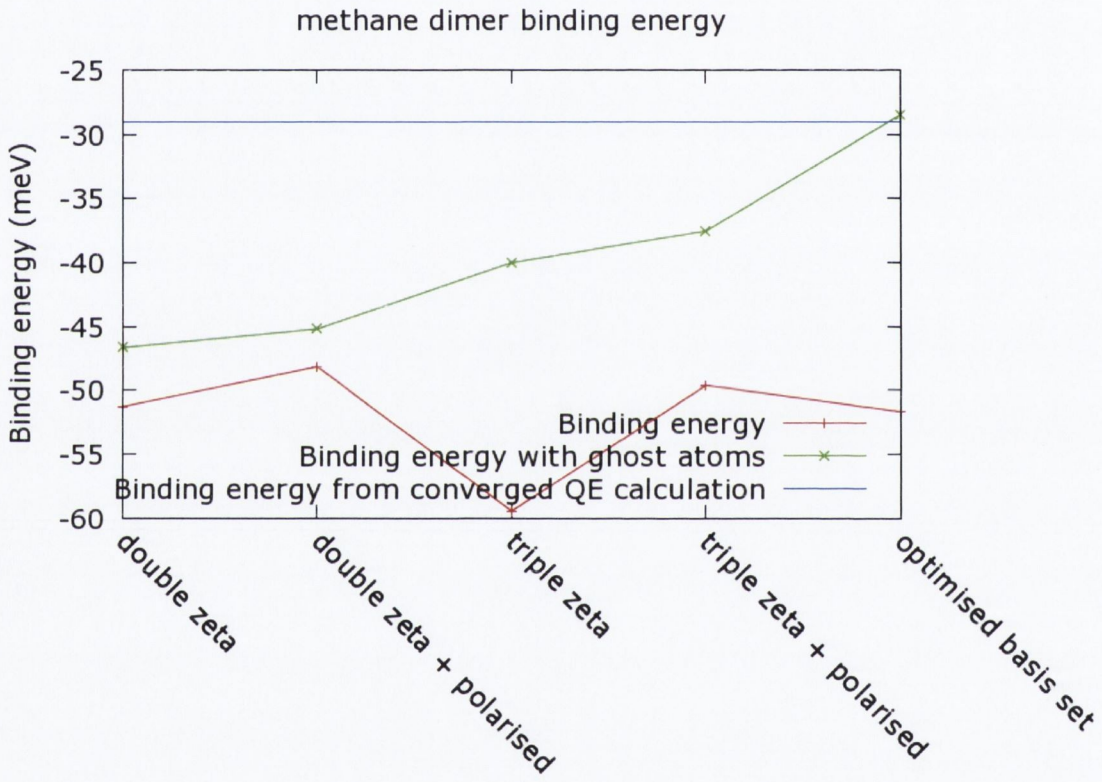


Figure 5.10: Methane dimer binding energy - Binding energy calculated for a selection of Siesta basis sets with and without the addition of ghost atoms to the monomer basis calculation.

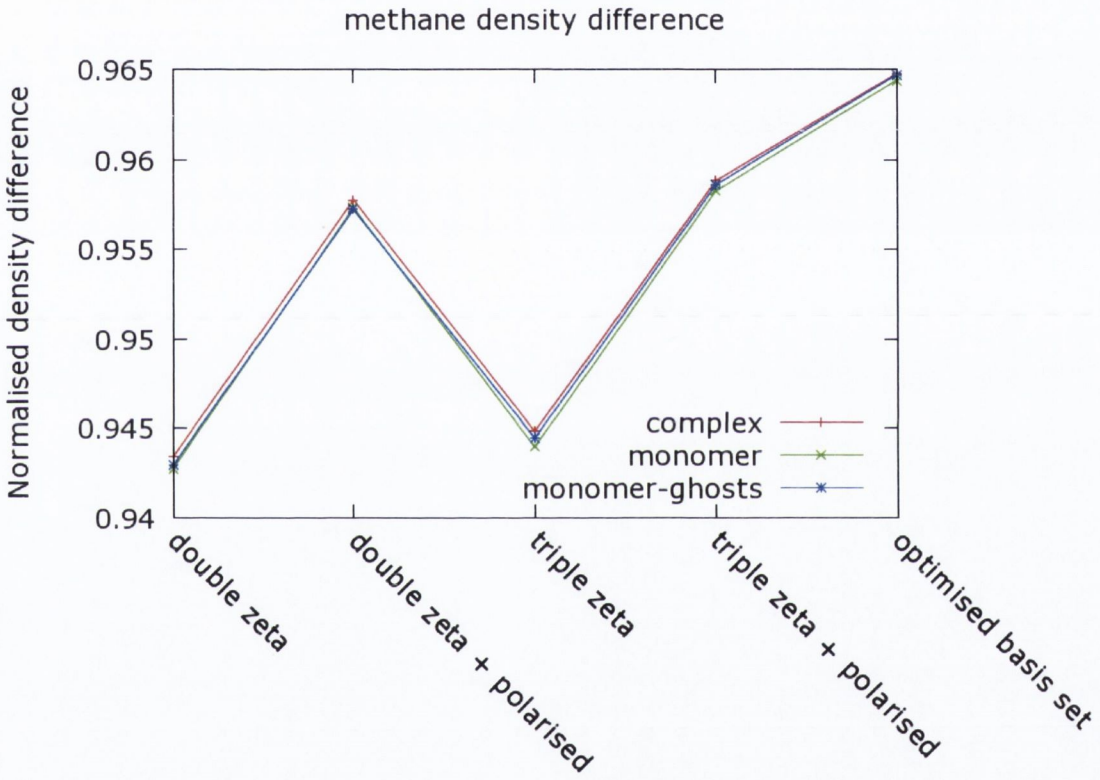


Figure 5.11: Normalised density difference for the methane dimer - Plot of the normalised density difference, equation (5.2.2), for the single methane molecule, with and without ghost atoms, as well as the dimer. The densities from the Siesta basis sets for each molecule is compared to the corresponding density from a converged QE calculation.

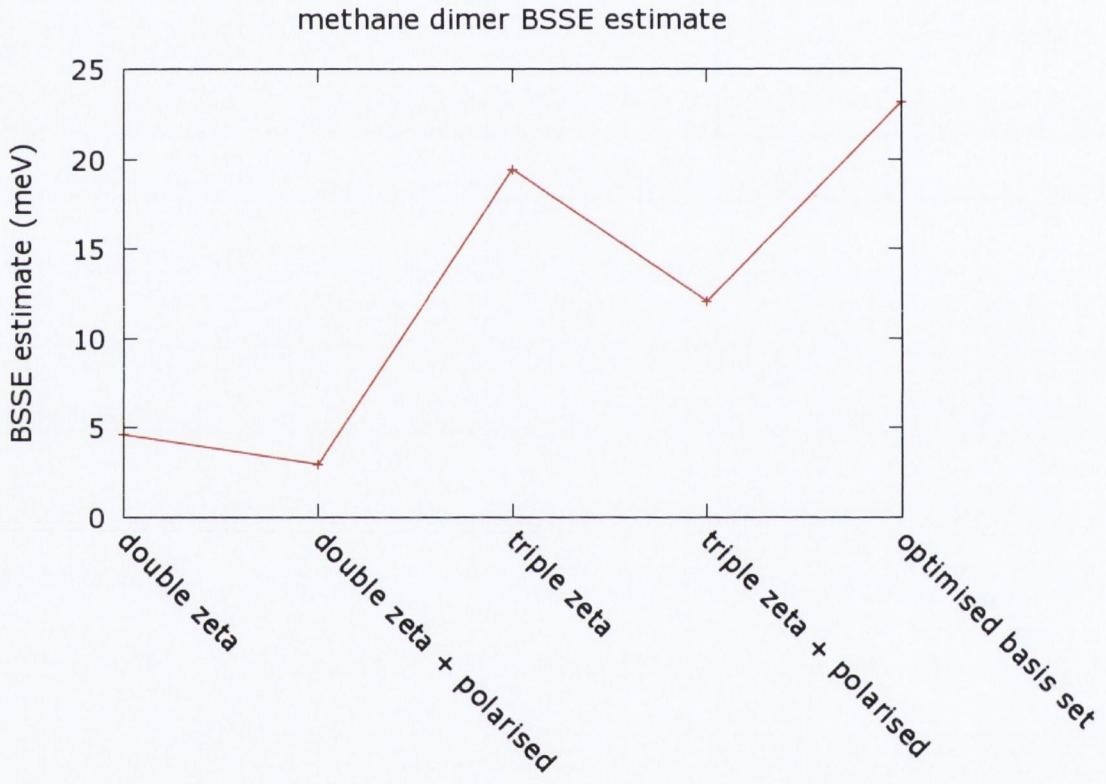


Figure 5.12: Estimate of the BSSE for the methane dimer - Using ghost atoms as a counterpoise correction an estimate of the BSSE can be obtained from the difference between the Siesta binding energies calculated with and without correction.

$E_{cut}(Ry)$	normalised density difference	Binding energy error (meV)
20	0.934	-22.55
25	0.957	-23.63
30	0.969	-35.45

Table 5.7: Normalised density difference and associated binding energy error of the benzene methane complex - A reference table for the normalised density differences for the benzene methane complex along with the plane wave kinetic energy cutoff used to generate each density and the resulting error in the binding energy.

Benzene methane complex

Table 5.8 shows the actual errors in the binding energies of the benzene methane complex as well as our estimates for the insufficient basis error, using values from table 5.7, as well as the BSSE, from Figure 5.15. From the table we can draw the following results:

1. The insufficient basis error is very consistent across all the Siesta generated basis sets*, varying by no more than 2 meV.

2. Although the BSSE universally over corrects for all the basis sets, the corrected binding errors appear to decrease for increasing basis quality.

*These are basis sets generated entirely by Siesta with a minimal external input. This includes all the basis sets used here *except* for the optimised basis.

Siesta basis	density difference	insufficient basis (meV)	BSSE (meV)	actual uncorrected (meV)	actual corrected (meV)
double zeta	0.943	-22.55	19.57	9.51	-10.06
double zeta + polarised	0.957	-23.63	25.40	18.93	-6.47
triple zeta	0.944	-22.55	44.55	37.15	-7.40
triple zeta + polarised	0.958	-23.63	19.78	15.03	-4.74
optimised	0.964	-35.45	60.99	58.17	-2.82

Table 5.8: Estimated and actual Siesta binding energy errors for the benzene methane - The errors for the benzene methane complex are given in meV in the different columns. The density difference is the normalised density difference between the non counterpoise corrected methane monomer and the converged plane wave density. This is used to estimate the insufficient basis error, error in the binding energy due to the basis set not being the converged basis. We use the uncorrected *methane* monomer as this will give the largest estimate for this error. The BSSE values are taken from Figure 5.15. The actual errors are the differences between the Siesta calculated binding energies and the converged plane wave result. Here we give errors from both the non counterpoised corrected and corrected basis set calculations.

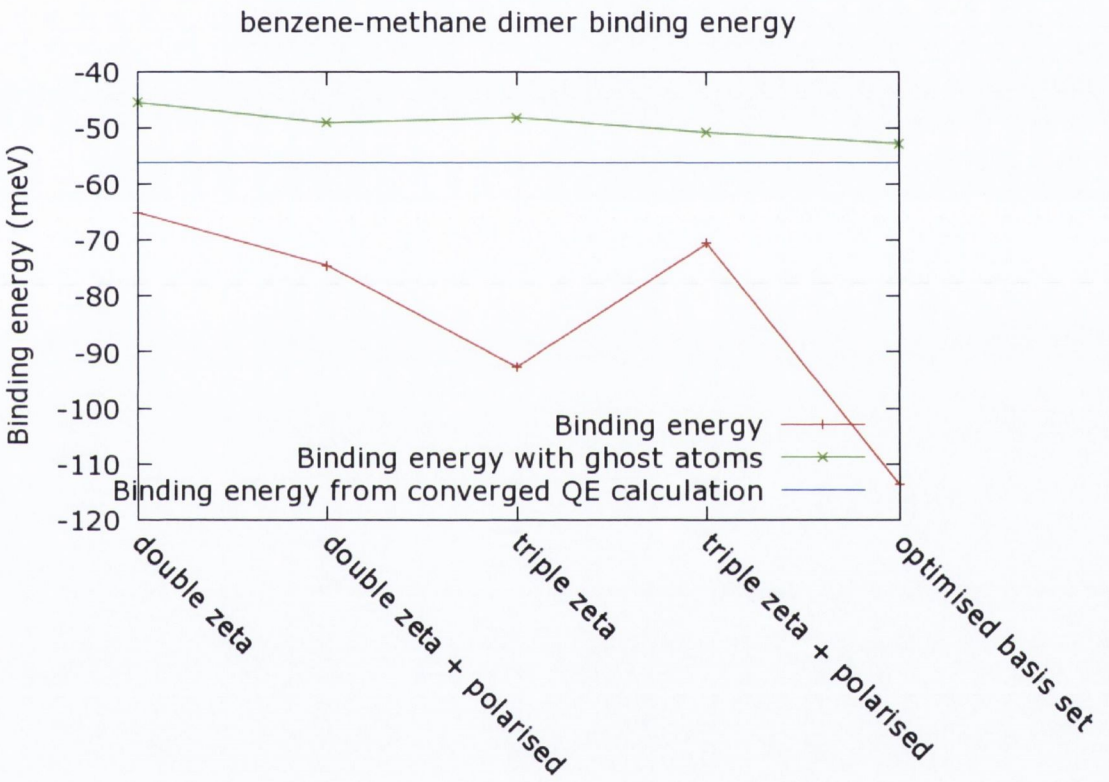


Figure 5.13: Benzene methane complex binding energy - Binding energy calculated for a selection of Siesta basis sets with and without the addition of ghost atoms to the monomer basis calculation.

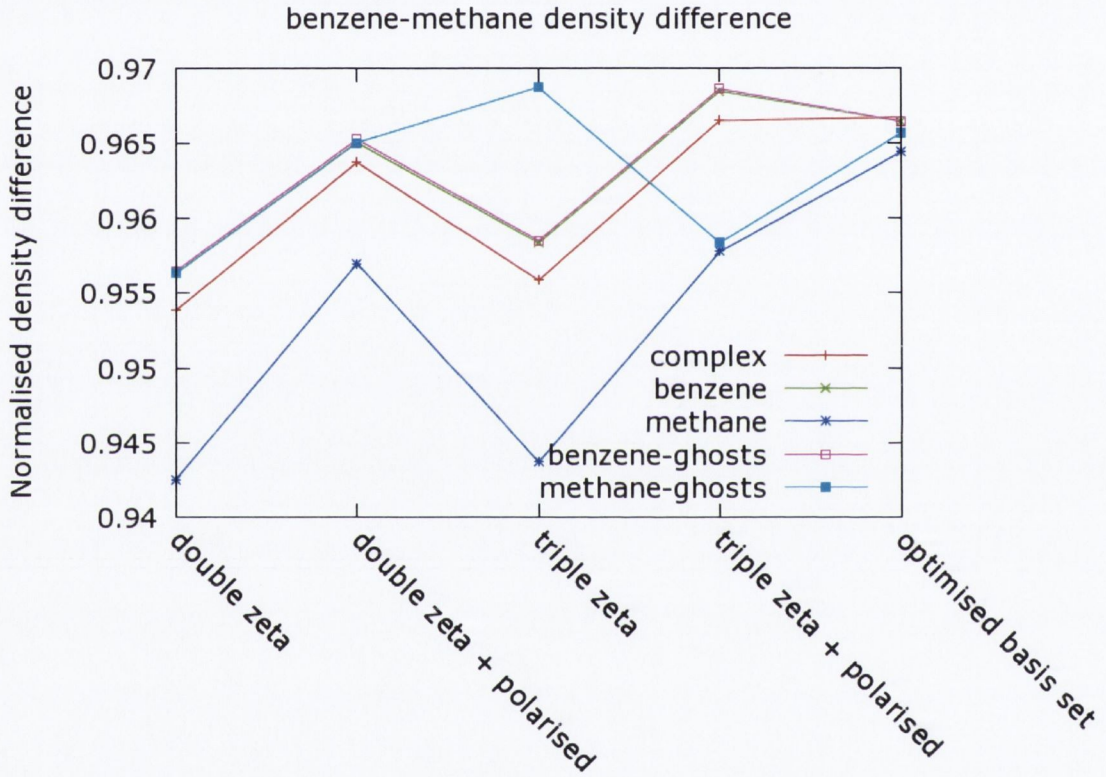


Figure 5.14: Normalised density difference for the benzene methane complex - Plot of the normalised density difference, equation (5.2.2), for the complex as well as the corrected and uncorrected monomers, corrected monomers are denoted by methane-ghosts and benzene-ghosts. The densities from the Siesta basis sets for each molecule is compared to the corresponding density from a converged QE calculation.

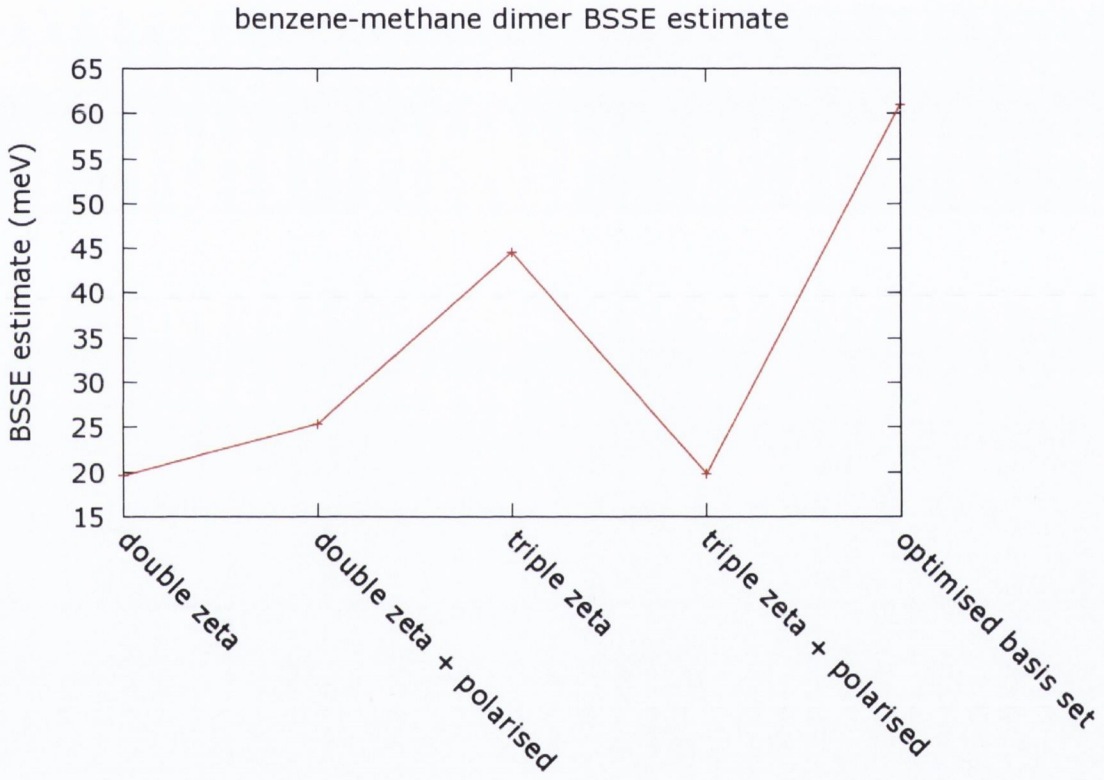


Figure 5.15: Estimate of the BSSE for the benzene methane complex - Using ghost atoms as a counterpoise correction an estimate of the BSSE can be obtained from the difference between the Siesta binding energies calculated with and without correction.

Collective trends from our density based error analysis.

The aim of our density based analysis of the errors in the four compounds was to extract general ideas about the relationship between the size or quality of a Siesta basis and the resulting accuracy of the calculated binding energy. Unlike in a plane wave basis where increasing the kinetic energy cutoff increases the *size* of the basis it is not clear how changing the parameters of our Siesta basis sets directly improves the basis. Here we refer to a generic "quality" of the basis as the idea of improving the basis by adding additional zetas, polarised orbitals or optimising the cutoffs of the basis functions. Indeed our results reflect this difficultly in determining how basis set changes alter the accuracy of calculations. Our optimised basis set results for the water and methane dimers give values comparable to those from the triple zeta + polarised basis. In contrast, neither the counterpoise corrected nor the uncorrected binding energies of the triple zeta + polarised or optimised basis sets are comparable with each other.

Our results from the water and formic acid dimers show a clear reduction in the insufficient basis error for basis sets which include polarised orbitals. This is not seen in the methane dimer nor methane benzene complex results. The need for polarised orbitals to better describe hydrogen bonded complexes is a direct consequence of hydrogen bond being an example of a dipolar bond. The covalent bonding of the highly electronegative oxygen to the low electronegative hydrogen creates a dipole and it is the interaction of these poles between the monomers which creates the strong intermolecular hydrogen bond. This is not seen in the dispersion bound methane dimer nor the methane benzene complex which is reflected in the consistent insufficient basis error for all basis sets. These results are consistent with dispersion interactions being an interaction between temporary, spontaneous multipoles; that is the multipoles fluctuate quickly enough and are evenly distributed across the monomers so that our

static DFT calculations do not need to consider orbital polarisations.

5.4.2 Analysis of vdW-DF S22 errors.

In this section we shall discuss two situations. Firstly we shall compare our Siesta calculated binding energies across the entire S22 database to the plane wave results of Lee *et al.* [56]. We will examine the standard basis with 3 modifications:

1. The standard basis with the addition of counterpoise corrections.
2. The standard basis with the addition of extra basis functions, in the form of additional zeta functions.
3. The standard basis with optimised cutoff lengths.

Secondly we shall put our S22 calculations in context with other atom centered basis set calculations of the S22 binding energy.

Figures 5.16 and 5.17 show the binding energy and differences in the binding energy from the Lee *et al.* [56] plane wave S22 results. We plot the energies and differences for a selection of Siesta basis sets. The double zeta + polarised, DZP, triple zeta + polarised, TZP, and optimised, OPT, basis sets were selected as the results from Section 5.4.1 indicated that these basis sets provided densities closest to that of the plane wave calculations. An additional basis set the double zeta + polarised and ghost atoms, DZP + ghosts, was also selected to illustrate how the inclusion of ghost atoms into a basis affects the accuracy of vdW-DF calculations in a broader setting.

Figure 5.16 indicates that the DZP, TZP and OPT basis results converge to values larger than the plane wave result; this is particularly evident for the dispersion and mixed binding compounds, compounds 8-22 of the S22 database. The counterpoise corrected DZP + ghosts basis under binds for the same regions of the S22 database. This effect can also be seen in Figure 5.17. In order to best compare the basis sets

and quantify which basis returns the best* results across the entire S22 database we calculated the relative and absolute errors with respect to the plane wave results of Lee *et al.* [56].

Table 5.9 shows the mean error, ME, mean absolute error, MAE, and mean absolute percentage error, MAPE, of our calculated values of the S22 binding energy with respect to the values from the plane wave calculations of Lee *et al.* [56]. These errors are defined as,

$$ME = \frac{1}{n}\sum_{i=1}^{n} e_i, \tag{5.4.4}$$

$$MAE = \frac{1}{n}\sum_{i=1}^{n} |e_i|, \tag{5.4.5}$$

$$MAPE = \frac{1}{n}\sum_{i=1}^{n} |p_i|, \tag{5.4.6}$$

where n is the number of cases to be averaged over, e_i is the error, $|e_i|$ is the absolute value of the error and p_i is the percentage error. Here we define the error as $Siesta_i - QE_i$ and the percentage error as $100\frac{Siesta_i - QE_i}{QE_i}$, where $Siesta_i$ and QE_i are the Siesta and QE values for the i^{th} complex of the S22 set. The binding energy values are taken to be positive values so a positive ME indicates over binding, a stronger than expected intermolecular bond, and a negative ME indicates under binding, a weaker than expected bond.

Collectively Table 5.9 and Figures 5.16 and 5.17 illustrate several important facts:

1. The ME indicates whether our calculated binding energies over or under bind. Across all categories we see that the DZP + ghosts underbinds, returning binding energies less than expected, while all our other basis sets overbind.

2. Both the MAE and MAPE errors show that our OPT basis results never per-

*i.e. results closest to those of the plane wave values

forms better than either the counterpoise corrected or TZP basis sets. The MAPE results for the total S22 database show it as the worst performing basis, beyond that of the DZP; this is a surprise given that it is a DZP basis with optimised cutoff parameters. The results of density based analysis suggested the OPT basis can give results which compare well with TZP basis sets. The failure of our OPT basis to perform across the entire S22 set is as a result of over optimising the basis using a single system. This highlights the difficultly in creating a transferable basis set suitable for a range of different chemical environments.

These results suggest that generally it is beneficial to include counterpoise corrections, as it greatly decreases the error for most calculations. The exception is for dispersion bound systems, here the correction from the ghost atoms is too extreme. For these low binding energy systems greater radial flexibility should be preferred.

	DZP	DZP + ghosts	TZP	OPT
ME (meV)				
hb	105.0	-30.9	59.9	55.4
dis	26.5	-34.9	29.9	23.7
mix	36.6	-16.1	32.2	37.8
total	54.7	-27.6	40.2	38.3
MAE (meV)				
hb	105.0	40.5	65.9	80.3
dis	34.7	36.4	36.5	37.8
mix	36.6	16.1	32.2	37.8
total	57.6	31.3	44.5	51.3
MAPE (%)				
hb	21.0	9.6	14.7	25.7
dis	20.4	21.2	18.6	27.0
mix	24.4	10.4	22.6	25.5
total	21.9	14.1	18.7	26.1

Table 5.9: Statistical errors of the S22 binding energies for various Siesta basis sets - The errors in our Siesta calculated binding energies with respect to the plane wave values of Lee *et al.* [56]. The Siesta basis sets are the same as those from Figure 5.16. The results are given both averaged across the total database as well as split amongst the various categories: hydrogen bonded, hb, dispersion bonded, dis, and mixed binding type, mix. We present several different statistical errors, the mean error, ME, the mean absolute error, MAE, and the mean absolute percentage error. Definitions of these can be seen in equations (5.4.4),(5.4.5), and (5.4.6). The ME indicates whether our calculated binding energies over or under bind. Across all categories we see that the DZP + ghosts underbinds, returning binding energies less than expected, while all our other basis sets overbind. The MAE indicates that our OPT basis fails to perform any better than the TZP or DZP + ghost basis sets. The MAPE indicates that TZP basis gives a lower and more consistent error across the dispersion bound complexes than the DZP + ghost basis.

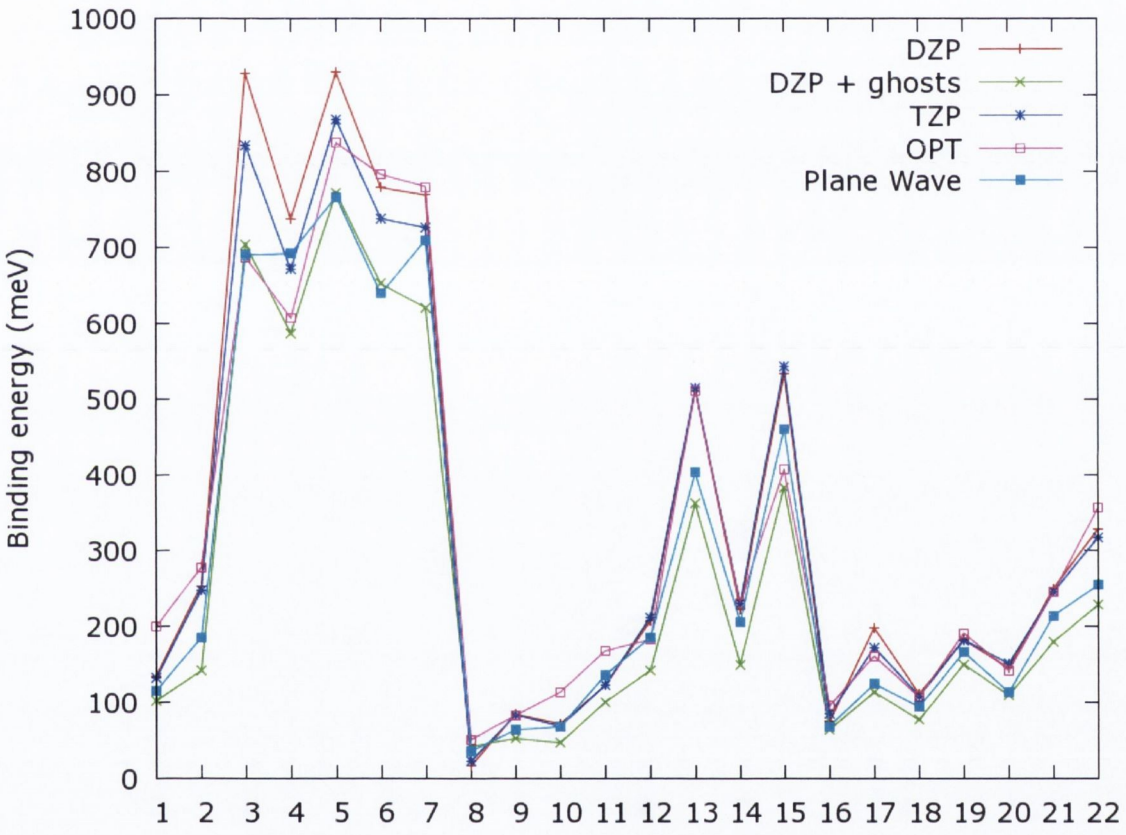


Figure 5.16: S22 Binding energies - The binding energies of the 22 compounds of the S22 database calculated with the double zeta + polarised, DZP, double zeta + polarised and ghost atoms, DZP + ghosts, triple zeta + polarised, TZP, and optimised, OPT, Siesta basis sets. The plane wave results are those from Lee *et al.* [56]. The three binding type categories can be seen in the plot: hydrogen bonded, 1-7, dispersion bonded, 8-15, and mixed bonding, 16-22.

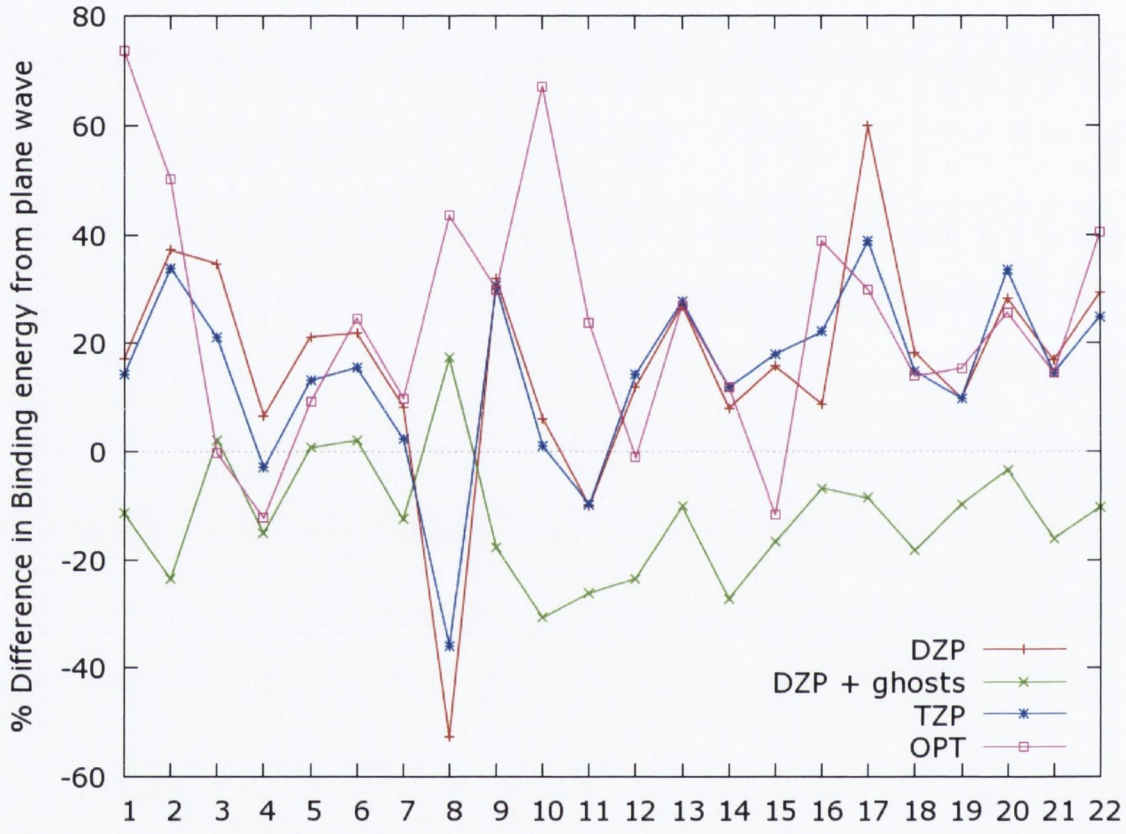


Figure 5.17: Differences between our calculated S22 binding energies and plane wave values - The binding energy differences between our Siesta calculations and the plane wave calculations of Lee *et al.* [56]. Plotted are the differences for several Siesta basis sets: the double zeta + polarised, DZP, double zeta + polarised and ghost atoms, DZP + ghosts, triple zeta + polarised, TZP, and optimised, OPT. Note how the non corrected basis sets, DZP, TZP and OPT, all tend to over bind with values greater than zero while the DZP + ghosts counterpoise corrected basis set appears to over correct and result in values less than zero, indicating under binding.

	This work				
	DZP + ghosts	TZP	Gaussian [103]	NAO [104]	Plane wave [56]
MAE (meV)					
hb	60.2	43.5	76.7	91.0	84.6
dis	52.0	17.5	54.7	14.0	20.9
mix	36.4	15.8	40.0	21.2	21.1
total	49.7	25.3	57.0	41.5	41.2

Table 5.10: Comparison of mean absolute errors in the S22 binding energies for our Siesta basis sets to literature results - The errors in our Siesta calculated binding energies with respect to the coupled cluster results of Jurečka *et al.* [98]. For comparison we also show the calculations of Vydrov and Van Voorhis [103], done in a Gaussian aug-cc-pVTZ basis, Marom *et al.* [104], done with a FHI-AIMS NAO basis equivalent to an aug-cc-pVQZ Gaussian basis, and the plane wave results of Lee *et al.* [56]. The results of our DZP + ghosts calculation are in good agreement with the literature results. Our TZP results for the dispersion bound subset of the S22 database show a better agreement to the NAO and plane wave results than that of the counterpoise corrected basis. This is in agreement with the errors we see in table 5.9.

5.4.3 Comparison to literature results.

From the results of table 5.9 we selected the DZP + ghosts and TZP basis sets as those which performed the best, returning the lowest errors in comparison to the plane wave results of Lee *et al.* [56]. In order to compare our results to others in the literature we have calculated the MAE with respect to the coupled cluster results of Jurečka *et al.* [98]. Table 5.10 shows these results for our basis set calculations as well as the calculations of Vydrov and Van Voorhis [103], done in a Gaussian aug-cc-pVTZ basis, Marom *et al.* [104], done with a FHI-AIMS NAO basis equivalent to an aug-cc-pVQZ Gaussian basis, and the plane wave results of Lee *et al.* [56]. For the DZP + ghosts basis our total MAE is in good agreement with the other literature results. The average error for the dispersion bound compounds however highlights that for this subset of the S22 compounds our TZP errors more closely agree with those of the FHI-AIMS NAO basis and plane wave results. We suspect that our DZP + ghosts dispersion error matches that of the Gaussian [103] basis as both use counterpoise

corrections. The percentage error and MAPE shown in Figure 5.17 and table 5.9 illustrate how the addition of counterpoise corrections can over correct for the BSSE and give worse than uncorrected results.

5.5 Conclusions

In this work we have examined how modifying the Siesta basis set affects the accuracy of the vdW-DF binding energies. We benchmarked several basis sets using the S22 molecular database and compared the error in these results to values seen in the literature. Comparisons were made with both converged plane wave DFT calculations as well as with other atom centered basis set codes. Additionally, through careful examination of the densities produced from these basis sets and comparison with plane wave converged densities we explored the origins of the errors in the binding energies; accounting for what originates from insufficiently large basis sets and what is the result of basis set superposition errors.

The modifications explored were, addition of counterpoise corrections, increasing the radial flexibility and the optimisation of cutoff lengths. By applying these modified basis sets to the molecules of the S22 database, clear and distinct trends can be identified. Our density based analysis of the water, formic acid and methane dimers as well as the benzene-methane complex indicated two distinct facts:

1. The addition of ghost atoms does not eliminate the BSSE, it does however shift the binding energies closer to those of the plane wave values.

2. If the number of atoms in a molecule is small enough, no modification to the basis set will allow for the generation of an accurate density.

Problems with counterpoise corrections are not new. Schwenke and Truhlar [102] showed that neither increasing the size of the basis nor the inclusion of counterpoise corrections guarantee an increase in the accuracy of the interaction energy. Loushin *et al* [105] suggest that when examining a hydrogen bonded system, simple counterpoise correction will never be sufficient. The dipole field of one monomer will have an effect on the second. They propose a polarisation counterpoise correction that add both

ghost atoms and point charges to the monomer calculations.

More recently Hamza *et al* [106] discuss an alternative "Chemical Hamiltonian Approach" to BSSE correction. In this approach the supermolecule molecular orbitals are expanded in terms of only a single monomer basis. They criticise this approach as it fails to allow for the true charge transfer in the complex.

We also presented the ME, MAE and MAPE errors of our Siesta calculated S22 binding energies with respect to the plane wave results of Lee *et al.* [56]. From these we draw the following general suggestion:

> The use of counterpoise corrections greatly decreases the error in binding energy calculations. The exception is dispersion bound systems, here the correction from the ghost atoms is too extreme. Better results can be obtained by adding extra zetas to the basis to increase the radial flexibility.

Chapter 6

A comparison of the overlayer adsorption of graphene onto a Bi_2Se_3 slab using the vdW-DF and recent beyond pairwise approximation methods.

6.1 Introduction

Since the experimental realisation of graphene [107], a multitude of 2D or quasi-2D materials have attracted the intense focus of both theoretical and experimental researchers. Such materials include the atomically thin hexagonal boron nitride, main group IV element based materials such as silicene and gemanene, ultra-thin materials which are larger than one atom thick such as the hydrogenated graphene, silicene and gemanene derivatives as well as the transition metal chalcogenides such as Molybde-

num disulphite [108]. This range of materials derive into a rich variety of electronic properties including metals, semimetals, insulators and semiconductors with direct and indirect band gaps ranging from ultraviolet to infrared throughout the visible range.

Recently research focus has shifted from the extraction of mono-layers from the bulk to the construction of 3D composite materials. In doing so, the hope is to create new materials with potentially bespoke electronic structures [109].

As the individual layers bind via vdW interactions such materials can be, relatively, easily constructed experimentally. Using method such as molecular beam epitaxy, MBE, low defect single mono-layers can be accurately and reliably grown. This process has been named van der Waals epitaxy [110, 111], to distinguish it from the more commonly used crystalline epitaxy. Due to the weak interlayer interaction, a mono-layer grows from the beginning with its own lattice constant forming an interface with only a small amount of defects. This relaxed lattice matching condition permits to combine almost any layered material. Additionally, due to the precise control of growth parameters, it is possible to realise experimental structures with any range of layers.

The most popular vdW methods currently in use in the DFT community are based on the DFT+D[112] and vdW-DF[113] methods. These however are based on the pairwise summation approximation. While this approximation is reasonable for distantly separated molecules in a vacuum, it breaks down for low dimensional solids and metallics [70, 68]. For these systems, beyond pairwise addition methods are necessary.

Electrostatic screening can be thought of as a first approximation to beyond pairwise addition methods. It is the result of coordinated electron-electron interactions in the media surrounding the interacting charges [24].

Here we will focus on four distinct classes of dispersion approximations:

- the pairwise summation method of Tkatchenko and Scheffler, TS-vdW [44];
- the pairwise summation approximation using self consistently screened C6 parameters, TS-vdW+SCS [114];
- the Langreth-Lundqvist vdW density functional, vdW-DF[49];
- the many bodied vdW method of Tkatchenko and Scheffler, vdW+MB [4].

In the DFT community there has been prior work incorporating screened interactions into XC functionals [115, 116, 117]. These functionals work by using a screened version of the Hartree-Fock potential. In doing so they attempt to introduce part of the correlation effects in the exchange hole [118]. In the methods we have introduced, screening is applied to the long range dispersion correction. This is accomplished with an approximate dielectric function, for the vdW-DF method, or with self consistently screened corrections to the molecular polarisabilities, for the TS-vdW+SCS and vdW+MB methods.

In the vdW-DF method, the dielectric function is approximated using a homogeneous dielectric function [84, 76, 49, 48]. Such a method was expected to be accurate for molecules, whose densities can vary quickly. However interaction energies between small organic molecules computed with such functionals are reasonably accurate [57, 56]. Metallic systems suffer though and modifications to the exchange term are necessary to get satisfactory results [61].

Topological insulators exhibit a novel quantum state, conductive topologically-protected surface states lying within the bulk energy gap [120, 121, 122]. These surface states are expected to have applications in spintronics, quantum computation as well as other areas [123, 124, 125, 126]. The semiconducting bismuth chalcogenides have been identified as three dimensional topological insulators and are the most

extensively studied. Our focus shall be on Bi_2Se_3. These materials are known to crystallise into a bulk layered structure, see Figure 6.1, with rhombohedral symmetry $R\bar{3}m$ (D^5_{3d}) [119]. In the out of plane direction, the atoms are arranged in a layered structure with hexagonal planes of Bi and Se as Se1-Bi-Se2-Bi-Se1, where Se1 and Se2 denote the two inequivalent Se atoms in the crystal

The individual quintuple layers are internally bound quite strongly, however the interlayer binding is via weak van der Waals. Ab inito structural studies, using local and semi-local XC functionals, have produced intra-layer lattice parameters* which closely match experimental measurements [127, 128]. For the out of plane parameters, however, the inclusion of dispersion forces becomes necessary [129]. Recently discussions regarding the influence of many body effects upon the vdW force for molecular solids and extended molecules [130] as well as graphene [131] have highlighted the need for beyond pairwise approximations for improved accuracies. Correctly predicting the inter-quintuple distances as well as adsorption distances is important, as these materials can undergo a range of electronic structure modifications as a result of strain engineering [132, 133] as well as substrate effects[134].

In this chapter we will apply the four dispersion methods introduced to two systems:

1. Bilayer graphene. The binding of AA and AB stacked graphene sheets provides an interesting system to benchmark the different screening methods. Both the individual graphene as well as the bilayer are metallic in nature. It is well known that that Coulomb screening in graphene layers is also unique. With many experimental and accurate computational results for both stackings the bilayer systems are a good benchmark for our vdW methods.

2. A graphene overlayer atop a Bi_2Se_3 slab. This is a complicated system needing

*see appendix for lattice parameters

dispersion forces for the physisorption of the overlayer as well as the binding of the Bi_2Se_3 quintuple layers in the slab. An additional complication is the metallic surface states of Bi_2Se_3 [135]. These difficulties make it a challenging test for beyond pairwise dispersion methods. The graphene-Bi_2Se_3 system is important as the experiments for thin films of Bi_2Se_3 are carried out atop graphene substrates [136].

6.2 Computational Methods

The bilayer graphene binding curves were calculated with the FHI-AIMS DFT code [137]. The calculations were performed using the default "tight" grid and including all atomic basis functions up to "tier 2" [138].

The grid parameters are optimised, pre-calculated divisions of atomic basis functions as determined by the FHI-AIMS developers. By grouping the atomic basis functions into tiers, in order of importance, accurate calculations can be achieved using a minimal basis set. For our calculations these parameters are expected to give converged energies to within 2 meV.

The calculations used a 16x16x1 kpoint grid and 4×4 supercell. The in-plane lattice parameter was kept fixed at the experimental value of 2.467 Å [139].

We confirmed these parameters were sufficient by calculating AB stacked bilayer graphene, at a separation of 3.3 Å, using LDA XC. The calculated binding energy was found to be 32.23 meV/atom, in good agreement with previous calculations [35].

The van der Waals contributions were added to GGA self consistent calculations in a post processing manner, ensuring the same flavour GGA functions were used for the self consistent and post processing calculations. We paired the vdW-DF non-local correlation with both the PBE [27] and revPBE [28] exchange. The TS-vdW, TS-vdW+SCS and vdW+MB methods are paired with the PBE XC. Our TS-vdW and

TS-vdW+SCS calculations used the standard damping function parameters, d=20 and s_r=0.94 [44]. For the vdW+MB calculations the beta factor was set to 2.56 [4].

The vdW-DF functional was evaluated using the linear scaling real space algorithm of Gulans *et al.* [57]. The non-local correlation was integrated using a grid comprising of 11 radial points and 11 Lebedev grid points. The density was interpolated, using an octree structure, to an accuracy of 1e-4 Rydberg.

The structural optimisation of the Bi_2Se_3-graphene complex was done with the FHI-AIMS DFT code [137]. The calculations were performed using the default "tight" grid and including all atomic basis functions up to "tier 2" [138]. The calculations used a 16x16x1 kpoint grid and a Gaussian broadening of 0.01 eV. Relativistic effects were included using the scalar atomic ZORA, zero-order regular approximation. For the structural optimization we have ignored spin-orbit coupling as this is not expected to greatly affect the structure [129, 127, 128]. We fixed the in-plan lattice constant to the experimental value of 4.138 Å [119]. Our use of a $\sqrt{3} \times \sqrt{3}$ in-plan supercell for graphene corresponds to a lattice mismatch of about 2.9%.

For the bandstructure calculations we used Quantum Espresso[87] with a 30 Ry kinetic energy cutoff. An 8x8x1 kpoint grid, Methfessel-Paxton smearing of 0.001 Ry and spin-orbit coupling. The bandstructures were calculated using the un-relaxed and relaxed structures from our FHI-AIMS calculations. The pseudopotentials used for bismuth and selenide were taken from Kucukbenli *et al.* [140]. They are fully relativistic, ultrasoft [141] type with non-linear core corrections.

Method	Interlayer distance (Å)	Interlayer binding energy (meV/atom)
PBE	4.13	-0.0
revPBE vdW-DF	3.75	-33.5
PBE vdW-DF	3.63	-47.9
TS-vdW	3.72	-35.9
TS-vdW+SCS	3.74	-25.4
vdW+MB	3.81	-19.5
DMC	3.50	-11.5
Exp	3.55	-

Table 6.1: AA stacked bilayer binding curve results - Interlayer binding distances and energies for several vdW methods. The values are extracted from quadratic functions fitted about the minima of binding curves seen in Figure 6.2. Experimental, Exp, interlayer distance taken from [143] for AA stacked graphite. Diffusion Monte Carlo, DMC, results from [142].

6.3 Results

6.3.1 Interlayer binding in bilayer graphene.

Figure 6.2 shows the binding curves for the AA stacked bilayer graphene as calculated with the different vdW methods. By fitting quadratic functions about the curve minima we obtain the binding energies and distances for each vdW method, these are shown in Table 6.1. Excluding the PBE method which does not bind, the vdW methods tested return binding distances whose errors, with respect to the experimental distance of 3.55Å, range from 2-7%. While all the vdW methods overbind with respect to the DMC results from [142], it is the methods which explicitly include non-local correlation screening which overbind least. Specifically the self consistent screening of the SCS-TS-vdW and TS-MBD methods. The results of the density based vdW-DF method, with revPBE exchange, agree closely with those of the TS-vdW, with no non-local screening.

Method	Interlayer distance (Å)	Interlayer binding energy (meV/atom)
PBE	4.13	-1.0
revPBE vdW-DF	3.61	-37.6
PBE vdW-DF	3.44	-55.4
TS-vdW	3.59	-40.8
TS-vdW+SCS	3.58	-29.9
vdW+MB	3.67	-22.8
DMC	3.38	-17.7
Exp	3.40	-

Table 6.2: AB stacked bilayer binding curve results - Interlayer binding distances and energies for several vdW methods. The values are extracted from quadratic functions fitted about the minima of binding curves seen in Figure 6.3. Diffusion Monte Carlo, DMC, results from [142]. Experimental, Exp, interlayer distance taken from [107] for AB stacked bilayer graphene.

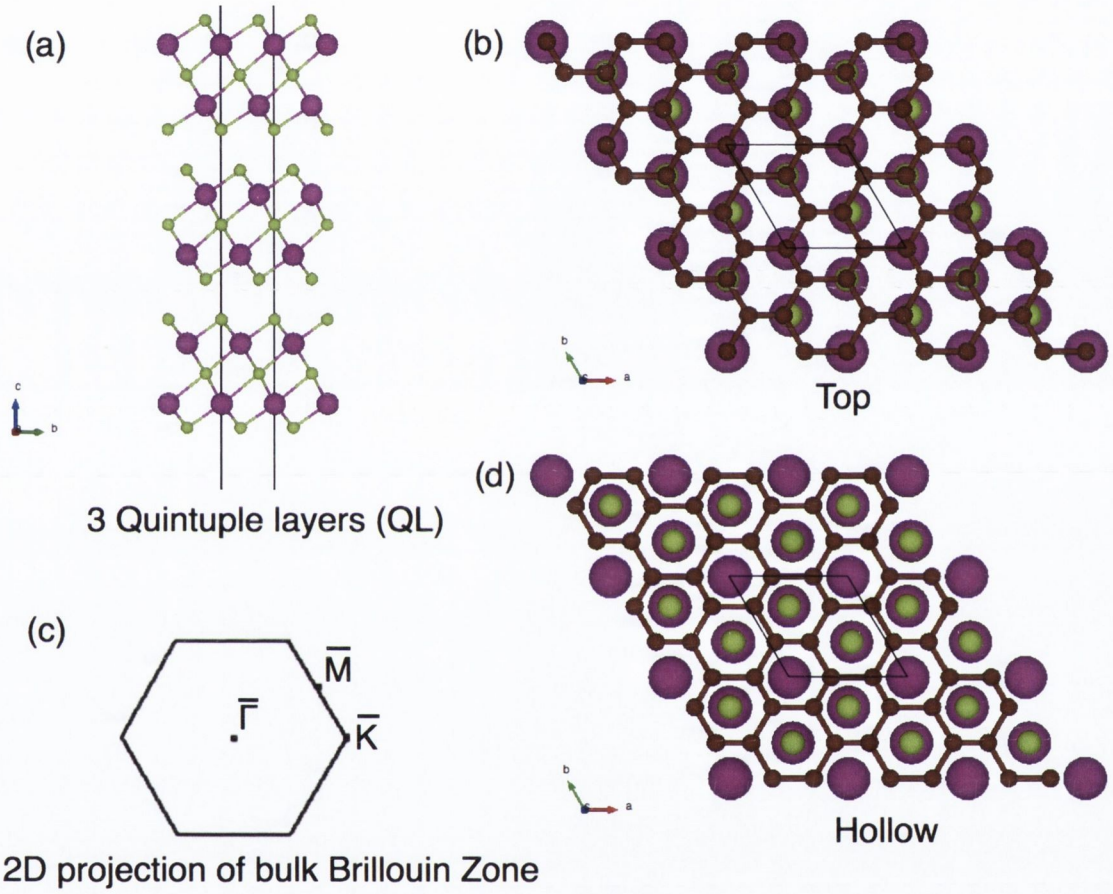


Figure 6.1: Bi_2Se_3-graphene structures - The Bi_2Se_3-graphene structures examined in this work. **(a)** The three quintuple layer, QL, slab. Each QL is comprised of five atoms which are stacked in a repeating ABC arrangement. In the bulk Bi_2Se_3 has a rhombohedral symmetry, $R\bar{3}m$ (D^5_{3d}) [119]. **(b)** The $\sqrt{3} \times \sqrt{3}$ graphene overlayer atop the (0001) Bi_2Se_3 surface. In this orientation the carbon atoms of the graphene lie on-top of the topmost selenium surface atoms. **(c)** The 2D projection of the bulk Brillouin zone of the Bi_2Se_3 onto the (0001) surface. **(d)** The $\sqrt{3} \times \sqrt{3}$ graphene overlayer atop the (0001) Bi_2Se_3 surface. In this orientation the carbon atoms of the graphene lie in the hollows of the topmost selenium surface atoms.

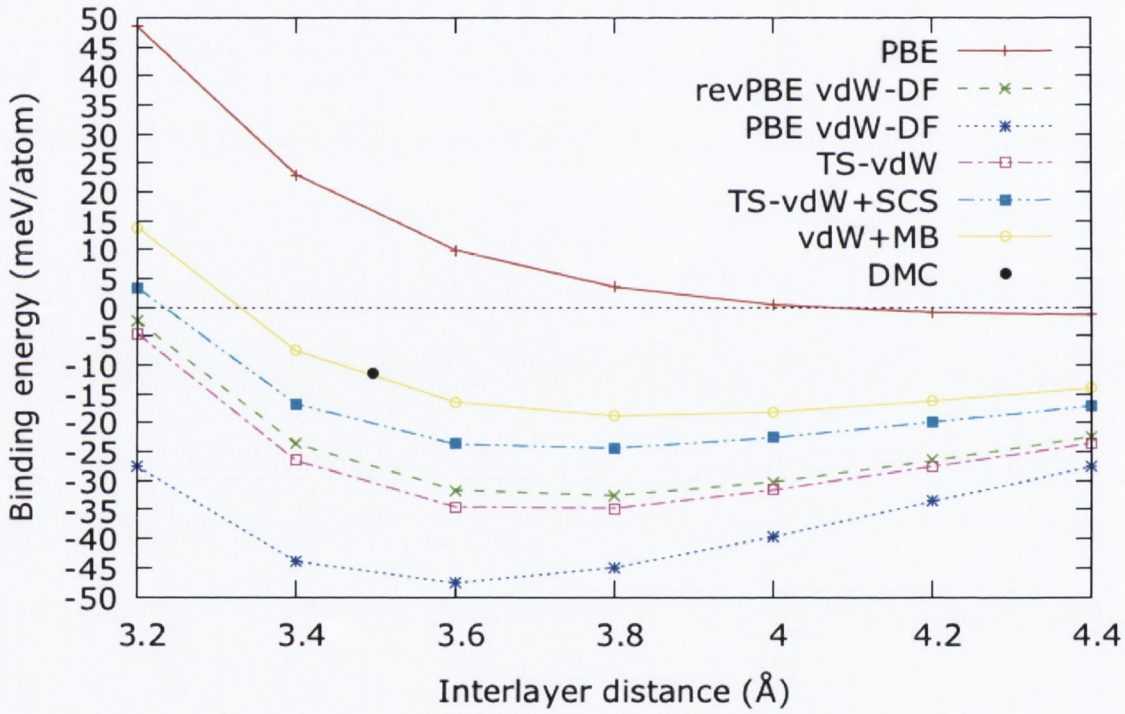


Figure 6.2: AA stacked bilayer binding curves - Interlayer binding curves for several vdW methods. Diffusion Monte Carlo, DMC, results from [142]. Binding energies and distances extracted from these curves are shown in Table 6.1.

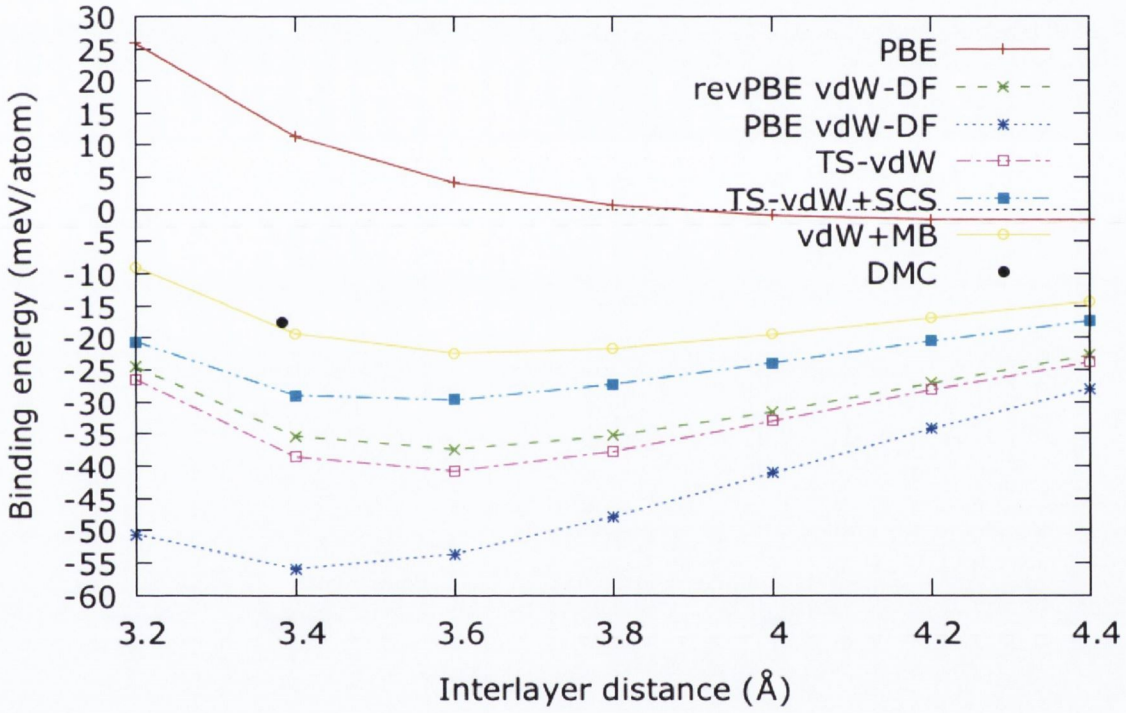


Figure 6.3: AB stacked bilayer binding curves - Interlayer binding curves for several vdW methods. Binding energies and distances extracted from these curves are shown in Table 6.2.

Number of QLs	Overlayer binding energy(meV/atom)
1	-24.041
2	-24.554
3	-24.745
4	-24.597

Table 6.3: Convergence of the overlayer binding energy with respect to the number of QLs in a Bi_2Se_3-graphene slab. - Convergence of the overlayer binding energy, as defined in equation (6.3.1), with respect to the number of quintuple layers in a Bi_2Se_3 slab. The Bi_2Se_3 QL atomic coordinates and inter-QL distances are taken from the bulk experimental parameters [119]. The graphene overlayer is a $\sqrt{3} \times \sqrt{3}$ in-plan suerpcell, separated from the top Bi_2Se_3 QL by 3.5 Å. The binding energy was calculated with the TS-vdW method without self consistent screening. The results show that the binding is relatively insensitive to the number of QLs in the Bi_2Se_3 slab.

6.3.2 Relaxation of three quintuple layer Bi_2Se_3 slab.

To obtain the correct Bi_2Se_3 surface geometry we constructed a three quintuple layer, QL, slab with 15 Å vacuum separation between layers. The internal coordinates of each QL was kept fixed at the bulk experimental coordinates [119]. Our initial testing showed that the binding of a graphene overlayer to a Bi_2Se_3 slab was relatively independent of the number of QLs in the slab. These results are shown in Table 6.3.

We define the overlayer binding energy for this system as

$$BE = (E_{Bi_2Se_3-graphene} - E_{Bi_2Se_3} - E_{graphene})/N, \tag{6.3.1}$$

where $E_{Bi_2Se_3-graphene}$ is the energy of the Bi_2Se_3-graphene system. Similarly $E_{Bi_2Se_3}$ and $E_{graphene}$ are the energies of the Bi_2Se_3 and graphene systems respectively. For comparison with other works we divide the binding energy by the total number of carbon atoms in the overlayer, N.

We fix the atomic positions of the middle QL and symmetrically relax the relative inter-QL separations of the top and bottom QLs from the middle QL. This method of geometry optimisation was chosen as the TS methods we are using are post-processing

Method	Top-middle QL separation(Å)	Middle-bottom QL separation(Å)
revPBE	5.560	5.560
PBE	3.504	3.504
revPBE vdW-DF	3.412	3.412
PBE vdW-DF	3.105	3.105
TS-vdW	3.186	3.186
TS-vdW+SCS	3.182	3.182
vdW+MB	3.377	3.377
Bulk	2.579	2.579

Table 6.4: Inter-QL distances in a relaxed 3 QL slab - Inter-QL separation distances of the top and bottom QLs from the middle QL. The bulk values are taken from the bulk experimental coordinates [119]. The distances are along the (0001) direction, out of plane, perpendicular to quintuple layers. Relaxation was done with constrained x and y, in-plane, coordinates as well as fixed intra-QL distances. Only the relative distance between the top and middle QLs as well as the bottom and middle QLs was optimised. The separations of the top and bottom QLs from the middle QL were optimised simultaneously to maintain the symmetry of the slab.

methods, meaning we don't have access to the non-local forces.

Table 6.4 shows the relaxed distances of the top and bottom QLs from the middle QL. As expected the semi-local revPBE and PBE methods have the longest inter-QL spacing due to the lack of long range correlations. The PBE C6 and PBE SCS C6 methods match to within 0.04 Å, suggesting that the vdW binding within the Bi_2Se_3 slab does not undergo much charge screening. This is reasonable as both the single QL as well as the bulk crystal are known to be insulators [134, 136]. The experimental bulk inter-QL separation [119] is denoted 'Bulk'.

Figure 6.4 shows the 2D surface band structure of our 3 QL Bi_2Se_3 slab. These are calculated using the PBE XC at the inter layer separations shown in Table 6.4 and at the bulk experimental separations, labeled 'Bulk'. The 2D Brillouin zone is shown in Figure 6.1 and the bands are plotted along the k-path, $\bar{K}$-$\bar{\Gamma}$-$\bar{M}$, using 40 k-points. At the 'Bulk' geometry the slab becomes a zero-gap semiconductor, this agrees well with other slab calculations for the surface band structure [144]. At our relaxed slab

Method	Band Gap at Γ point(eV)	QL separation(Å)
revPBE	1.291	5.560
PBE	1.127	3.504
revPBE vdW-DF	1.104	3.412
PBE vdW-DF	1.035	3.105
TS-vdW	1.063	3.186
TS-vdW+SCS	1.062	3.182
vdW+MB	1.103	3.377
Bulk	0.865	2.579

Table 6.5: Bi_2Se_3 slab band gap at Γ point - Γ point band gaps of the 3 QL Bi_2Se_3 slab, calculated at the relaxed slab geometries, Table 6.4. The band gap for the slab using the experimental bulk geometry [119] is denoted 'Bulk'. Also shown are the inter-QL separations, from Table 6.4, illustrating that the increase in the magnitude of the band gap coincides with the increase of the inter-QL separation.

geometries a gap opens between the valence and conduction bands. The magnitude of the gap scales with the magnitude of the inter-QL separation. Table 6.5 shows the band gap at Γ for all the band plots shown in Figure 6.4.

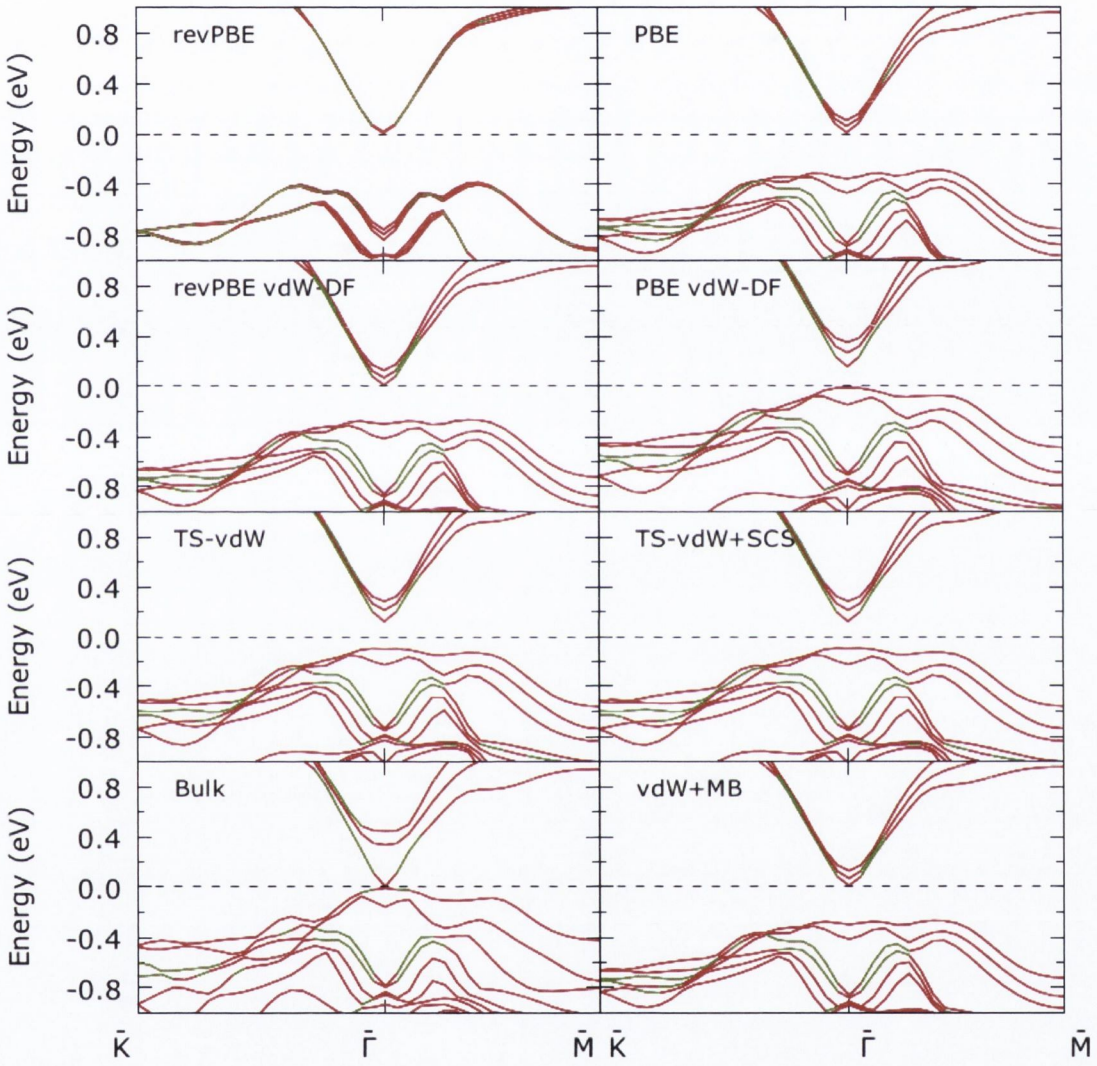


Figure 6.4: Bi_2Se_3 slab band structures - Band structures of the 3 QL Bi_2Se_3 slab, calculated at the relaxed slab geometries, Table 6.4. The band structure using the bulk experimental geometry [119] is denoted "Bulk". The 2D Brillouin zone of the surface is shown in Figure 6.1. The k points are taken along the path $\bar{K}$-$\bar{\Gamma}$-$\bar{M}$. The bands attributed to Bi_2Se_3 top QLs are marked in green. The bands are aligned at the Fermi level, which is plotted as the dashed grey line.

6.3.3 Adsorption of a graphene overlayer atop an unrelaxed Bi_2Se_3 slab.

To create our Bi_2Se_3-graphene heterostructure we first calculated the optimum overlayer distance with the graphene aligned in both the 'top' and 'hollow' positions. These positions are described in Figure 6.1, succinctly in the 'top' position the carbon atoms of the graphene overlayer are aligned on top of the top selenium atoms of the top QL. In the 'hollow' orientation, the carbon rings of the graphene overlayer form around the top selenium atoms.

Figures 6.5 and 6.6 show the binding energy curves, for the vdW methods under investigation, of a graphene overlayer atop an unrelaxed 3 QL Bi_2Se_3 slab in both the 'top' and 'hollow' orientations. The binding energy, as defined in equation (6.3.1), is normalised by the number of carbon atoms in the simulation cell.

Tables 6.6 and 6.7 show the binding energies and distances of the graphene overlayer in the two orientations. These values are extracted from the binding curves of Figures 6.5 and 6.6 by fitting cubic functions about the curve minima. Apart from the TS-MBD method, all the methods with non-local correlations calculated the 'hollow' orientation to be lower in energy than the 'top'. This suggests that the 'hollow' position is the preferred binding position for the overlayer, an observation which other researchers have also found [145].

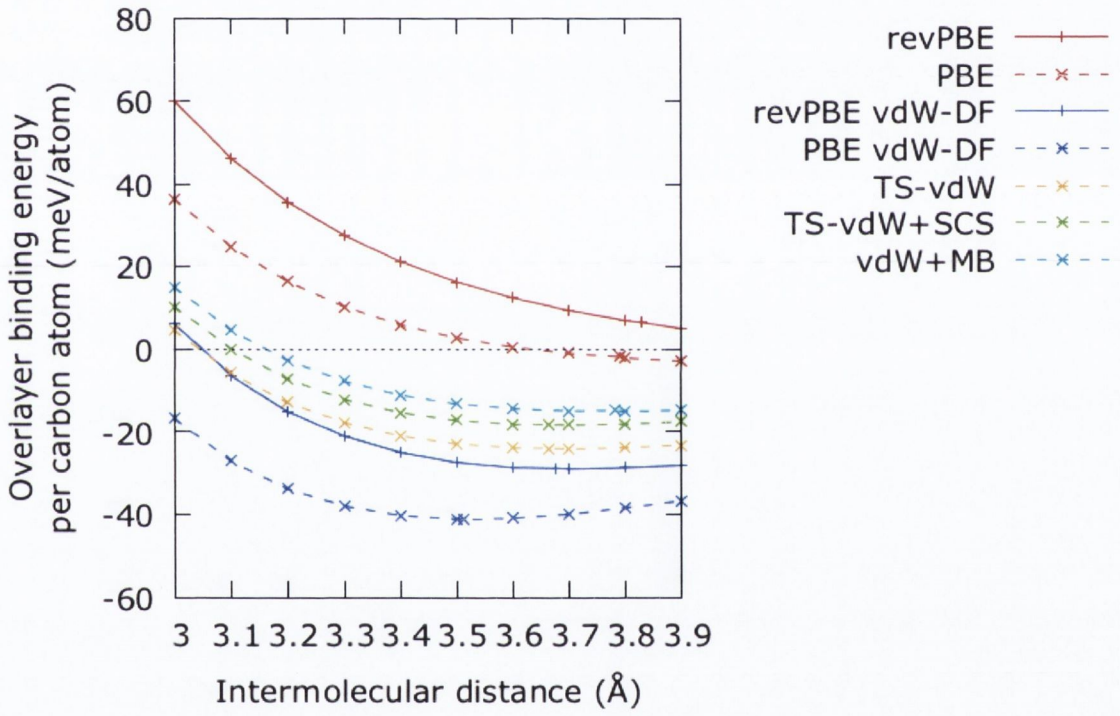


Figure 6.5: Binding energy curves for the unrelaxed Bi_2Se_3-graphene structure - top orientation - The binding energy of the $\sqrt{3} \times \sqrt{3}$ graphene overlayer atop the (0001) Bi_2Se_3 surface. Here the graphene is aligned in the "top" position as described in Figure 6.1. The Bi_2Se_3 slab is unrelaxed in its experimental coordinates [119]. The binding energy is defined in equation (6.3.1).

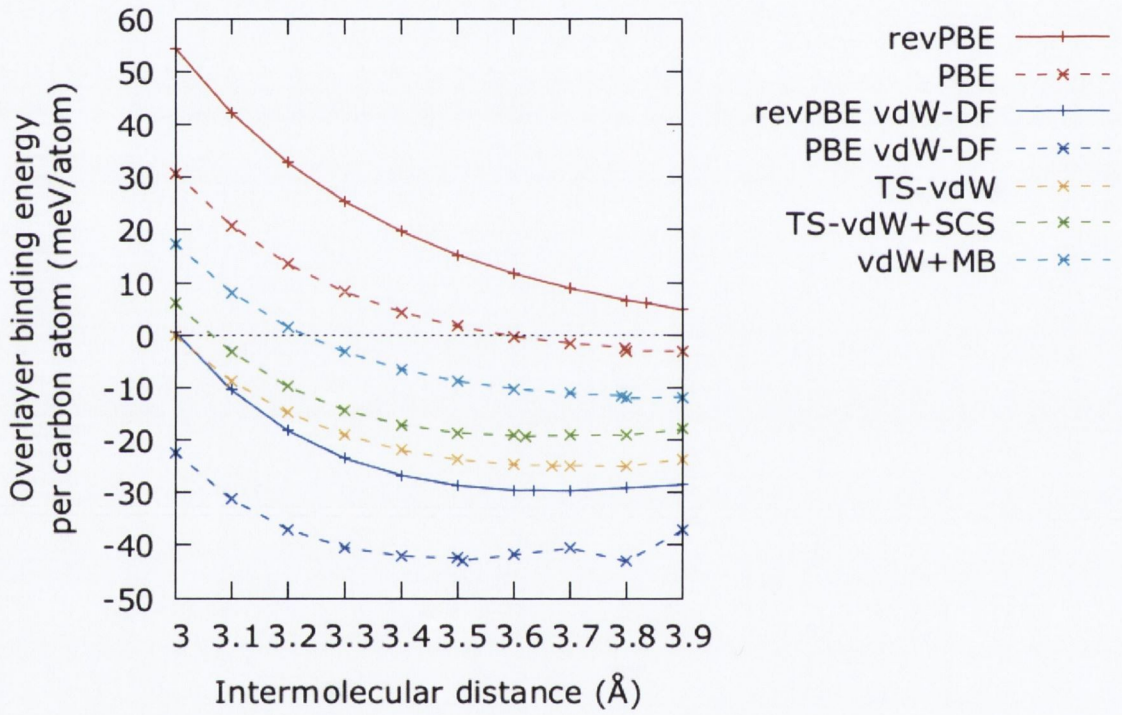


Figure 6.6: Binding energy curves for the unrelaxed Bi_2Se_3-graphene structure - hollow orientation - The binding energy of the $\sqrt{3} \times \sqrt{3}$ graphene overlayer atop the (0001) Bi_2Se_3 surface. Here the graphene is aligned in the "hollow" position as described in Figure 6.1. The Bi_2Se_3 slab is unrelaxed in its experimental coordinates [119]. The binding energy is defined in equation (6.3.1).

Method	Overlayer binding distance(Å)	Overlayer binding energy(meV/atom)
revPBE	unbound	n/a
PBE	3.790	-1.78
revPBE vdW-DF	3.677	-28.81
PBE vdW-DF	3.511	-41.30
TS-vdW	3.664	-23.98
TS-vdW+SCS	3.664	-18.26
vdW+MB	3.782	-14.81

Table 6.6: Results of binding energy curves for the unrelaxed Bi_2Se_3-graphene structure - top orientation - The binding energy and separation distance of the $\sqrt{3} \times \sqrt{3}$ graphene overlayer atop the (0001) Bi_2Se_3 surface. The values are then extracted from the binding curves of Figure 6.5 by fitting cubic functions about the curve minima. Here the graphene is aligned in the "top" position as described in Figure 6.1. The Bi_2Se_3 slab is unrelaxed in its experimental coordinates [119].

Method	Overlayer binding distance(Å)	Overlayer binding energy(meV/atom)
revPBE	unbound	n/a
PBE	3.796	-2.45
revPBE vdW-DF	3.635	-29.57
PBE vdW-DF	3.508	-42.89
TS-vdW	3.668	-24.86
TS-vdW+SCS	3.622	-19.29
vdW+MB	3.790	-11.48

Table 6.7: Results of binding energy curves for the unrelaxed Bi_2Se_3-graphene structure - hollow orientation - The binding energy and separation distance of the $\sqrt{3} \times \sqrt{3}$ graphene overlayer atop the (0001) Bi_2Se_3 surface. The values are then extracted from the binding curves of Figure 6.6 by fitting cubic functions about the curve minima. Here the graphene is aligned in the "hollow" position as described in Figure 6.1. The Bi_2Se_3 slab is unrelaxed in its experimental coordinates [119].

6.3.4 Adsorption of a graphene overlayer atop a relaxed Bi_2Se_3 slab.

Figures 6.7 and 6.8 show the binding energy curves, for the vdW methods under investigation, of a graphene overlayer atop a relaxed 3 QL Bi_2Se_3 slab in both the 'top' and 'hollow' orientations. The bottom QL remains fixed while the relative separation of the top two layers for each vdW method is defined in Table 6.4. The intra-QL atomic coordinates were kept fixed at the bulk coordinates [119].

Tables 6.8 and 6.9 show the binding energies and distances of the graphene overlayer in the two orientations. These values are extracted from the binding curves of Figures 6.7 and 6.8 by fitting cubic functions about the curve minima. With the relaxed slab geometry the TS-MBD method agrees with our other methods by showing the 'hollow' orientation to be lower in energy than the 'top'. Again, the observation that the 'hollow' position is the preferred binding position for the graphene overlayer has also been confirmed by other researchers [145].

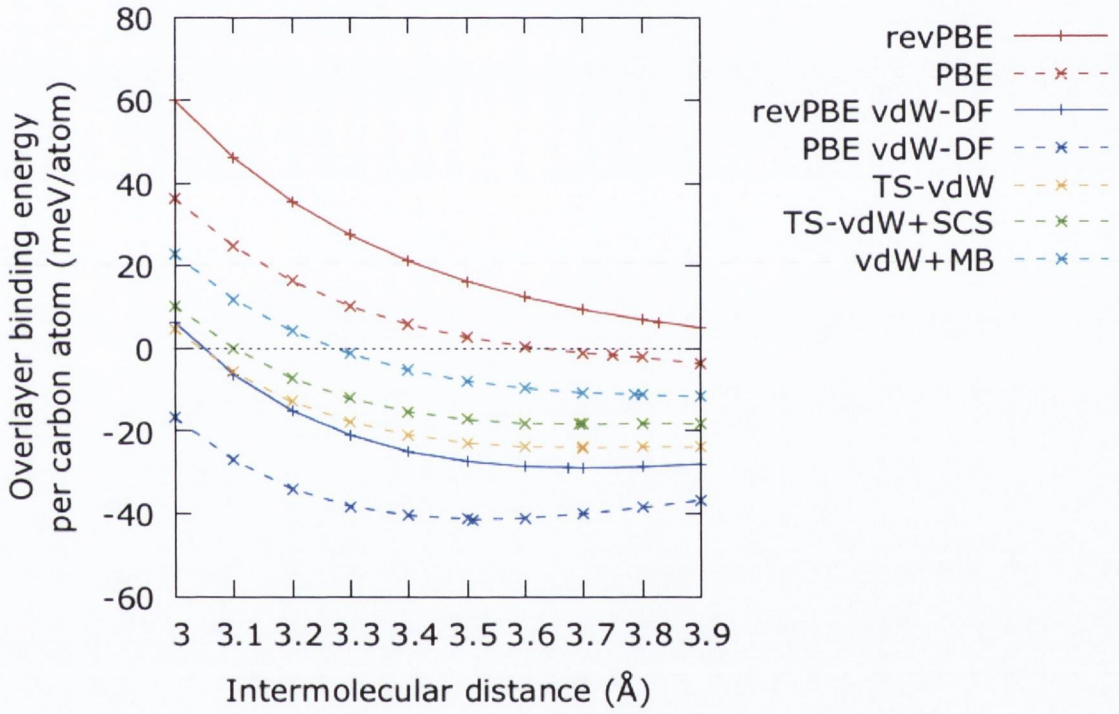


Figure 6.7: Binding energy curves for the relaxed Bi_2Se_3-graphene structure - top orientation - The binding energy of the $\sqrt{3} \times \sqrt{3}$ graphene overlayer atop the (0001) Bi_2Se_3 surface. Here the graphene is aligned in the "top" position as described in Figure 6.1. The Bi_2Se_3 slab is relaxed from its experimental coordinates [119], to the positions shown in Table 6.4 for each vdW method.

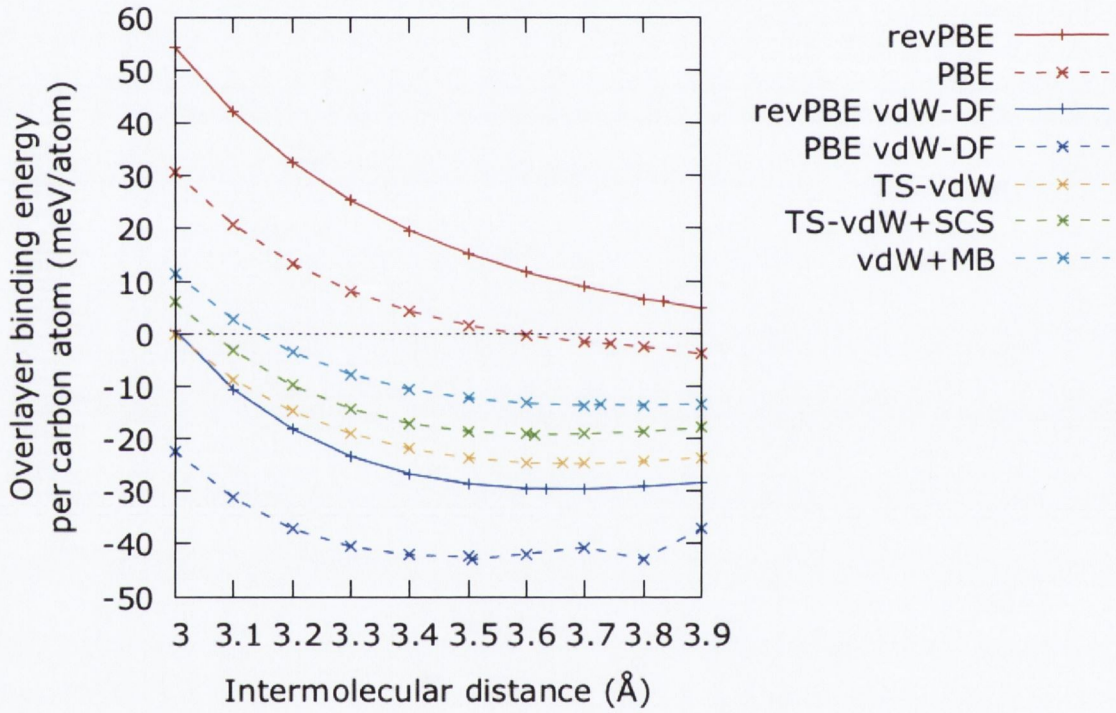


Figure 6.8: Binding energy curves for the relaxed Bi_2Se_3-graphene structure - hollow orientation - The binding energy of the $\sqrt{3} \times \sqrt{3}$ graphene overlayer atop the (0001) Bi_2Se_3 surface. Here the graphene is aligned in the "hollow" position as described in Figure 6.1. The Bi_2Se_3 slab is relaxed from its experimental coordinates [119], to the positions shown in Table 6.4 for each vdW method.

Method	Overlayer binding distance(Å)	Overlayer binding energy(meV/atom)
revPBE	unbound	n/a
PBE	3.750	-1.55
revPBE vdW-DF	3.674	-28.75
PBE vdW-DF	3.509	-41.46
TS-vdW	3.699	-23.94
TS-vdW+SCS	3.694	-18.25
vdW+MB	3.785	-11.01

Table 6.8: Results of binding energy curves for the relaxed Bi_2Se_3-graphene structure - top orientation - The binding energy and separation distance of the $\sqrt{3}\times\sqrt{3}$ graphene overlayer atop the (0001) Bi_2Se_3 surface. The values are the extracted from the binding curves of Figure 6.7 by fitting cubic functions about the curve minima. Here the graphene is aligned in the "top" position as described in Figure 6.1. The Bi_2Se_3 slab is relaxed in its experimental coordinates [119], to the positions shown in Table 6.4 for each vdW method.

Method	Overlayer binding distance(Å)	Overlayer binding energy(meV/atom)
revPBE	unbound	n/a
PBE	3.745	-2.02
revPBE vdW-DF	3.635	-29.53
PBE vdW-DF	3.506	-42.98
TS-vdW	3.661	-24.71
TS-vdW+SCS	3.615	-19.20
vdW+MB	3.726	-13.48

Table 6.9: Results of binding energy curves for the relaxed Bi_2Se_3-graphene structure - hollow orientation - The binding energy and separation distance of the $\sqrt{3}\times\sqrt{3}$ graphene overlayer atop the (0001) Bi_2Se_3 surface. The values are the extracted from the binding curves of Figure 6.7 by fitting cubic functions about the curve minima. Here the graphene is aligned in the "hollow" position as described in Figure 6.1. The Bi_2Se_3 slab is relaxed in its experimental coordinates [119], to the positions shown in Table 6.4 for each vdW method.

6.3.5 Electronic bandstructure of Bi_2Se_3-graphene composite.

Figures 6.9 and 6.10 show the 2D surface band structure of our relaxed Bi_2Se_3-graphene composite. These are calculated using the PBE XC at the inter layer separations shown in Table 6.4 with the graphene overlayer at the distances described in Tables 6.8 and 6.9. The bands are plotted along the k-path, K-Γ-M using 40 k-points. At each k-point we project the eigenstates corresponding to each eigen-energy onto the atomic wavefunctions. In doing so we can evalutate how each atoms contributes to each state. Here we plot the total band structure, in red, as well as the states whose majority contributions are from the graphene, in blue, and topmost QL, in green. We define a state as having a majority contribution when the total contribution from a particular subsystem, either the graphene or top QL, is $\geq 50\%$ of the normalised eigenstate. The total contribution is the sum of all the projections of the normalised eigenstate onto the states of the subsystem in question.

Comparing the bandstructures to those of the Bi_2Se_3 slab, Figure 6.4 we see that all methods predict the composite material to be metallic. The plots clearly show that the Dirac cones of the graphene overlayer are unaffected by the proximity of the Bi_2Se_3 slab. Additionally we see that the graphene overlayer pulls the Dirac cones of the Bi_2Se_3 slab closer. By pulling the upper Dirac cone under the Fermi level the underlying Bi_2Se_3 slab becomes metallic.

Table 6.10 shows the extracted band gaps and Dirac gaps from the bandstructures. We define the Dirac gap as the separation between the Bi_2Se_3 Dirac cones. For the Bi_2Se_3 slab the band gap and Dirac gap are equivalent. In the composite material we see a reduction of the Dirac gap at Γ of about 0.9 eV compared to the gaps of the Bi_2Se_3 slab, Table 6.5. Similar to the band gap of the Bi_2Se_3 slab, the Dirac gap closely follows the separation distance of the graphene overlayer from the Bi_2Se_3 slab

Method	Band Gap at Γ point(eV)	Dirac Gap at Γ point(eV)
revPBE	0.255	0.521
PBE	0.250	0.151
revPBE vdW-DF	0.187	0.174
PBE vdW-DF	0.135	0.116
TS-vdW	0.116	0.128
TS-vdW+SCS	0.112	0.131
vdW+MB	0.084	0.153

Table 6.10: Bi_2Se_3-graphene band gaps and Dirac gaps at Γ point - top orientation - Γ point band gaps and Dirac gaps of the 3 QL Bi_2Se_3-graphene slab, calculated at the relaxed slab geometries, Table 6.4. The graphene overlayer is aligned in the "top" position as described in Figure 6.1 at the distances shown in Table 6.8. The Dirac gap is defined as the separation between the Bi_2Se_3 Dirac cones.

Method	Band Gap at Γ point(eV)	Dirac Gap at Γ point(eV)
revPBE	0.261	0.515
PBE	0.194	0.222
revPBE vdW-DF	0.083	0.168
PBE vdW-DF	0.140	0.113
TS-vdW	0.118	0.123
TS-vdW+SCS	0.116	0.122
vdW+MB	0.220	0.140

Table 6.11: Bi_2Se_3-graphene band gaps and Dirac gaps at Γ point - hollow orientation - Γ point band gaps and Dirac gaps of the 3 QL Bi_2Se_3-graphene slab, calculated at the relaxed slab geometries, Table 6.4. The graphene overlayer is aligned in the "hollow" position as described in Figure 6.1 at the distances shown in Table 6.9. The Dirac gap is defined as the separation between the Bi_2Se_3 Dirac cones.

with the largest gap corresponding to non binding revPBE method.

Finally we note that by adsorbing the graphene onto one side of the Bi_2Se_3 slab we break the inversion symmetry of the slab resulting in Rashba splitting of the energy bands. This energy splitting is strongest for the PBE vdW-DF method which had the shortest Bi_2Se_3-graphene separation.

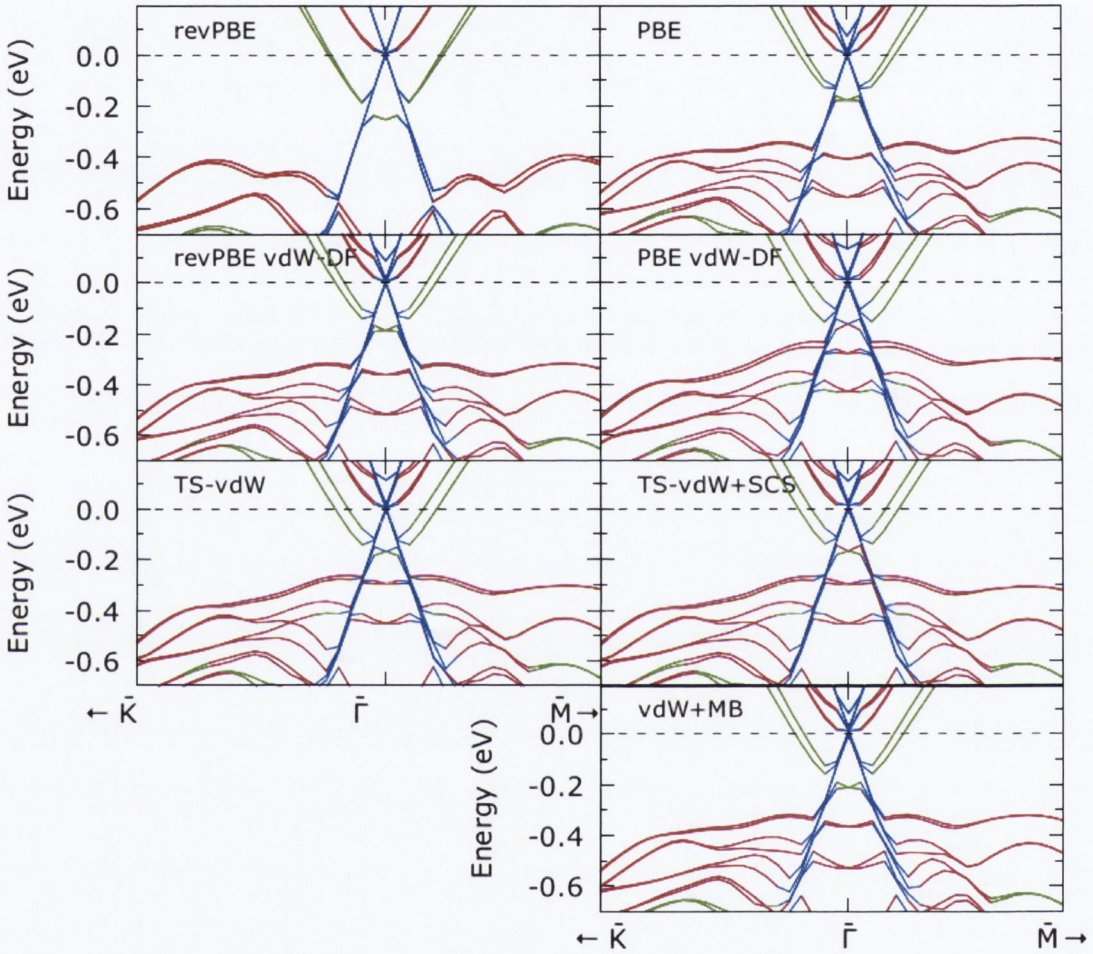


Figure 6.9: Bi_2Se_3-graphene band structures - top orientation - Band structures of the 3 QL Bi_2Se_3-graphene system, calculated at the relaxed slab geometries, Table 6.4, and overlayer distances. Here the graphene is aligned in the "top" orientation, see Figure 6.1, at the calculated distances shown in Table 6.8. The 2D Brillouin zone of the surface is shown in Figure 6.1. A total of 40 k points taken near the $\bar{\Gamma}$ point in the $\bar{K}$ and $\bar{M}$ directions are used. The energies attributed to the graphene are marked in blue. The energies attributed to Bi_2Se_3 top QL are marked in green. The bands are aligned at the Fermi level, which is plotted as the dashed grey line.

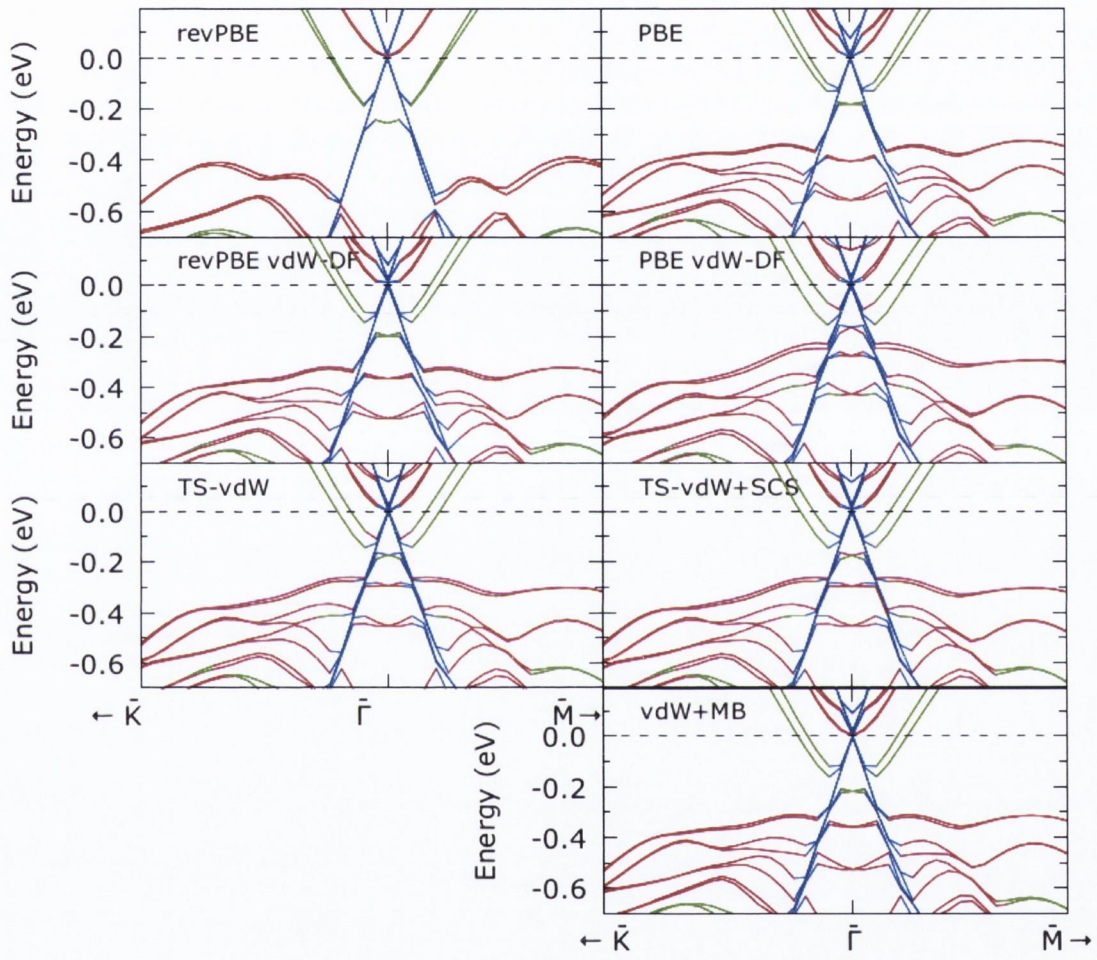


Figure 6.10: Bi_2Se_3-graphene band structures - hollow orientation - Band structures of the 3 QL Bi_2Se_3-graphene system, calculated at the relaxed slab geometries, Table 6.4, and overlayer distances. Here the graphene is aligned in the "hollow" orientation, see Figure 6.1, at the calculated distances shown in Table 6.9. The 2D Brillouin zone of the surface is shown in Figure 6.1. A total of 40 k points taken near the $\bar{\Gamma}$ point in the $\bar{K}$ and $\bar{M}$ directions are used. The energies attributed to the graphene are marked in blue. The energies attributed to Bi_2Se_3 top QL are marked in green. The bands are aligned at the Fermi level, which is plotted as the dashed grey line.

6.4 Conclusions

In this work we have compared the vdW-DF density based vdW functional against various other vdW methods. These methods are the TS-vdW, based on the pair-wise summation, the TS-vdW+SCS, based on the pair-wise summation and includes long range correlation screening, and the vdW+MB, includes long range correlation screening and many body effects, methods from the Tkatchenko-Scheffler publications. By comparing the vdW-DF against these methods with varying levels of beyond pairwise interactions, we can get a better sense of the performance of the vdW-DF homogeneous density dielectric function approximation.

Our bilayer graphene results show the vdW+MB method gives binding energy results closest to DMC calculations for both stackings. The need for vdW methods with beyond pairwise contributions has been noted by Dobsen *et al.* [131, 68]. While all the vdW methods tested overbound with respect to the DMC results, the vdW-DF with PBE exchange overbound the most. This is a known consequence of pairing the vdW-DF with the PBE exchange [59], and is a result of the attractive nature of the PBE exchange term [146]. The vdW-DF method with revPBE exchange produced binding energies close to those of the TS-vdW for both stackings. This result indicates that the homogeneous density approximation, the vdW-DF functional uses to estimate the dielectric function, fails to capture long range correlation screening.

The inter QL separation distances for all the vdW methods lie within 0.2 Å of each other. Additionally the TS-vdW and TS-vdW+SCS methods, vdW without and with long range correlation screening, suggest there is no long range correlation screening internally within the 3 QL Bi_2Se_3 slab. This is in line with previous calculations for few layer Bi_2Se_3 slabs which suggest the thin slabs are insulating [134, 136].

Our results for the convergence of the Bi_2Se_3-graphene overlayer binding energy show no variations greater than 1 meV/carbon atom independent of the number

of QLs included within the slab. This results suggests that the geometry of the Bi_2Se_3-graphene interface is almost entirely determined by the interaction between the graphene and the top QL.

Our overlayer binding energies for the vdW-DF with revPBE exchange are between 28-30 meV/carbon atom, depending on the alignment of the overlayer. Calculations using similar graphene supercells and the vdW-DF with revPBE exchange for the adsorption of graphene onto the surface of metallic surfaces found binding energies in the range 36-42 meV/carbon atom [147]. The preservation of the graphene Dirac cones along with the low binding energies and large overlayer separation distances confirm that the graphene is physisorbed onto the slab surface [148].

While the graphene bands are not affected by the proximity of the Bi_2Se_3 slab, the electronic structure of the slab is affected by the graphene. The adsorption of the graphene onto one side of the slab breaks inversion symmetry for the system and introduces Rashba splitting of the Bi_2Se_3 bands away from the Γ point. The magnitude of the splitting increases with decreased separation of the graphene from the slab. This is in line with previous calculations [134]

The adsorption of the graphene overlayer acts to significantly reduce the energy gap between the Dirac cones of the Bi_2Se_3 slab, decreasing the gap by as much as 900 meV.

Independent of the method used we found the 'hollow' site was the preferred adsorption site for the graphene. Additionally for all methods the adsorption caused a shift in the Fermi level making the Bi_2Se_3 slab metallic.

In summary, the good agreement between the vdW+MB and the DMC results suggest this is the best method to use; producing accurate beyond pairwise approximate results at a low computational cost. Because of the insulating nature of the individual Bi_2Se_3 QLs internal coordinates for Bi_2Se_3 slabs can be obtained from vdW methods

without explicit non-local correlation screening. The geometry of the Bi_2Se_3-graphene interface is entirely determined by the interaction between the graphene and the first QL. All the vdW methods tested predict the 'hollow' orientation as the preferred adsorption site and that the proximity of the graphene causes the Bi_2Se_3 slab to become metallic as well as introducing Rashba splitting. Overall this work shows the failure of the approximate dielectric function used in the vdW-DF method to capture non-local correlation screening as well as the need for such corrections to achieve accurate quantitative results. While broad qualitative features of the Bi_2Se_3-graphene hetrostructure are captured by all the vdW methods tested there are significant differences in overlayer binding energies between the vdW-DF methods and the beyond pairwise approximation of the vdW+MB. We believe that this work shows that current vdW methods can capture the broad qualitatively features of novel new hetro-structures and identify points of interest where more rigorous, and computationally expensive, methods can be brought to bear.

Chapter 7

Final conclusions and future work.

The work in this thesis is aimed towards exploring the edge case application of the Langreth-Lundqvist vdW density functional. The increasing popularity of the vdW-DF functional has resulted in its application across a wide variety of systems. Some of these systems are at the limit of the approximations made in the derivation of the functional, so called edge case systems. Although the vdW-DF functional may break down when applied to these edge case systems, through careful exploration of these systems we gain a greater understanding of not only the functional but also ways within which it can be improved.

In this chapter we reiterate the main findings of our research chapters. We place these results into a broader context giving a better sense of their significance. Additionally we indicate directions and systems for future interest. Finally we give our general thoughts on the vdW-DF community as well as issues it faces and possible directions for its future.

Our most significant finding of Chapter 4 is that the spin vdW-DF method already put forward, hereafter referred to as the spin-sum approximation, doesn't respect the non-commutativity of the non-local correlation functional where as our spin vdW-DF method does. This results in an over estimation of the vdW interactions by the

spin-sum approximation. This happens more strongly for non-spin polarised systems, where the spin up and spin down densities are identical or near identical.

We tested our spin vdW-DF on three systems, the non-spin polarised N_2-N_2, the O_2-O_2 system in two different geometries for two different spin states and for the phenalenyl molecules which are open shell molecules which interact via vdW. For the O_2 and phenalenyl systems we found the spin-sum method overbound with respect to experimental results. Similarly we found it overbound with respect to our spin vdW-DF method. For the O_2-O_2 system we found that the spin-sum method incorrectly predicted the non-spin state as the lowest energy state for both geometries. It also incorrectly predicted a large energy splitting between the spin polarised and non-spin energy states for both geometries. Our spin vdW-DF method predicts the correct spin state for both geometries as reported from experiments and more accurate coupled cluster results. It also predicts a smaller energy splitting between the spin states, much closer to experiment and coupled cluster results.

A reasonable question to ask is why not approximate a spin vdW calculation by preforming two calculations, one using a non spin vdW to determine the geometry of the problem followed up with a second calculation using a spin XC to determine the energy. Such a procedure is based on the reasonable assumption that the vdW interaction determines the long range interaction while the spin interaction is short ranged and as such the two interactions exist in two isolated regimes. The counter point to this however can be seen in the O_2-O_2 example where different spin states result in drastically different geometries. This is rooted in the fact that any binding curve is made up of two parts, a long range attractive part and a short range repulsive part. As the systems we have investigated are dispersion bound, the long range part is from the vdW contribution and the short range part is due to Pauli repulsion. As the exchange interaction is spin dependent so too will this repulsive energy. The nature

of this repulsion and where the repulsive curve meets the attractive curve, and hence the equilibrium distance, is dependent on the spin state of the interacting systems. From understanding we can disregard the notation that spin vdW calculations can be carried out in a two calculation procedure. The correct binding curve is determined by the interaction of the correct attractive and repulsive curves, both should be captured by the same functional.

The spin-sum approximation is based on the reasonable idea that if the long range attraction is independent of the spin it is appropriate to work with the total charge density rather than the spin density. The spin-sum approximation creates a total charge density by adding the spin up and spin down densities. Our results from the O_2-O_2 system and the phenalenyl molecules show that such approximates overbind with respect to our spin vdW-DF method. Our methods suggests that rather than adding the spins together the interaction of the spin densities should be considered separately. We show that the spin-sum method incorrectly makes the assumption that the interaction using the sum of spin densities is equivalent to the sum of the interactions between the spin densities, or at least the difference between these two evaluations is small. For the phenalenyl molecules the relative difference between our spin vdW-DF and the spin-sum approximation is small, owing to the relatively large dispersion energy between the dimers and the small fraction of unpaired electrons. The opposite is true for the O_2-O_2 system and as such there is a significant difference between the methods which cannot be ignored.

These are two alternative methods to carry out calculations needing both spin and vdW interactions. Our work on this topic and our vdW-DF functional show that such alternatives are either erroneous or unnecessary.

A spin dependent vdW functional is necessary for a particular class of systems. Specifically these are open shell systems bound by dispersion interactions. The biggest

issue with investigating such systems is that open sell compounds are very reactive and as such tend not to exist for long. Because of this neither extensive experimental research nor computational effort has been put into investigating these systems. Along with the O_2-O_2 system we found two other simple paramagnetic dimers which interact in a similar manner. A Diboron complex, B_2-B_2, and possibly a disulphur complex, S_2-S_2. We could not however find reliable experimental or computational results for these systems. In the case of the disulphur complex researchers are unsure if such a dispersion bound complex exists or if atoms form a four membered ring.

The phenalenyl molecule represents another class of systems where our spin vdW-DF can play an active role in materials research. These are open shell systems whose inter-molecule interactions are a mixture of covalent and dispersion forces. It is this class of molecules where our spin vdW-DF will be of most use: for self assembling, open shell molecules bound by dispersion forces [149]; for important organic heme unit based molecules [75]; for single molecule magnets adsorbed to a substrate [150].

Moving to larger systems or wishing to include some many body interaction correction it may become necessary to include beyond shot ranged spin interactions. For systems where the pairwise interaction remains appropriate, an additional long range spin interaction Hamiltonian could be added in a post processing step. The accurate O_2-O_2 results were performed using symmetry adapted perturbation theory, SAPT. The monomers were calculated using coupled cluster, CCSD, calculations and the interaction between them was modelled as a perturbation using the Coulomb interaction. Results from such methods are in good agreement with experiment. This suggests that for small molecules the short range spin interaction is appropriate. There may be a crossover however between small isolated molecules and larger systems where long range spin effects become of greater importance. To investigate this however systems which depend on long range spin interactions will have to be

identified and the long range spin correction Hamiltonian implemented.

Our results from Chapter 5 show that appropriate atom centered basis sets can be constructed to give vdW interactions with errors comparable to those from a plane wave basis. We also showed that the main source of error in vdW binding error calculations when using an atom centered basis set is due to the basis set superposition error. The work is based on a number of our own custom codes. These allowed us to create efficiently optimised basis sets, generate the same pseudopotential in formats suitable for both atom centered basis and plane wave basis DFT calculations and quantify the difference between the densities generated from these two methods.

The result that atom centered basis sets are capable of evaluating the vdW-DF functional at the same level of accuracy as a plane wave basis should be self evident. The vdW-DF after all, calculates vdW energies from the electronic density. If the density can be accurately represented in an atom centered basis, to the same level of accuracy as in a plane wave basis, then accurate vdW-DF interactions can be calculated. By comparing the densities produced by different atom centered basis sets with the density from a converged plane wave basis we were able to quantify the magnitude and source of errors in our calculations. While we found that accurate densities could be constructed from relatively simple basis sets, larger basis sets were necessary to minimise the BSSE.

The fact that BSSE dramatically effects the vdW binding energy is not unknown. Our results echo such findings and reaffirm that there is no systematic method to reduce the BSSE. While we did find that generally, across the S22 database, the addition of ghost atoms to a basis improved the accuracy, for purely dispersion bound systems the opposite was true. As the magnitude of the BSSE is comparable to the binding energies of small to medium complexes, even subtle changes to the basis set can dramatically change the binding energies. In these situations we found adding

additional radial functions to the basis resulted in a more reliable improvement of the binding energies.

Finally we observed that the optimisation of the basis function parameters did not lead to more accurate binding energies. This is due to a loss of transferability as a result of over-fitting of the basis. This over-fitting occurs as we fit the basis function parameters to a single system, for each element. More transferable optimised basis could be obtained by fitting the parameters across a set of systems for each element. This however represents a huge computational effort for an unknown gain when the addition of ghost atoms or additional radial functions are known to improve the accuracy. Succinctly, basis sets with larger numbers of basis functions are more transferable.

While our results regarding the optimisation of the Siesta basis set are not transferable to other atom centered basis codes, our findings on the generation of accurate atom centered basis sets suitable for vdW calculations are. We found in general the addition of ghost atoms to the basis gave the most accurate binding energies. Where complexes were small and purely dispersion bound, the BSSE had the most significant effect. For these complexes the addition of ghost atoms reduced the accuracy of the binding energies. For systems where ghost atoms cannot be used, such as molecular dynamics or atomic relaxations where appropriate sites for the ghost atoms are unknown, the addition of more radial functions to the basis improved the accuracy.

Though simple, these results are a significant benefit to the community. For systems with large unit cells or significant amounts of vacuum it can be computationally cheaper to use an atom centered basis over a plane wave one. Our results show that calculations of such systems can give accurate vdW interaction energies, and forces, independent of the basis set used. Although binding energy calculations will still suffer from BSSE, calculations such as molecular dynamics or atomic relaxations will

remain as accurate in an atom centered basis as a plane wave basis.

The purpose of Chapter 6 was to place the vdW-DF in context with some new beyond pairwise approximation methods. These methods include beyond pairwise approximations of the vdW interaction in the form of non-local correlation screening and many body effects captured by an interaction tensor. By comparing the vdW-DF functional to these methods we gain a better understanding of the limits of the functional. The main result we found was that the homogeneous density approximation of the dielectric function, used in the vdW-DF method, fails to capture any non-local correlation screening.

We also wanted to test these new vdW methods on a Bi_2Se_3-graphene hetrostructure. These novel structures are suggested as a new way to combine layered materials to produce interesting compounds with, perhaps, designer electronic properties. As the layers are bound together with vdW forces and have a wide range of properties ranging from insulating to metallic we must be sure that our vdW methods are accurate across all these

From our calculations of the bilayer graphene in AA and AB stacked configurations we found that the beyond pairwise approximation effects acted to reduce the interlayer binding energies. The vdW+MB method was found to give binding energies closest to highly accurate Monte Carlo results.

Our optimisation of the 3 quintuple layer, QL, Bi_2Se_3 slab suggested that the internal vdW interactions are not screened. We found almost no difference in the inter-QL separations calculated with the TS-vdW and the TS-vdW with self consistent screening. Other experimental results and calculations have shown that the Bi_2Se_3 slabs up to 6 QL remain gapped. As such it is a reasonable result to see that the vdW-DF method gives similar geometries as the beyond pairwise methods.

We found that the interface interaction between the Bi_2Se_3 slab and the graphene

overlayer is entirely captured within the first QL. In calculating the binding energy per carbon atom of the graphene to Bi_2Se_3 slabs comprised of one to four QLs we found no change in the overlayer binding energy.

Our results for the adsorption of the graphene onto the Bi_2Se_3 slab confirmed other work in finding that the 'hollow' position is the preferred adsorption site.

The adsorption of the graphene caused the bandstructure of the Bi_2Se_3 slab to change from gapped, in the case of the isolated slab, to metallic. Additionally we also observed the affect of the graphene on the Bi_2Se_3 energy bands. By adsorbing the graphene onto a single side of the Bi_2Se_3 slab we break the inversion symmetry of the slab along the z direction, the direction along which electrons are confined, and cause Rashba splitting. This effect has been noted in both experiments as well and has been shown to originate from the graphene substrate. Interestingly we observed that the magnitude of the splitting increased for methods which more strongly bound the graphene overlayer. This is a significant consideration for researchers wishing to take advantage of this energy splitting.

We found that the biggest difference between the beyond pairwise methods and the vdW-DF was the magnitude of the binding energies. From all the methods we tested we found quite similar inter-layer separation distances although the gap between the Bi_2Se_3 slab Dirac cones does appear to be relatively sensitive to these small changes. The results do suggest that the vdW-DF method could be used for rough geometry optimisations or exploratory calculations of new systems before applying the beyond pairwise methods to obtain final binding energies. While these beyond pairwise methods remain post processing methods the self-consistent vdW-DF possesses a distinct advantage, to be able to return vdW forces and hence preform geometry relaxations.

To conclude this Chapter we give our more general thoughts on our work and on the vdW in DFT field in general.

Our work towards a spin vdW-DF method is promising. The benefit of our spin vdW-DF over the spin-sum approximation is clear with our results showing a good agreement with experiments. The possibility to extend the vdW-DF to include a new class of systems previously unaccessible with DFT is exciting. In doing so we can bring the advantages of the DFT method to these problems allowing for the investigation of larger systems than previously allowed under quantum chemistry methods. The issues however will be in ensuring the results are reliable and accurate, a difficult feat with such a new method. Of greatest benefit towards the advancement of this method would be the compiling of a database of dispersion bound open shell complexes with optimised geometries and binding energies.

Our Chapter 5 results are very much directed at atom centered basis set users and in particular people using Siesta. This work should highlight for researchers, in particular those unfamiliar with dispersion interactions, the level of basis set accuracy which is required for accurate results. Our work draws a direct comparison between atom centered basis and plane wave basis calculations giving a clear example of the atom centered basis parameters necessary for results comparable to plane wave. We also give more general ideas for creating an accurate atom centered basis set which is capable of being used across a wide variety of systems. Avoid optimisation, adding additional radial functions is better. As a general rule add ghost atoms to get accurate binding energy but be careful when working with purely dispersion bound systems where the BSSE is of a comparable magnitude to the binding energy.

Our work with the several different vdW methods in Chapter 6 highlighted what we believe is the biggest issue regarding the integration of vdW methods in DFT. In our work we have featured two differing approaches to the connection of the dispersion correction to the XC functional:

- the "seamless" connection of the vdW-DF method;

- the C6 methods which rely on a cut-off function to avoid double counting between the correction term and semi-local XC functional to which it is connected.

On the face of it the vdW-DF method appears to be the superior method by removing any empirical fitting in the functional. The issue however is that the vdW-DF functional derives the correlation energy independent of the exchange energy. When researches originally attempted to push improvements into the XC functional to go beyond the LDA they found an immediate loss in accuracy. One of the advantages of DFT is its ability to treat the exchange and correction energy together rather than separately. Researchers found that by building functionals based on models of the XC hole, errors in exchange energy and correlation energy could be balanced leading to more accurate functionals. This is the so called error cancellation of DFT. The issue in trying to select an exchange term to match with the derived correlation term is to find one which balances with the correlation errors to give accurate results. Several different researchers have developed exchange functionals to fit to the correlation and maximise the accuracy possible with the vdW-DF, however the cost is a loss of the *ab inito* nature of the functional.

The alternatives are the C6 parameter based methods which are most definitely empirical in nature. The biggest advantage of these methods is that they can be fitted to work with any semi-local XC and do not affect the accuracy of the XC short ranged interactions. This is unlike the vdW-DF functional whose covalent interactions are not identical to those of the base functional. For example covalent bond lengths calculated with the PBE XC and the vdW-DF with PBE exchange do not match.

Ultimately these factors may lead to researchers finding C6 parameter based methods preferable over the vdW-DF. With its long derivation and tricky computational evaluation it may be difficult to develop this method further. The C6 parameter based methods give researchers a simple, reliable tool which has been shown can be

expanded to include beyond pairwise effects. While the vdW-DF provides hope for an accurate *ab inito* method for the calculation of dispersion forces within DFT, more work must be done to ensure its accuracy and reliability across different systems.

In closing, we repeat our most significant findings regarding our work in generalising the vdW-DF to allow for the interaction of spin densities - our spin vdW-DF. We have shown that our spin vdW-DF is a desirable alternative to the approximate spin-sum method. We have presented a rigorous derivation based on a generalisation of the Langreth-Lundqvist vdW-DF functional. We have shown that for closed shell systems, such as the $(N_2)_2$ complex, our spin vdW-DF and the spin-sum methods are similar. Both methods are in close agreement to the non-spin vdW-DF for spin polarised calculations and congruent with the non-spin vdW-DF for calculations without spin. For the $(O_2)_2$ system we have shown that our spin vdW-DF predicts the correct ground state spin for both geometries considered. Our method also predicts the energy separation between the spin states in close agreement with experimental results. The spin-sum method fails in both of these points, incorrectly predicting a much more strongly bound singlet state for both geometries and consequently predicting a spin state energy splitting much larger than experiment. Our results of the phenalenyl dimer shows that both spin vdW methods give results in reasonable agreement to experimental values.

Appendix A

Phenalenyl molecule optimised atomic coordinates

These are the atomic coordinates of an isolated phenalenyl molecule as optimised with our spin-polarised vdW-DF functional.

C	-4.554546204	0.534713781	-0.000631819
C	-2.132764187	1.615597707	-0.000399773
C	-1.748625246	4.239855530	-0.000551916
C	-4.861469902	-2.048322669	-0.000459532
C	0.000643924	-0.000504335	0.000002655
C	-0.333151515	-2.656330770	0.000154136
C	-2.798756621	-3.634623749	-0.000077547
C	1.814833170	-4.212494189	0.000529950
H	1.571245617	-6.227488209	0.000649063
C	4.205206963	-3.185297129	0.000760871
C	4.547066670	-0.605870001	0.000623061
C	2.466618451	1.039234171	0.000245644

A. PHENALENYL MOLECULE OPTIMISED ATOMIC COORDINATES

C	2.740608411	3.677338978	0.000103649
C	0.655764987	5.234374669	-0.000290243
H	0.907882259	7.248177447	-0.000414130
H	4.608108777	4.473675677	0.000266209
H	-6.732364423	-2.834849791	-0.000593765
H	-3.060430812	-5.648260753	0.000042336
H	5.822715996	-4.410308614	0.001045239
H	6.420751899	0.175586474	0.000790649
H	-3.362386900	5.470736051	-0.000858593
H	-6.176983314	1.754871725	-0.000935144

Appendix B

Inverting the spin Dyson like screening equation

Under the full potential approximation (FPA) [49]* the scaled response function, $\chi^{\lambda}_{\sigma\sigma'}$, is approximated by using the fully-interacting response, $\chi^{\lambda=1}_{\sigma\sigma'}$. The Dyson-like screening equation with spin is written as,

$$\chi^{\lambda}_{\sigma\sigma'} = \chi^{\lambda=1}_{\sigma\sigma'} + \sum_{\nu\nu'} \chi^{\lambda=1}_{\sigma\nu} * [\lambda V + f^{\nu\nu'}_{xc}] * \chi^{\lambda}_{\nu'\sigma'} \tag{B.1.1}$$

where $A * B$ denotes the convolution operation and $f^{\nu\nu'}_{xc}$ denotes the kernel $f^{\nu\nu'}_{xc} = \frac{\delta v_{xc}(r\nu,t)}{\delta n(r'\nu',t')}$. Taking a double sum over the spins σ, σ' giving,

$$\sum_{\sigma\sigma'} \chi^{\lambda}_{\sigma\sigma'} = \sum_{\sigma\sigma'} \chi^{\lambda=1}_{\sigma\sigma'} + \sum_{\sigma\sigma'\nu\nu'} \chi^{\lambda=1}_{\sigma\nu} * [\lambda V + f^{\nu\nu'}_{xc}] * \chi^{\lambda}_{\nu'\sigma'} \tag{B.1.2}$$

First we set $f^{\nu\nu'}_{xc} = 0$, i.e. the FPA approximation, and rearrange the indices of the second term on the right hand side. This is possible as the indices are dummy

*In effect this is identical to the RPA [85] but uses the fully-interacting response, $\chi^{\lambda=1}_{\sigma\sigma'}$ instead of the non-interacting, $\chi^{\lambda=0}_{\sigma\sigma'}$.

variables. This gives

$$\sum_{\sigma\sigma'} \chi^{\lambda}_{\sigma\sigma'} = \sum_{\sigma\sigma'} \chi^{\lambda=1}_{\sigma\sigma'} + \sum_{\sigma\sigma'\nu\nu'} \chi^{\lambda=1}_{\nu\nu'} * [\lambda V] * \chi^{\lambda}_{\sigma\sigma'} \tag{B.1.3}$$

and,

$$\sum_{\sigma\sigma'} \chi^{\lambda}_{\sigma\sigma'} - \sum_{\sigma\sigma'\nu\nu'} \chi^{\lambda=1}_{\nu\nu'} * [\lambda V] * \chi^{\lambda}_{\sigma\sigma'} = \sum_{\sigma\sigma'} \chi^{\lambda=1}_{\sigma\sigma'} \tag{B.1.4}$$

The $\chi^{\lambda}_{\sigma\sigma'}$ term can be included in the summation $\sum_{\nu\nu'}$ as it is constant with respect to the summation. In order to preserve the value of the $\chi^{\lambda}_{\sigma\sigma'}$ term it must be evenly divided across the $\sum_{\nu\nu'}$ summation. If the summation $\sum_{\nu}$ runs over N different spin directions, and similarly the $\sum_{\nu'}$ sum, then $\frac{1}{N^2}$ of the $\chi^{\lambda}_{\sigma\sigma'}$ term must appear in the double summation. This becomes,

$$\sum_{\sigma\sigma'\nu\nu'} \frac{1}{N^2}\chi^{\lambda}_{\sigma\sigma'} - \chi^{\lambda=1}_{\nu\nu'} * [\lambda V] * \chi^{\lambda}_{\sigma\sigma'} = \sum_{\sigma\sigma'} \chi^{\lambda=1}_{\sigma\sigma'} \tag{B.1.5}$$

From this expression we can factorise out the $\chi^{\lambda}_{\sigma\sigma'}$ term giving,

$$\sum_{\sigma\sigma'\nu\nu'} \chi^{\lambda}_{\sigma\sigma'} \left(\frac{1}{N^2} - \chi^{\lambda=1}_{\nu\nu'} * [\lambda V] \right) = \sum_{\sigma\sigma'} \chi^{\lambda=1}_{\sigma\sigma'} \tag{B.1.6}$$

The $\sum_{\nu\nu'}$ summation can be pushed into the brackets and the $\frac{1}{N^2}$ becomes 1,

$$\sum_{\sigma\sigma'} \chi^{\lambda}_{\sigma\sigma'} \left(1 - \sum_{\nu\nu'} \chi^{\lambda=1}_{\nu\nu'} * [\lambda V] \right) = \sum_{\sigma\sigma'} \chi^{\lambda=1}_{\sigma\sigma'} \tag{B.1.7}$$

From this we can write our final expression for the spin-density spin-density response function with coupling constant, λ,

$$\sum_{\sigma\sigma'} \chi^{\lambda}_{\sigma\sigma'} = \sum_{\sigma\sigma'} \chi^{\lambda=1}_{\sigma\sigma'} \left(1 - \sum_{\nu\nu'} \chi^{\lambda=1}_{\nu\nu'} * [\lambda V]\right)^{-1} \tag{B.1.8}$$

Appendix C

Spin vdW kernel

Inserting equation (4.2.38) into (4.2.37) gives,

$$E_c^{nl} = \frac{1}{2} \sum_{\sigma\sigma' \mathbf{q}_1 \mathbf{q}_2} \int d^3r \int d^3r' (1 - (\hat{\mathbf{q}}_1 . \hat{\mathbf{q}}_2)^2) e^{-i(\mathbf{q}_1 - \mathbf{q}_2).\mathbf{r}} e^{-i(\mathbf{q}_2 - \mathbf{q}_1).\mathbf{r}} \omega_{p\sigma} \omega_{p'\sigma'} F(\mathbf{q}_1, \mathbf{q}_2, \mathbf{r}, \mathbf{r}'), \tag{C.1.1}$$

using the convention $\omega_{p\sigma}^2(\mathbf{r}) = \omega_{p\sigma}^2 = 4\pi n_\sigma(\mathbf{r})$ and $\omega_{p\sigma}(\mathbf{r}') = \omega'_{p\sigma}$ to denote the plasma frequency. The F function is,

$$\begin{aligned} F(\mathbf{q}_1, \mathbf{q}_2, \mathbf{r}, \mathbf{r}') = \int_0^\infty \frac{du}{2\pi} \frac{1}{2} \left(\frac{1}{(iu + \omega_{q_1})(-iu + \omega_{q_2})} + \frac{1}{(-iu + \omega_{q_1})(iu + \omega_{q_2})} \right) \\ \times \frac{1}{2} \left(\frac{1}{(iu + \omega'_{q_1})(-iu + \omega'_{q_2})} + \frac{1}{(-iu + \omega'_{q_1})(iu + \omega'_{q_2})} \right) \end{aligned} \tag{C.1.2}$$

where ω_σ^q is the spin dependent dispersion function. Using the approximate formula from Dion,

$$\omega_\sigma^q(\mathbf{r}) = \frac{q^2}{2h(1/q_\sigma^0(\mathbf{r}))} \tag{C.1.3}$$

with $h(x) = 1 - e^{-ax^2}$, being a cutoff function for the large q limit. The parameter q^0 is then given by the ratio,

$$q^0(\mathbf{r}) = \frac{\epsilon_{xc}^0(\mathbf{r})}{\epsilon_x^{lda}(\mathbf{r})} k_F(\mathbf{r}) \tag{C.1.4}$$

given that $k_F(\mathbf{r})$ is the Fermi vector it is easy to see how this quantity can be extended to the spin density regime. The kernel function, $\phi_{\sigma\sigma'}(\mathbf{r}, \mathbf{r}')$, is then given by,

$$\phi_{\sigma\sigma'}(\mathbf{r}, \mathbf{r}') = A \sum_{\mathbf{q}_1 \mathbf{q}_2} F(\mathbf{q}_1, \mathbf{q}_2, \mathbf{r}, \mathbf{r}') W(q_1, q_2, |\mathbf{r} - \mathbf{r}'|) \tag{C.1.5}$$

Where

$$W(q_1, q_2, |\mathbf{r} - \mathbf{r}'|) = (1 - (\hat{\mathbf{q}}_1 . \hat{\mathbf{q}}_2)^2) e^{-i(\mathbf{q}_1 - \mathbf{q}_2).\mathbf{r}} e^{-i(\mathbf{q}_2 - \mathbf{q}_1).\mathbf{r}}, \tag{C.1.6}$$

is identical to the similar expression appearing in Dion, equation 16 in Reference [49]. A is a constant resulting in the final, spin dependent expression of equation (4.2.40).

Appendix D

Evaluating the spin vdw kernel

Equation (C.1.5) highlights an issue with this functional, the kernel clearly has a spin dependence but is it different from the Dion kernel [49, 84]? How can we evaluate it? The most widely implemented algorithm to evaluate equation (3.4.1) is the algorithm of Román-Pérez and Soler [77]. Critical to this algorithm is the expansion of the kernel,

$$\phi(\mathbf{q}_1, \mathbf{q}_2, R) \simeq \sum_{\alpha\beta} \phi(\mathbf{q}_\alpha, \mathbf{q}_\beta, R) P_\alpha(\mathbf{q}_1) P_\beta(\mathbf{q}_2) \tag{D.1.1}$$

with $R = |\mathbf{r} - \mathbf{r}'|$, $\mathbf{q}_\alpha$ are fixed values and P_α are interpolating functions. The purpose behind this expansion is to then transform equation (3.4.1) to Fourier space, reducing the costly double integral to a single integral. Applying a similar expansion to our

spin kernel gives,

$$E_c^{nl} = \frac{1}{2}\sum_{\sigma\sigma'}\int\int d^3\mathbf{r}d^3\mathbf{r}' n_\sigma(\mathbf{r})\phi_{\sigma\sigma'}(R)n_{\sigma'}(\mathbf{r}')$$

$$= \frac{1}{2}\sum_{\sigma\sigma'\alpha\beta}\int\int d^3\mathbf{r}d^3\mathbf{r}'\theta_{\alpha\sigma}(\mathbf{r})\phi^{\alpha\beta}(R)\theta_{\beta\sigma'}(\mathbf{r}') \tag{D.1.2}$$

$$= \frac{1}{2}\sum_{\sigma\sigma'\alpha\beta}\int d^3\mathbf{k}\theta_{\alpha\sigma}(\mathbf{k})\phi^{\alpha\beta}(k)\theta_{\beta\sigma'}(\mathbf{k}) \tag{D.1.3}$$

where $\theta_{\alpha\sigma}(\mathbf{r}) = n_\sigma(\mathbf{r})P_\alpha(q_\sigma^0(n_\sigma(\mathbf{r})))$ and $\phi^{\alpha\beta}(R) \equiv \phi(\mathbf{q}_\alpha, \mathbf{q}_\beta, R)$. Equation (D.1.3) has undergone a fourier transform, as such the variables are the fourier transform of their real space counterparts.

What is important for us here though is that the spin dependence has been removed from the "core" of the kernel, $\phi^{\alpha\beta}(R)$. This is beneficial to us as we can utilise the pre-calculated table of values from the standard Román-Pérez/Soler implementation for $\phi^{\alpha\beta}(R)$. The theta values are calculated at run time on a grid, matching the density grid, for the range of q-value interpolation points. In our implementation of the spin kernel in code we simply calculate, and save, the theta values calculated using both spin densities*.

*$\sigma = \{\uparrow, \downarrow\}$

Appendix E

Our calculated S22 binding energies as well as the optimised Siesta basis sets and pseudopotentials used.

E.1 Our calculated S22 binding energies.

We present our binding energies calculated using Siesta with double zeta + polarised, DZP, double zeta + polarised with ghost atoms, DZP+ghosts, triple zeta + polarised, TZP, and optimised, OPT, basis sets.

E. OUR CALCULATED S22 BINDING ENERGIES AS WELL AS THE OPTIMISED SIESTA BASIS SETS AND PSEUDOPOTENTIALS USED.

No.	Complex	DZP (meV)	DZP+ghosts (meV)	TZP (meV)	OPT (meV)
1	Ammonia dimer	134	101	131	199
2	Water dimer	253	141	247	277
3	Formic acid dimer	929	704	834	687
4	Formamide dimer	737	587	671	607
5	Uracil dimer hb	929	772	867	837
6	2-pyridoxine 2-aminopyridine	778	652	738	796
7	Adenine thymine wc	768	620	726	780
8	Methane dimer	17	42	23	51
9	Ethene dimer	84	52	83	83
10	Benzene methane	72	47	68	113
11	Benzene dimer (slip-parallel)	122	100	122	168
12	Pyrazine dimer	207	141	211	182
13	Uracil dimer (stack)	512	362	514	511
14	Indole benzene (stack)	222	150	230	230
15	Adenine thymine (stack)	533	384	543	406
16	Ethene ethine	75	64	84	95
17	Benzene water	198	113	172	160
18	Benzene ammonia	111	76	107	107
19	Benzene hcn	182	149	182	191
20	Benzene dimer (T-shape)	144	109	150	141
21	Indole benzene (T-shape)	249	179	245	245
22	Phenol dimer	328	227	317	356

Table E.1: Our calculated S22 binding energies - The binding energies from our Siesta calculations for the double zeta + polarised, DZP, double zeta + polarised with ghost atoms, DZP+ghosts, triple zeta + polarised, TZP, and optimised, OPT, basis sets.

E.2 Optimised Siesta basis sets.

For this work we used optimised basis sets for carbon, hydrogen, nitrogen and oxygen. We used pre-calculated parameters for hydrogen and oxygen and generated our own basis for carbon and nitrogen. In order to create optimised basis sets we used a particle swarm optimiser to variationally select the cut-offs of each of the zetas as well as parameters for the cut-off function.

Each basis was optimised in a particular chemical environment. For the oxygen and hydrogen bases the water monomer was used, for nitrogen the N_2 dimer, and for carbon the benzene with methane ghost atoms system.*

Below we give the optimised basis set parameters used in this work, in the Siesta input format.

Optimised hydrogen basis

```
H     2       0.22
n=1    0    2   E      2.07       0.00
4.971    1.771
n=2    1    1   E      0.89       0.01
4.988
```

Optimised carbon basis

```
C     3    0.646669
 n=2    0    2   E      0.670840      -0.933314
```

*A carbon basis optimised using an isolated benzene ring was also tested. In both cases all the other species, including ghosts, were represented with a TZP basis. This alternative basis was rejected as the difference between the counterpoise corrected and non corrected binding energies for the benzene ammonia complex was 76meV versus the 22meV for the benzene with ghost system. The additional criterion of minimising the difference in the corrected and uncorrected results added to help in the optimisation of the carbon basis. As mentioned in Section 5.4.1 this is the standard measure of BSSE errors for binding energy calculations.

```
   7.711389          -0.145525
 n=2    1    2   E      99.999829      -0.959560
   13.999999          -0.000000
 n=3    0    1   E      99.993343      -1.000000
   13.999998
```

Optimised nitrogen basis

```
N      2 -0.031268
 n=2    0    2  E 39.703023      -0.845926
        8.796486          2.691619
 n=2    1    2   E      35.361655      -0.435948
   10.597426 3.273545
```

Optimised oxygen basis

```
O      3      -0.20
n=2    0    2   E       0.00       1.31
5.000    2.581
n=2    1    2   E       0.00       5.28
6.500    2.487
n=3    2    1   E     104.31       0.00
3.923
```

E.3 Siesta Pseudopotentials.

For each of the elements we generated pseudopotentials using our cross code pseudopotential generator. This code outputs the same pseudopotentials in both Siesta

and QE formats. The pseudopotentials we generated using the vdW-DF XC and the following atomic configurations:

- Hydrogen: 1S1 2p0 3d0 4f0,
- Carbon: 2S2 2p2 3d0 4f0,
- Nitrogen: 2S2 2p3 3d0 4f0,
- Oxygen: 2S2 2p4 3d0 4f0.

To satisfy Siestas pseudopotential format we must generate pseudopotentials with each of the four angular momenta channels. To do this we add empty channels with very short cutoffs.

Appendix F

Bi_2Se_3 $R\bar{3}m$ structure in a hexagonal lattice.

Here we use a hexagonal lattice constants to allow for easier lattice matching with the graphene overlayer. The unit cell vectors are,

$$\mathbf{v_1} = a\hat{x} \tag{F.0.1}$$

$$\mathbf{v_2} = -\frac{a}{2}\hat{x} + \frac{\sqrt{3}a}{2}\hat{y} \tag{F.0.2}$$

$$\mathbf{v_3} = c\hat{z}, \tag{F.0.3}$$

where $\hat{x}$, $\hat{y}$, and $\hat{z}$, are unit vectors along the orthongal directions where $\hat{x}$ and $\hat{y}$ are in the plane of the quintuple layer.

Each quintuple layer comprises of five atoms whose internal parameters, u and v

can be obtained from litrature [119],

$$\text{Se} \quad (0, 0, v) \tag{F.0.4}$$

$$\text{Bi} \quad (0, 0, u) \tag{F.0.5}$$

$$\text{Se} \quad (0, 0, 0) \tag{F.0.6}$$

$$\text{Bi} \quad (0, 0, -u) \tag{F.0.7}$$

$$\text{Se} \quad (0, 0, -v). \tag{F.0.8}$$

References

[1] Kolb, B., Kertesz, M. & Thonhauser, T. Binding Interactions in Dimers of Phenalenyl and Closed-Shell Analogues. *The Journal of Physical Chemistry A* **117**, 3642–3649, 17 (2013).

[2] Obata, M. *et al.* Implementation of van der Waals Density Functional Approach to the Spin-Polarized System: Interaction Potential between Oxygen Molecules. *Journal of the Physical Society of Japan* **82**, 9 (2013).

[3] Soler, J. M. *et al.* The SIESTA method for ab initio order-N materials simulation. *Journal of Physics: Condensed Matter* **14**, 2745, 11 (2002).

[4] Tkatchenko, A. *et al.* Accurate and Efficient Method for Many-Body van der Waals Interactions. *Physical Review Letters* **108**, 236402 (2012).

[5] Griffiths, D. J. & Dick, G. Introduction to quantum mechanics. *Physics Today* **48**, 94 (1995).

[6] Sakurai, J. J., Tuan, S.-F. & Commins, E. D. Modern quantum mechanics. *American Journal of Physics* **63**, 93 (1995).

[7] Sherrill, C. D. & Schaefer III, H. F. The configuration interaction method: Advances in highly correlated approaches. *Advances in Quantum Chemistry* **34**, 143–269 (1999).

[8] Cramer, C. J. *Essentials of Computational Chemistry: Theories and Models* (Wiley. com, 2005).

[9] Shavitt, I. & Bartlett, R. J. *Many-Body Methods in Chemistry and Physics: MBPT and Coupled-Cluster Theory* (Cambridge University Press, 2009).

[10] Møller, C. & Plesset, M. S. Note on an Approximation Treatment for Many-Electron Systems. *Physical Review* **46**, 618–622 (1934).

[11] Thomas, L. H. The calculation of atomic fields. In *Mathematical Proceedings of the Cambridge Philosophical Society*, vol. 23, 542–548 (Cambridge University Press, 1927).

[12] Fermi, E. & Amaldi, E. *Collected Papers:(Note E Memorie).*, vol. 2 (University of Chicago Press, 1965).

[13] Dirac, P. A. Note on exchange phenomena in the Thomas atom. In *Mathematical Proceedings of the Cambridge Philosophical Society*, vol. 26, 376–385 (Cambridge University Press, 1930).

[14] Parr, R. G. & Yang, W. *Density-Functional Theory of Atoms and Molecules*, vol. 16 (Oxford university press, 1989).

[15] Teller, E. On the stability of molecules in the Thomas-Fermi theory. *Reviews of Modern Physics (US)* **34** (1962).

[16] Hohenberg, P. & Kohn, W. Inhomogeneous electron gas. *Physical Review* **136**, B864, 3B (1964).

[17] Levy, M. Electron densities in search of Hamiltonians. *Physical Review A* **26**, 1200–1208 (1982).

[18] Kohn, W. & Sham, L. J. Self-Consistent Equations Including Exchange and Correlation Effects. *Physical Review* **140**, A1133–A1138 (1965).

[19] Ceperley, D. & B.J.Alder. Ground state of the electron gas by a stochastic method. *Physical Review Letters* **45**, 7 (1980).

[20] Perdew, J. P. & Wang, Y. Accurate and simple analytic representation of the electron-gas correlation energy. *Physical Review B* **45**, 13244–13249 (1992).

[21] von Barth, U. & Hedin, L. A local exchange-correlation potential for the spin polarized case. i. *Journal of Physics C: Solid State Physics* **5**, 1629, 13 (1972).

[22] Hood, R. Q. *et al.* Exchange and correlation in silicon. *Physical Review B* **57**, 8972–8982 (1998).

[23] Martin, R. M. *Electronic Structure: Basic Theory and Practical Methods* (Cambridge University Press, 2004).

[24] Ashcroft, N. & Mermin, N. *Solid State Physics.* HRW international editions (Holt, Rinehart and Winston, 1976).

[25] Kittel, C. & McEuen, P. *Introduction to solid state physics*, vol. 8 (Wiley New York, 1976).

[26] Langreth, D. C. & Mehl, M. J. Beyond the local-density approximation in calculations of ground-state electronic properties. *Physical Review B* **28**, 1809–1834 (1983).

[27] Perdew, J. P., Burke, K. & Ernzerhof, M. Generalized Gradient Approximation Made Simple. *Physical Review Letters* **77**, 3865–3868 (1996).

[28] Zhang, Y. & Yang, W. Comment on "Generalized Gradient Approximation Made Simple". *Physical Review Letters* **80**, 890–890 (1998).

[29] Perdew, J. P. & Yue, W. Accurate and simple density functional for the electronic exchange energy: Generalized gradient approximation. *Physical Review B* **33**, 8800–8802 (1986).

[30] Perdew, J. P. *et al.* Accurate Density Functional with Correct Formal Properties: A Step Beyond the Generalized Gradient Approximation. *Physical Review Letters* **82**, 2544–2547 (1999).

[31] Perdew, J. P. & Zunger, A. Self-interaction correction to density-functional approximations for many-electron systems. *Physical Review B* **23**, 5048–5079 (1981).

[32] Hedin, L. New Method for Calculating the One-Particle Green's Function with Application to the Electron-Gas Problem. *Physical Review* **139**, A796–A823 (1965).

[33] Klimes, J. & Michaelides, A. Perspective: Advances and challenges in treating van der Waals dispersion forces in density functional theory. *The Journal of Chemical Physics* **137**, 120901, 12 (2012).

[34] Ooi, N., Rairkar, A. & Adams, J. B. Density functional study of graphite bulk and surface properties. *Carbon* **44**, 231–242, 2 (2006).

[35] Birowska, M., Milowska, K. & Majewski, J. Van der Waals density functionals for graphene layers and graphite. *Acta Physica Polonica A* **120**, 845–848 (2011).

[36] Chen, D.-L., Al-Saidi, W. A. & Johnson, J. K. Noble gases on metal surfaces: Insights on adsorption site preference. *Physical Review B* **84**, 241405 (2011).

[37] Grimme, S. Semiempirical GGA-type density functional constructed with a long-range dispersion correction. *Journal of Computational Chemistry* **27**, 1787–1799, 15 (2006).

[38] Casimir, H. B. G. & Polder, D. The Influence of Retardation on the London-van der Waals Forces. *Physical Review* **73**, 360–372 (1948).

[39] Grimme, S. Accurate description of van der Waals complexes by density functional theory including empirical corrections. *Journal of Computational Chemistry* **25**, 1463–1473, 12 (2004).

[40] Rana, M. K. *et al.* Comparing van der Waals Density Functionals for CO_2 Adsorption in Metal Organic Frameworks. *The Journal of Physical Chemistry C* **116**, 16957–16968, 32 (2012).

[41] Albuquerque, A. R. *et al.* DFT Study with Inclusion of the Grimme Potential on Anatase TiO_2: Structure, Electronic, and Vibrational Analyses. *The Journal of Physical Chemistry A* **116**, 11731–11735, 47 (2012).

[42] Bučko, T. *et al.* Improved description of the structure of molecular and layered crystals: Ab initio DFT calculations with van der Waals corrections. *The Journal of Physical Chemistry A* **114**, 11814–11824, 43 (2010).

[43] Appalakondaiah, S. *et al.* Effect of van der Waals interactions on the structural and elastic properties of black phosphorus. *Physical Review B* **86**, 035105, 3 (2012).

[44] Tkatchenko, A. & Scheffler, M. Accurate Molecular Van Der Waals Interactions from Ground-State Electron Density and Free-Atom Reference Data. *Physical Review Letters* **102**, 073005 (2009).

[45] Grimme, S. *et al.* A consistent and accurate ab initio parametrization of density functional dispersion correction (DFT-D) for the 94 elements H-Pu. *The Journal of Chemical Physics* **132**, 154104, 15 (2010).

[46] Chu, X. & Dalgarno, A. Linear response time-dependent density functional theory for van der Waals coefficients. *The Journal of Chemical Physics* **121**, 4083 (2004).

[47] Andersson, Y., Langreth, D. C. & Lundqvist, B. I. van der Waals Interactions in Density-Functional Theory. *Physical Review Letters* **76**, 102–105 (1996).

[48] Rydberg, H. *et al.* Van der Waals Density Functional for Layered Structures. *Physical Review Letters* **91**, 126402 (2003).

[49] Dion, M. *et al.* Van der Waals Density Functional for General Geometries. *Physical Review Letters* **92**, 24 (2004).

[50] Thonhauser, T., Puzder, A. & Langreth, D. C. Interaction energies of monosubstituted benzene dimers via nonlocal density functional theory. *The Journal of Chemical Physics* **124**, 164106 (2006).

[51] Puzder, A., Dion, M. & Langreth, D. C. Binding energies in benzene dimers: Nonlocal density functional calculations. *The Journal of Chemical Physics* **124**, 164105 (2006).

[52] Thonhauser, T. *et al.* Van der Waals density functional: Self-consistent potential and the nature of the van der Waals bond. *Physical Review B* **76**, 125112 (2007).

[53] Vydrov, O. A. & Van Voorhis, T. Nonlocal van der Waals Density Functional Made Simple. *Physical Review Letters* **103**, 063004 (2009).

[54] Vydrov, O. A. & Van Voorhis, T. Improving the accuracy of the nonlocal van der Waals density functional with minimal empiricism. *The Journal of Chemical Physics* **130**, 104105 (2009).

[55] Vydrov, O. A. & Van Voorhis, T. Dispersion interactions from a local polarizability model. *Physical Review A* **81**, 062708 (2010).

[56] Lee, K. *et al.* Higher-accuracy van der Waals density functional. *Physical Review B* **82**, 081101, 8 (2010).

[57] Gulans, A., Puska, M. J. & Nieminen, R. M. Linear-scaling self-consistent implementation of the van der Waals density functional. *Physical Review B* **79**, 201105(R) (2009).

[58] Cooper, V. R. Van der waals density functional:an appropriate exchange functional. *Physical Review B* **81**, 164404(R) (2010).

[59] Klimeš, J., Bowler, D. R. & Michaelides, A. Chemical accuracy for the van der Waals density functional. *Journal of Physics: Condensed Matter* **22**, 022201 (2010).

[60] Mittendorfer, F. *et al.* Graphene on Ni(111): Strong interaction and weak adsorption. *Physical Review B* **84**, 201401 (2011).

[61] Klimeš, J., Bowler, D. R. & Michaelides, A. Van der Waals density functionals applied to solids. *Physical Review B* **83**, 195131, 19 (2011).

[62] Ziambaras, E. *et al.* Potassium intercalation in graphite: A van der Waals density-functional study. *Physical Review B* **76**, 155425, 15 (2007).

[63] Langreth, D. C. *et al.* Van der Waals density functional theory with applications. *International Journal of Quantum Chemistry* **101**, 599–610, 5 (2005).

[64] Sabatini, R. *et al.* Structural evolution of amino acid crystals under stress from a non-empirical density functional. *Journal of Physics: Condensed Matter* **24**, 424209, 42 (2012).

[65] Bohm, D. & Pines, D. A Collective Description of Electron Interactions: III. Coulomb Interactions in a Degenerate Electron Gas. *Physical Review* **92**, 609–625 (1953).

[66] Bruneval, F. Range-Separated Approach to the RPA Correlation Applied to the van der Waals Bond and to Diffusion of Defects. *Physical Review Letters* **108**, 256403 (2012).

[67] Dobson, J. F. & Wang, J. Successful Test of a Seamless van der Waals Density Functional. *Physical Review Letters* **82**, 2123–2126 (1999).

[68] Lebègue, S. *et al.* Cohesive Properties and Asymptotics of the Dispersion Interaction in Graphite by the Random Phase Approximation. *Physical Review Letters* **105**, 196401 (2010).

[69] Björkman, T. *et al.* van der Waals Bonding in Layered Compounds from Advanced Density-Functional First-Principles Calculations. *Physical Review Letters* **108**, 235502 (2012).

[70] Dobson, J. F., White, A. & Rubio, A. Asymptotics of the Dispersion Interaction: Analytic Benchmarks for van der Waals Energy Functionals. *Physical Review Letters* **96**, 073201 (2006).

[71] Shimizu, Y. R., Donati, P. & Broglia, R. A. Response Function Technique for Calculating the Random-Phase Approximation Correlation Energy. *Physical Review Letters* **85**, 2260–2263 (2000).

[72] Furche, F. Molecular tests of the random phase approximation to the exchange-correlation energy functional. *Physical Review B* **64**, 195120 (2001).

[73] Harris, J. Adiabatic-connection approach to Kohn-Sham theory. *Physical Review A* **29**, 1648–1659 (1984).

[74] Aquilanti, V. *et al.* Molecular Beam Scattering of Aligned Oxygen Molecules. The Nature of the Bond in the O_2-O_2 Dimer. *Journal of the American Chemical Society* **121**, 10794–10802, 46 (1999).

[75] Minaev, B. & Minaeva, V. Spin-dependent binding of dioxygen to heme and charge-transfer mechanism of spin-orbit coupling enhancement. *Ukrainica Bioorganica Acta 2* 56 (2008).

[76] Rydberg, H. *Long- and Medium-Ranged Nonlocal Correlations in Density Functional Theory.* Ph.D. thesis, Department of Applied Physics, Chalmers University of Technology and Göteborg University, S-412 96 Göteborg, Sweden (2001).

[77] Román-Pérez, G. & Soler, J. M. Efficient implementation of a van der Waals density functional: application to double-wall carbon nanotubes. *Physical Review Letters* **103**, 096102, 9 (2009).

[78] Gunnarsson, O. & Lundqvist, B. I. Exchange and correlation in atoms, molecules, and solids by the spin-density-functional formalism. *Physical Review B* **13**, 4274–4298 (1976).

[79] Jacob, C. R. & Reiher, M. Spin in Density-Functional Theory. *ArXiv e-prints* (2012).

[80] Kubo, R. The fluctuation-dissipation theorem. *Reports on Progress in Physics* **29**, 255, 1 (1966).

[81] Perdew, J. P. & Zunger, A. Self-interaction correction to density-functional approximations for many-electron systems. *Physical Review B* **23**, 5048, 10 (1981).

[82] Runge, E. & Gross, E. K. U. Density-Functional Theory for Time-Dependent Systems. *Physical Review Letters* **52**, 997–1000 (1984).

[83] Petersilka, M., Gossmann, U. J. & Gross, E. K. U. Excitation Energies from Time-Dependent Density-Functional Theory. *Physical Review Letters* **76**, 1212–1215 (1996).

[84] Dion, M. *van der Waals Forces in Density Functional Theory.* Ph.D. thesis, Graduate School–New BrunswickRutgers, The State University of New Jersey (2004).

[85] Nozières, P. & Pines, D. Correlation Energy of a Free Electron Gas. *Physical Review* **111**, 442–454 (1958).

[86] Kanjouri, F., Esmailian, A. H. & Molayem, M. Spin polarization effect in 2D and Q2D electron gas. *The European Physical Journal B* **79**, 429–433, 4 (2011).

[87] Giannozzi, P. *et al.* QUANTUM ESPRESSO: a modular and open-source software project for quantum simulations of materials. *Journal of Physics: Condensed Matter* **21**, 395502 (19pp), 39 (2009).

[88] Bussery, B. & Wormer, P. A van der Waals intermolecular potential for $(O_2)_2$. *The Journal of Chemical Physics* **99**, 1230 (1993).

[89] Aquilanti, V. *et al.* Dimers of the major components of the atmosphere: Realistic potential energy surfaces and quantum mechanical prediction of spectral features. *Physical Chemistry Chemical Physics* **3**, 3891–3894, 18 (2001).

[90] Huber, K. & Herzberg, G. Molecular Structure and Molecular Spectra. IV. Constants of Diatomic Molecules. *Van Rostrand-Reinhold, New York* (1979).

[91] Troullier, N. & Martins, J. L. Efficient pseudopotentials for plane-wave calculations. *Physical Review B* **43**, 3 (1991).

[92] Skylaris, C.-K. *et al.* Introducing ONETEP: Linear-scaling density functional simulations on parallel computers. *The Journal of Chemical Physics* **122**, –, 8 (2005).

[93] Ordejón, P. *et al.* Linear system-size scaling methods for electronic-structure calculations. *Physical Review B* **51**, 1456 (1995).

[94] Junquera, J. *et al.* Numerical atomic orbitals for linear-scaling calculations. *Physical Review B* **64**, 235111 (2001).

[95] Kohn, W. Density Functional and Density Matrix Method Scaling Linearly with the Number of Atoms. *Physical Review Letters* **76**, 3168–3171 (1996).

[96] Prodan, E. & Kohn, W. Nearsightedness of electronic matter. *Proceedings of the National Academy of Sciences of the United States of America* **102**, 11635–11638, 33 (2005).

[97] Ordejón, P., Artacho, E. & Soler, J. M. Self-consistent order-N density-functional calculations for very large systems. *Physical Review B* **53**, R10441–R10444 (1996).

[98] Jurečka, P. *et al.* Benchmark database of accurate (MP2 and CCSD (T) complete basis set limit) interaction energies of small model complexes, DNA base pairs, and amino acid pairs. *Physical Chemistry Chemical Physics* **8**, 1985–1993, 17 (2006).

[99] Čížek, J. On the Correlation Problem in Atomic and Molecular Systems. Calculation of Wavefunction Components in Ursell-Type Expansion Using Quantum-Field Theoretical Methods. *The Journal of Chemical Physics* **45**, 4256 (1966).

[100] Jansen, H. & Ros, P. Non-empirical molecular orbital calculations on the protonation of carbon monoxide. *Chemical Physics Letters* **3**, 140–143, 3 (1969).

[101] Boys, S. F. & Bernardi, F. The calculation of small molecular interactions by the differences of separate total energies. Some procedures with reduced errors. *Molecular Physics* **19**, 553–566, 4 (1970).

[102] Schwenke, D. W. & Truhlar, D. G. Systematic study of basis set superposition errors in the calculated interaction energy of two HF molecules. *The Journal of Chemical Physics* **82**, 2418 (1985).

[103] Vydrov, O. A. & Van Voorhis, T. Implementation and assessment of a simple nonlocal van der Waals density functional. *The Journal of Chemical Physics* **132**, 164113, 16 (2010).

[104] Marom, N. *et al.* Dispersion interactions with density-functional theory: benchmarking semiempirical and interatomic pairwise corrected density functionals. *Journal of Chemical Theory and Computation* **7**, 3944–3951, 12 (2011).

[105] Loushin, S. K., Liu, S.-Y. & Dykstra, C. E. Improved counterpoise corrections for the ab initio calculation of hydrogen bonding interactions. *The Journal of Chemical Physics* **84**, 2720 (1986).

[106] Hamza, A. *et al.* BSSE-free SCF theories: a comment. *Journal of Molecular Structure: THEOCHEM* **501**, 427–434 (2000).

[107] Castro Neto, A. H. *et al.* The electronic properties of graphene. *Reviews of Modern Physics* **81**, 109–162 (2009).

[108] Miró, P., Audiffred, M. & Heine, T. An atlas of two-dimensional materials. *Chemical Society Reviews* (2014).

[109] Geim, A. & Grigorieva, I. Van der Waals heterostructures. *Nature* **499**, 419–425, 7459 (2013).

[110] Koma, A., Sunouchi, K. & Miyajima, T. Fabrication and characterization of heterostructures with subnanometer thickness. *Microelectronic Engineering* **2**, 129–136, 1 (1984).

[111] Koma, A. Van der Waals epitaxy for highly lattice-mismatched systems. *Journal of Crystal Growth* **201**, 236–241 (1999).

[112] Grimme, S. Density functional theory with London dispersion corrections. *Wiley Interdisciplinary Reviews: Computational Molecular Science* **1**, 211–228, 2 (2011).

[113] Langreth, D. C. *et al.* A density functional for sparse matter. *Journal of Physics: Condensed Matter* **21**, 084203, 8 (2009).

[114] Bučko, T. *et al.* Tkatchenko-Scheffler van der Waals correction method with and without self-consistent screening applied to solids. *Physical Review B* **87**, 064110, 6 (2013).

[115] Heyd, J., Scuseria, G. E. & Ernzerhof, M. Hybrid functionals based on a screened Coulomb potential. *The Journal of Chemical Physics* **118**, 8207–8215, 18 (2003).

[116] Seidl, A. *et al.* Generalized Kohn-Sham schemes and the band-gap problem. *Physical Review B* **53**, 3764–3774 (1996).

[117] Adamo, C. & Barone, V. Toward reliable density functional methods without adjustable parameters: The PBE0 model. *The Journal of Chemical Physics* **110**, 6158–6170, 13 (1999).

[118] Lee, B. *et al.* Nonlocal exchange correlation in screened-exchange density functional methods. *Physical Review B* **76**, 245114, 24 (2007).

[119] Wyckoff, R. W. G. *Crystal Structures* (Krieger, 1964).

[120] Fu, L., Kane, C. L. & Mele, E. J. Topological Insulators in Three Dimensions. *Physical Review Letters* **98**, 106803 (2007).

[121] Moore, J. E. & Balents, L. Topological invariants of time-reversal-invariant band structures. *Physical Review B* **75**, 121306 (2007).

[122] Bernevig, B. A. & Zhang, S.-C. Quantum Spin Hall Effect. *Physical Review Letters* **96**, 106802 (2006).

[123] Hasan, M. Z. & Kane, C. L. Colloquium. *Reviews of Modern Physics* **82**, 3045–3067 (2010).

[124] Moore, J. E. The birth of topological insulators. *Nature* **464**, 194–198, 7286 (2010).

[125] Nayak, C. *et al.* Non-Abelian anyons and topological quantum computation. *Reviews of Modern Physics* **80**, 1083–1159 (2008).

[126] Zhang, X., Wang, J. & Zhang, S.-C. Topological insulators for high-performance terahertz to infrared applications. *Physical Review B* **82**, 245107 (2010).

[127] Vilaplana, R. *et al.* Structural and vibrational study of Bi_2Se_3 under high pressure. *Physical Review B* **84**, 184110 (2011).

[128] Cheng, W. & Ren, S.-F. Phonons of single quintuple Bi_2Te_3 and Bi_2Se_3 films and bulk materials. *Physical Review B* **83**, 094301 (2011).

[129] Luo, X., Sullivan, M. B. & Quek, S. Y. First-principles investigations of the atomic, electronic, and thermoelectric properties of equilibrium and strained Bi_2Se_3 and Bi_2Te_3 including van der Waals interactions. *Physical Review B* **86**, 184111 (2012).

[130] Jr, R. A. D., Gobre, V. V. & Tkatchenko, A. Many-body van der Waals interactions in molecules and condensed matter. *Journal of Physics: Condensed Matter* **26**, 213202, 21 (2014).

[131] Dobson, J. F., Gould, T. & Vignale, G. How Many-Body Effects Modify the van der Waals Interaction between Graphene Sheets. *Physical Review X* **4**, 021040 (2014).

[132] Jia, J. Topological insulators: Strain away. *Nature Physics* (2014).

[133] Liu, Y. *et al.* Tuning Dirac states by strain in the topological insulator Bi_2Se_3. *Nature Physics* (2014).

[134] Liu, W. *et al.* Surface and substrate induced effects on thin films of the topological insulators Bi_2Se_3 and Bi_2Te_3. *Physical Review B* **87**, 205315 (2013).

[135] Hasan, M. Z. & Kane, C. L. Colloquium: topological insulators. *Reviews of Modern Physics* **82**, 3045, 4 (2010).

[136] Zhang, Y. *et al.* Crossover of the three-dimensional topological insulator Bi_2Se_3 to the two-dimensional limit. *Nature Physics* **6**, 584–588, 8 (2010).

[137] Blum, V. *et al.* Ab initio molecular simulations with numeric atom-centered orbitals. *Computer Physics Communications* **180**, 2175 – 2196, 11 (2009).

[138] Zhang, I. Y. *et al.* Numeric atom-centered-orbital basis sets with valence-correlation consistency from H to Ar. *New Journal of Physics* **15**, 123033, 12 (2013).

[139] Saito, R. *et al. Physical Properties of Carbon Nanotubes*, vol. 4 (World Scientific, 1998).

[140] Kucukbenli, E. *et al.* Projector augmented-wave and all-electron calculations across the periodic table: a comparison of structural and energetic properties. *arXiv preprint arXiv:1404.3015* (2014).

[141] Laasonen, K. *et al.* Implementation of ultrasoft pseudopotentials in ab initio molecular dynamics. *Physical Review B* **43**, 6796–6799 (1991).

[142] Mostaani, E. & Drummond, N. Binding energy of bilayer graphene and Electronic properties of oligoynes (2014).

[143] Lee, J.-K. *et al.* The growth of AA graphite on (111) diamond. *The Journal of Chemical Physics* **129**, 234709–234709, 23 (2008).

[144] Zhang, H. *et al.* Topological insulators in Bi_2Se_3, Bi_2Te_3 and Sb_2Te_3 with a single Dirac cone on the surface. *Nature Physics* **5**, 438–442, 6 (2009).

[145] Kou, L. *et al.* Graphene-based topological insulator with an intrinsic bulk band gap above room temperature. *Nano Letters* **13**, 6251–6255, 12 (2013).

[146] Ruzsinszky, A., Perdew, J. P. & Csonka, G. I. Binding energy curves from nonempirical density functionals I. van der Waals bonds in rare-gas and alkaline-earth diatomics. *The Journal of Physical Chemistry A* **109**, 11015–11021, 48 (2005).

[147] Zheng, J. *et al.* Interfacial Properties of Bilayer and Trilayer Graphene on Metal Substrates. *Scientific Reports* **3** (2013).

[148] Giovannetti, G. *et al.* Doping graphene with metal contacts. *Physical Review Letters* **101**, 026803, 2 (2008).

[149] Akande, A. *et al.* First principles study of the structural, electronic, and transport properties of triarylamine-based nanowires. *The Journal of Chemical Physics* **140**, 074301, 7 (2014).

[150] Bogani, L. & Wernsdorfer, W. Molecular spintronics using single-molecule magnets. *Nature Materials* **7**, 179–186, 3 (2008).